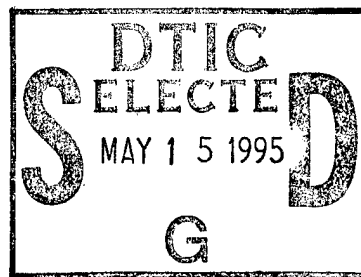


**PROCEEDINGS OF THE ENVIRONMENTAL SITE
CHARACTERIZATION AND MONITORING BASIC
RESEARCH PROGRAM
1995 CONTRACTOR/GRANTEE MEETING,
11-12 MAY 1995**

Editors:

**Katharine Kadinsky-Cade
Steven Cardimona**

May 1995



APPROVED FOR PUBLIC RELEASE; DISTRIBUTION UNLIMITED



PHILLIPS LABORATORY

Directorate of Geophysics


AIR FORCE MATERIEL COMMAND

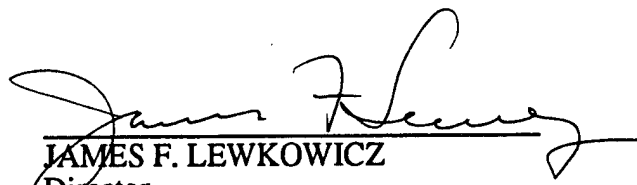
HANSCOM AIR FORCE BASE, MA 01731-3010

DTIC QUALITY INSPECTED 5

19950512 123

This technical report has been reviewed and is approved for publication.


KATHARINE A. KADINSKY-CADE
Task Scientist
Earth Sciences Division


JAMES F. LEWKOWICZ
Director
Earth Sciences Division

This report has been reviewed by the ESC Public Affairs Office (PA) and is releasable to the National Technical Information Service (NTIS).

Qualified requestors may obtain additional copies from the Defense Technical Information Center (DTIC). All others should apply to the National Technical Information Service (NTIS).

If your address has changed, if you wish to be removed from the mailing list, or if the addressee is no longer employed by your organization, please notify PL/IM, 29 Randolph Road, Hanscom AFB, MA 01731-3010. This will assist us in maintaining a current mailing list.

Do not return copies of this report unless contractual obligations or notices on a specific document require that it be returned.

REPORT DOCUMENTATION PAGE			Form Approved OMB No. 0704-0188	
Public reporting burden for this collection of information is estimated to average 1 hour per response, including the time for reviewing instructions, searching existing data sources, gathering and maintaining the data needed, and completing and reviewing the collection of information. Send comments regarding this burden estimate or any other aspect of this collection of information, including suggestions for reducing this burden, to Washington Headquarters Services, Directorate for Information Operations and Reports, 1215 Jefferson Davis Highway, Suite 1204, Arlington, VA 22202-4302, and to the Office of Management and Budget, Paperwork Reduction Project (0704-0188), Washington, DC 20503.				
1. AGENCY USE ONLY (Leave blank)	2. REPORT DATE May 1995	3. REPORT TYPE AND DATES COVERED SCIENTIFIC		
4. TITLE AND SUBTITLE PROCEEDINGS OF THE ENVIRONMENTAL SITE CHARACTERIZATION AND MONITORING BASIC RESEARCH PROGRAM 1995 CONTRACTOR/GRANTEE MEETING, 11-12 MAY 1995		5. FUNDING NUMBERS PE 61102F PR 2302 TA GN WU 01		
6. AUTHOR(S) EDITORS: DR. KATHARINE KADINSKY-CADE DR. STEVEN CARDIMONA				
7. PERFORMING ORGANIZATION NAME(S) AND ADDRESS(ES) PHILLIPS LABORATORY/GPE 29 RANDOLPH ROAD HANSCOM AFB, MA 01731-3010		8. PERFORMING ORGANIZATION REPORT NUMBER PL-TR-95-2047 ERP, No. 1170		
9. SPONSORING / MONITORING AGENCY NAME(S) AND ADDRESS(ES) AFOSR/NA 110 DUNCAN AVENUE, SUITE B115 BOLLING AFB, DC 20332-0001		10. SPONSORING / MONITORING AGENCY REPORT NUMBER		
11. SUPPLEMENTARY NOTES THIS RESEARCH WAS SUPPORTED BY THE AIR FORCE OFFICE OF SCIENTIFIC RESEARCH (AFOSR) UNDER PE 61102F.				
12a. DISTRIBUTION / AVAILABILITY STATEMENT APPROVED FOR PUBLIC RELEASE: DISTRIBUTION UNLIMITED			12b. DISTRIBUTION CODE	
13. ABSTRACT (Maximum 200 words) These Proceedings contain papers presented at the first contractor/ grantee meeting for AFOSR's basic research program in Environmental Site Characterization and Monitoring (SCM). Researchers from the SCM program and select researchers from AFOSR's Electromagnetics program are joined by several researchers supported by the Army Research Office in a meeting intended to exchange ideas and support future interactions. The scientific objective of the symposium is to address fundamental questions which currently prevent and/or will enable the application of geophysical science to the problem of environmental SCM.				
14. SUBJECT TERMS ENVIRONMENTAL SITE CHARACTERIZATION, ENVIRONMENTAL SITE MONITORING, ELECTROMAGNETICS, NEAR SURFACE GEOPHYSICS, HYDRAULIC PROPERTIES.			15. NUMBER OF PAGES 84	
			16. PRICE CODE	
17. SECURITY CLASSIFICATION OF REPORT UNCLASSIFIED	18. SECURITY CLASSIFICATION OF THIS PAGE UNCLASSIFIED	19. SECURITY CLASSIFICATION OF ABSTRACT UNCLASSIFIED	20. LIMITATION OF ABSTRACT UL	

TABLE OF CONTENTS

	PAGE
Barrash, Warren; Donaldson, Paul; Michaels, Paul; Pelton, Jack; Urban, Scott <i>Joint Inversion of Hydrologic and Geophysical Data for Permeability Distribution in an Alluvial Aquifer.....</i>	1
Blanch, Joakim O.; Symes, William W.; Versteeg, Roelof <i>Linearized Inversion in Attenuative Media-A Viscoelastic Example..</i>	10
Borup, David T.; Johnson, Steven A. <i>Theoretical and Experimental Research Studies of Full Vector, 3-D, Quantitative Inverse Scattering, Ground Penetrating Radar.....</i>	16
Cardimona, Steve; Kadinsky-Cade, Katharine <i>Integrated Geophysical Methods for Environmental Site Characterization and Monitoring.....</i>	21
Knight, Rosemary <i>Characterizing Scale Dependent Hydraulic Properties with measurement of Dielectric properties.....</i>	27
Olhoeft, Gary <i>Noninvasive Complex Resistivity Measurements of Clay-Organic Processes to Map Organic Contamination and Degradation of Clay Barriers.....</i>	33
Papanicolaou, George <i>Underground Imaging in High Contrast Cases.....</i>	38
Scales, John; Tsvankin, Ilya <i>Modeling and Inversion of Shallow Seismic Data Including Nongeometric Waves.....</i>	39
Sternberg, Ben K.; Dvorak, Steven L. <i>Basic Research on Three-Dimensional (3D) Electromagnetic (EM) Methods for Imaging the Flow of Organic Fluids in the Subsurface.</i>	42
Wang, Yun <i>A PDE Based Approach to Dispersive Inverse Problems.....</i>	48

LATE ABSTRACTS

PAGE

- Carin, Lawrence; Felsen, Leopold B.**
Ultra-Wideband Techniques for Classification and Imaging of Buried Targets..... 54
- Deming, R.; Devaney, A.J.**
Processing Experimental Ground Penetrating Radar Data..... 60
- Lesmes, David; Jouniaux, Laurence; Morgan, Dale**
Frequency Dependent Electrokinetic Studies of Rocks and Soils..... 68
- Morris, J.B.; Fiddy, M.A.**
Nonlinear Filtering Applied to Single-View Backpropagated Images of Strong Scatterers..... 73

Accession For	
NTIS	CRA&I <input checked="" type="checkbox"/>
DTIC	TAB <input type="checkbox"/>
Unannounced <input type="checkbox"/>	
Justification	
By	
Distribution /	
Availability Codes	
Dist	Avail and/or Special
A-1	

PROCEEDINGS

Environmental Site Characterization and Monitoring Basic Research Program 1995 Contractor/Grantee Meeting

11-12 May 1995

Conducted at

**PHILLIPS LABORATORY
29 Randolph Road
Hanscom AFB, Massachusetts 01731-3010**

Sponsored by

**AIR FORCE OFFICE OF SCIENTIFIC RESEARCH
110 Duncan Avenue, Suite B-115
Bolling AFB, DC 20332-0001**

**THE VIEWS AND CONCLUSIONS CONTAINED IN THIS DOCUMENT ARE THOSE OF THE
AUTHORS AND SHOULD NOT BE INTERPRETED AS REPRESENTING THE OFFICIAL POLICIES,
EITHER EXPRESSED OR IMPLIED, OF THE U.S. AIR FORCE**

JOINT INVERSION OF HYDROLOGIC AND GEOPHYSICAL DATA FOR PERMEABILITY DISTRIBUTION IN AN ALLUVIAL AQUIFER

Warren Barrash, Paul Donaldson, Paul Michaels, Jack Pelton and Scott Urban
Center for Geophysical Investigation of the Shallow Subsurface
Boise State University, Boise, Idaho

Abstract

We are in the first year of a three-year field and modeling study to map permeability and hydrostratigraphy in a heterogeneous alluvial aquifer by extending control at wells with non-invasive geophysical investigation methods. Our efforts build upon recent work [1, 2] which used laboratory-derived relationships between permeability and seismic P-velocity, and joint inversion of synthetic data sets, to demonstrate the feasibility of determining the distribution of permeability in a heterogeneous aquifer without requiring information from a dense network of wells.

The aquifer under study is a heterogeneous alluvial system with 50-70 ft (15-20 m) of saturated thickness above a clay layer at the 25-acre Capital Station remediation site in Boise, Idaho (Fig. 1A). Our approach is to use seismic methods (reflection, refraction, surface wave dispersion), ground penetrating radar, resistivity, and time-domain electromagnetic methods (Fig. 1B) to determine site-wide subsurface distributions of seismic velocity (P-wave and S-wave), dielectric constant, and resistivity. Profiles of hydrostratigraphy and permeability are being obtained from wells (Fig. 1C) with geophysical logging, sampling/coring, vertical seismic profiling and multiple-well pumping tests.

Borehole and laboratory data will be used to develop a locally valid empirical relationship between permeability and geophysical parameter space expressed in terms of radial basis functions. An important part of the analysis will be determining which parts of geophysical parameter space make the greatest contributions in the determination of permeability. The empirical relationship will be tested by examining its predictive ability at individual well locations, and then it will be applied to generate a distribution of permeability throughout the study area.

Geologic and Geophysical Logs. Drilling logs from existing wells describe a generalized two-layer stratigraphy in the saturated zone with cobbles in a sand matrix overlying a sand unit, and these data suggest a directional depositional fabric trending NNW. More detailed interpretations of stratigraphy and physical properties at individual wells come from borehole geophysical logs (e.g., Figs. 2-3), and from samples or core from new wells at the site. Neutron, natural gamma, resistivity, conductivity and temperature logs were run in 8 deep and 9 shallow wells in 1994 by the U.S. Geological Survey Borehole Geophysics Research Project (Fig. 1C); a second round of logging is planned for 1995 to investigate remaining monitoring wells and new wells. Core samples (disturbed) from sands in one well are being analyzed for V_p , V_s , grain density, grain size distribution, porosity and permeability; we are collaborating with rock physics researchers at Stanford [1, 2] on analysis and interpretation of these samples.

Aquifer Tests. Fourteen multiple-well aquifer tests have been run at the site where wells are screened in different intervals (Fig. 1C), including tests in four areas where two or more wells were used alternately for pumping and observation (e.g., Fig. 2). Simple 1- or 2-layer analytical or numerical models of the system do not adequately match observed behavior. Modeling of local areas pumped with several wells using the axisymmetric option of MODFLOW gives reasonable matches if additional layers are added to delay onset of drawdown in observation wells. Where available, borehole geophysical logs and core samples provide control to assist development of layered models (Fig. 2B). Permeability (or hydraulic conductivity) of layers ranges over 3 orders of magnitude with clean sands being the most permeable units. At least 7 more tests will be run in remaining monitoring wells, and additional tests will be run as new wells are emplaced.

Vertical Seismic Profiles. Vertical seismic profiles of P- and S-wave velocity in three boreholes (Fig. 1C) were run in 1994 using two downhole geophone tools. Repeatable horizontal and vertical hammer sources were used to acquire 3-component data from which broad-band first arrival time measurements have been made (e.g., Fig. 3). Figure 3C shows a vertical travel-time profile. As expected, the water table provides the largest discontinuity in P-wave velocity. However, the similar change in S-wave velocity was unexpected because S-waves should be relatively insensitive to variations in pore fluid content. In addition, the P-wave reflection image suggests that mode conversions are occurring at the water table. As a result, we are evaluating the potential value of offset-dependent observations for future surface seismic work. In Figure 3B, the silty-sand layer (15-19 m depth) appears to generate a good S-wave reflection, making this also a possible objective for future S-wave reflection work. Fine scale velocity anomalies within the saturated zone are also apparent in the travel time data (Fig. 3C). These fluctuations are most noticeable on the P-wave times. We hope to relate the P-wave variations to changes in hydrologic properties by using the S-waves as a datum.

Future plans include development of a downhole geophone tool that will fit in 2-inch boreholes and couple with a mechanical, rather than pneumatic, mechanism in order to collect high-quality S-wave data in standard monitoring wells. Also we plan to explore the attenuation and phase-velocity dispersion in the full waveform data. We hope to achieve vertical resolution of 4 m from these measurements.

Surface Wave Dispersion. Dispersion of seismic surface waves may be used to infer near-surface physical properties. In particular, the profile of shear-wave velocity (V_s) with depth may be inferred from the dispersion of Rayleigh waves. Measurements of Rayleigh-wave dispersion were carried out at the Capital Station site to independently confirm V_s data obtained from downhole seismic VSP experiments, and to test the feasibility of using surface-wave techniques as a low-cost method for extending VSP results away from boreholes.

The Capital Station seismic experiments show that Rayleigh waves are easily generated and recorded along profiles of approximately 100-m length virtually anywhere on the site. Preliminary interpretations of phase-velocity dispersion curves for the fundamental Rayleigh-wave mode are based on a simple single layer over half-space velocity model. These interpretations show that estimates of V_s are consistent with estimates derived from nearby VSP experiments, but that VSP-derived interface depths are greater than Rayleigh-wave

interpretations by a factor of 160-200% (Table 1). One explanation for the differences in

TABLE 1. Comparison of shear-wave velocity estimates derived from Rayleigh-wave dispersion data and VSP measurements in boreholes. Velocity model is single layer over a half-space. Wells chosen for comparison are those with VSP measurements located closest to seismic lines 2W (well 14) and 2N (well ST3).

	Layer V_s	Half-Space V_s	Interface Depth
Line 2W	180 m/s	400 m/s	2.8 m
Well 14	180 m/s	380 m/s	4.5 m
Line 2N	150 m/s	370 m/s	3.1 m
Well ST3	170 m/s	430 m/s	5.9 m

interface depth may be the fact that the Rayleigh-wave estimates represent averages over a 100-m profile, whereas the VSP data are point measurements offset to one end of the seismic lines. However, because the VSP data indicate that the interface is the water table, and because it is unlikely that the average water table depth beneath the seismic line differs significantly from the depth at the well, it appears that a systematic bias may exist in the preliminary Rayleigh-wave interpretations. It is probable that this discrepancy is related to non-uniqueness in the inversion procedure and is under active investigation.

An example of the Rayleigh-wave data and dispersion analysis is shown in Figure 4 where seismic records for lines 2W and 2N (about 300 m apart, Fig. 1B) are presented for comparison. Both lines were shot with the same source-receiver geometry (Fig. 4A). Rayleigh waves dominate the seismograms within the triangular windows bracketed by the white lines, but the window for line 2N is longer in duration than for line 2W, indicating more dispersion and a concomitant greater stretching of the waveforms. This difference is reflected in the phase-velocity dispersion curves where the overall slope of the 2N data is greater than the slope of the 2W data (Fig. 4B). Despite the clear differences in the recorded data for lines 2W and 2N, the associated velocity models are not greatly different (Fig. 4C), suggesting that dispersion is a sensitive phenomenon for the range of model parameters under consideration. These preliminary results indicate that additional work on the surface-wave dispersion method is warranted, with emphasis on: increasing the bandwidth (especially at lower frequencies); inclusion of higher modes beyond the fundamental mode; observations of horizontally polarized surface waves (Love waves); and consideration of more complicated velocity models.

Resistivity Soundings. Preliminary resistivity data from 8 profiles acquired in the fall of 1994 (Fig. 1B) have been inverted, and compared and correlated with lithologic logs and geophysical logs. Some soundings (in northwest of site) appear to be contaminated by lateral disturbances. The best correlations are observed in the southeast part of the site where the soundings reflect changes observed in lithologic and geophysical logs. Sounding 2N (Fig. 1B) has been included as an example (Fig. 5). These observations predict probable success for our planned Transient EM (TEM) experiments. The TEM technique is noted for minimizing lateral effects from vertical soundings. We will be experimenting on-site, seeking the minimum-diameter transmitter loop feasible. Minimizing this parameter corresponds to optimizing lateral resolution in our attempts to image the subsurface resistivity distribution which in turn can be correlated to porosity/permeability.

Ground Penetrating Radar. Tests of ground penetrating radar (GPR) along a single profile (Fig. 1B) suggest that GPR measurements will produce little useful information. The tests were conducted using a Sensors and Software pulseEKKO IV unit with separable source and receiver. Common midpoint experiments using 25-MHz, 50-MHz and 100-MHz antennas failed to provide convincing evidence of any subsurface reflectors. Independent resistivity measurements (Fig. 5) indicate that the unsaturated zone is relatively conductive ($5\text{-}25 \times 10^{-3}$ S/m), thereby limiting the usefulness of GPR through severe attenuation of the electromagnetic waves.

Acknowledgement/Disclaimer

This work is sponsored by the Army Research Office under grant number DAAH04-94-G-0271. The views and conclusions contained herein are those of the authors and should not be interpreted as necessarily representing the official policies or endorsements, either expressed or implied, of the Army Research Office or the U.S. Government. Access to the field site and operational data are provided by S-Sixteen and Anderson and Associates. Geophysical logging was performed by Dr. R.H. Morin, U.S. Geological Survey, as part of a cooperative research effort. Center for Geophysical Investigation of the Shallow Subsurface (CGISS) technical report 95-08.

References

1. Copt, N., Yoram, R., and Mavko, G., Geophysical-hydrological identification of field permeabilities through Bayesian updating, *Water Resources Research*, 29, 2813-2825, 1993.
2. Rubin, Y., Mavko, G. and Harris, J., Mapping permeability in heterogeneous aquifers using hydrologic and seismic data, *Water Resources Research*, 28, 1809-1816, 1992.

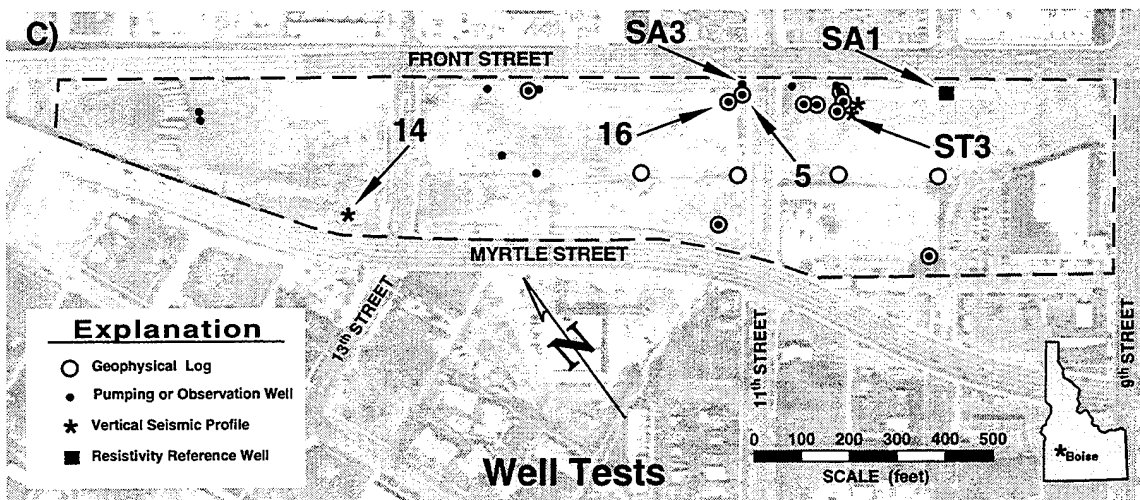
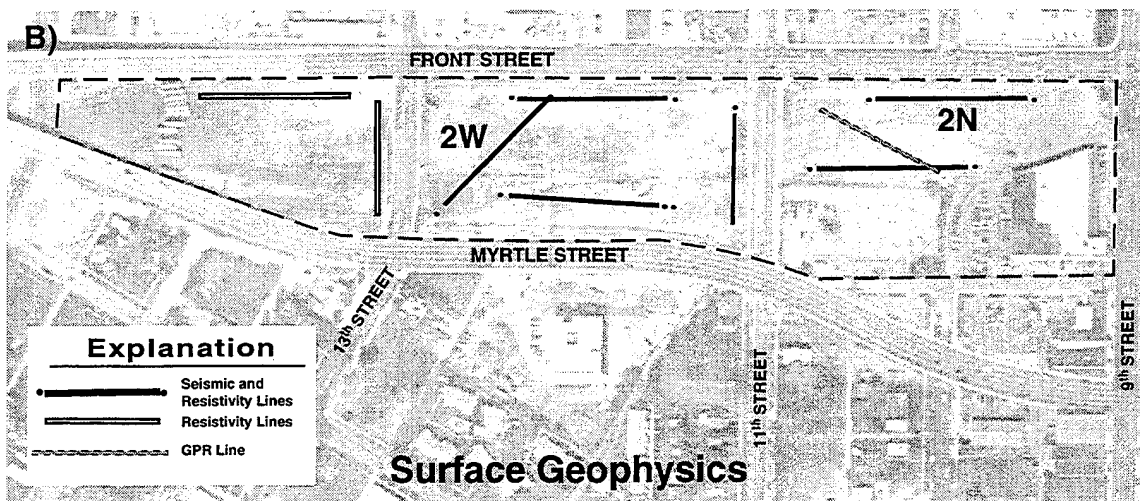
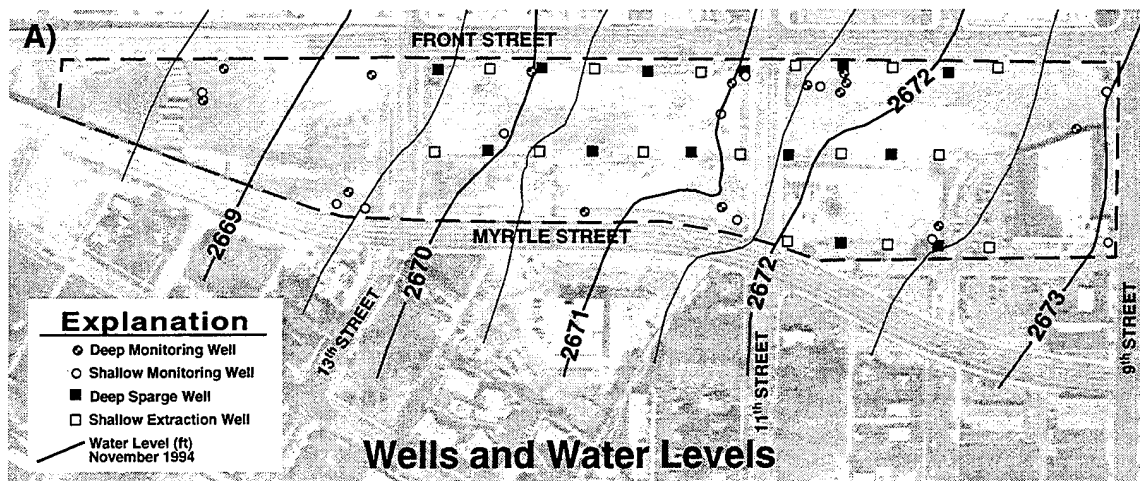


Figure 1. Capital Station site (within dashed line), downtown Boise, Idaho. A) Shallow wells are <25 ft deep and open across the water table in the cobble unit. Deep wells are 50–85 ft deep and open within the sand unit. B) Surface geophysical lines run in 1994. C) Wells tested geophysically and hydrologically in 1994.

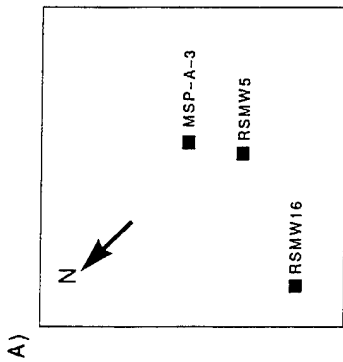
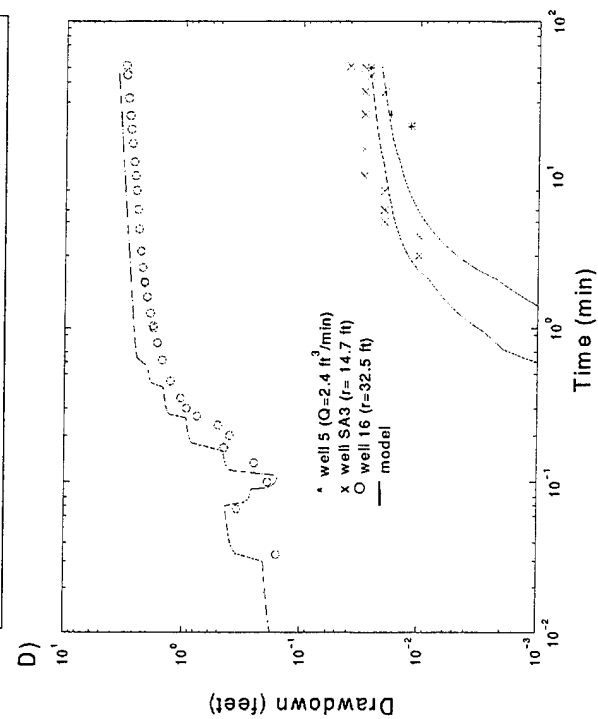
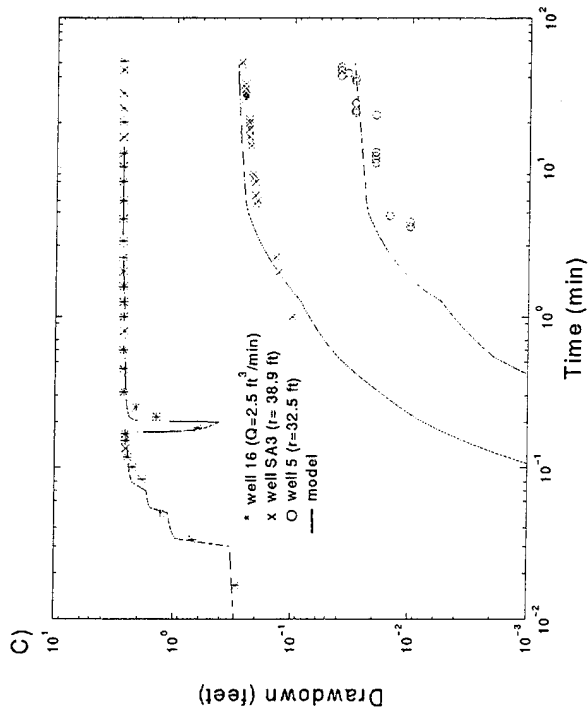
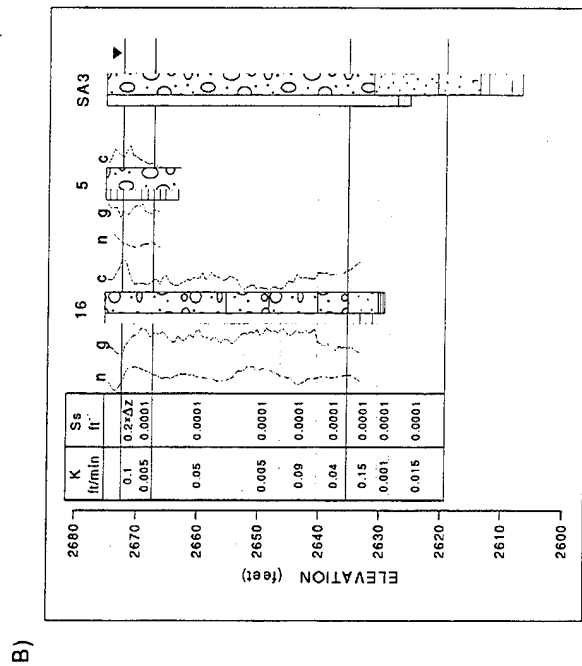


Figure 2. Modeling of multiple-well pumping test results at wells 16, 5, and SA3. A) Relative well locations. B) Well log data and layering used to model responses to pumping at wells 16 (C) and 5 (D). Symbols: n (neutron log), g (natural gamma log), c (electrical conductivity log).



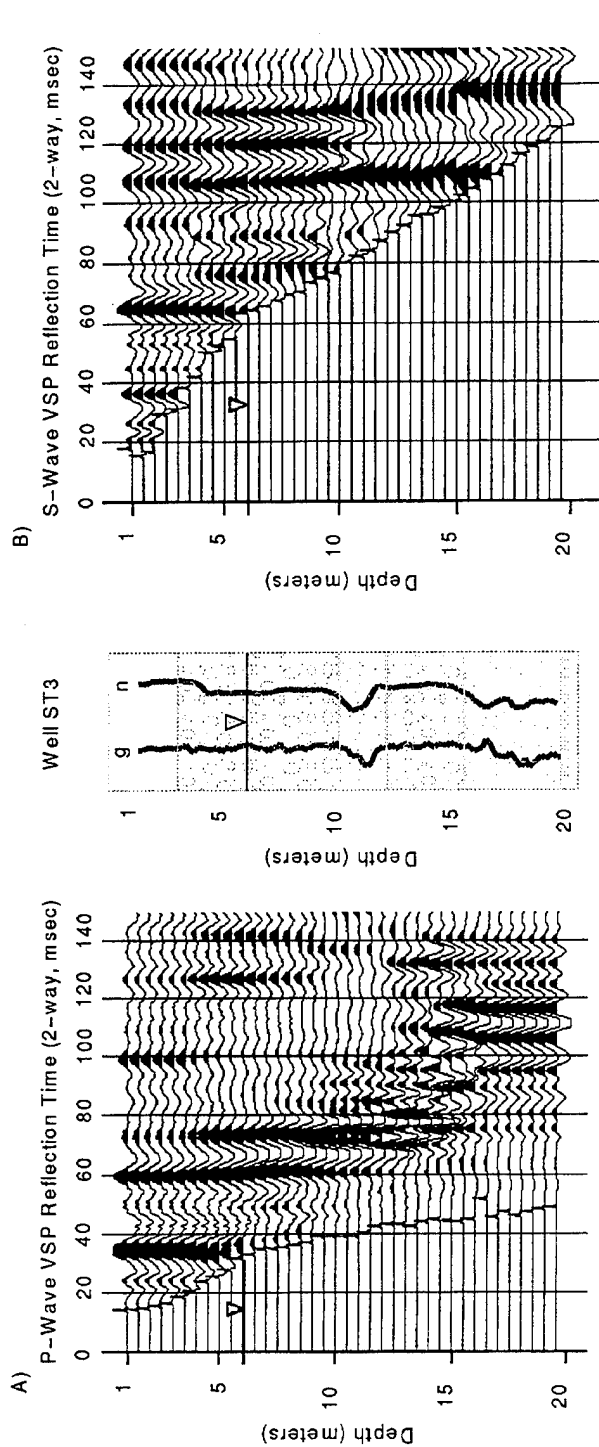
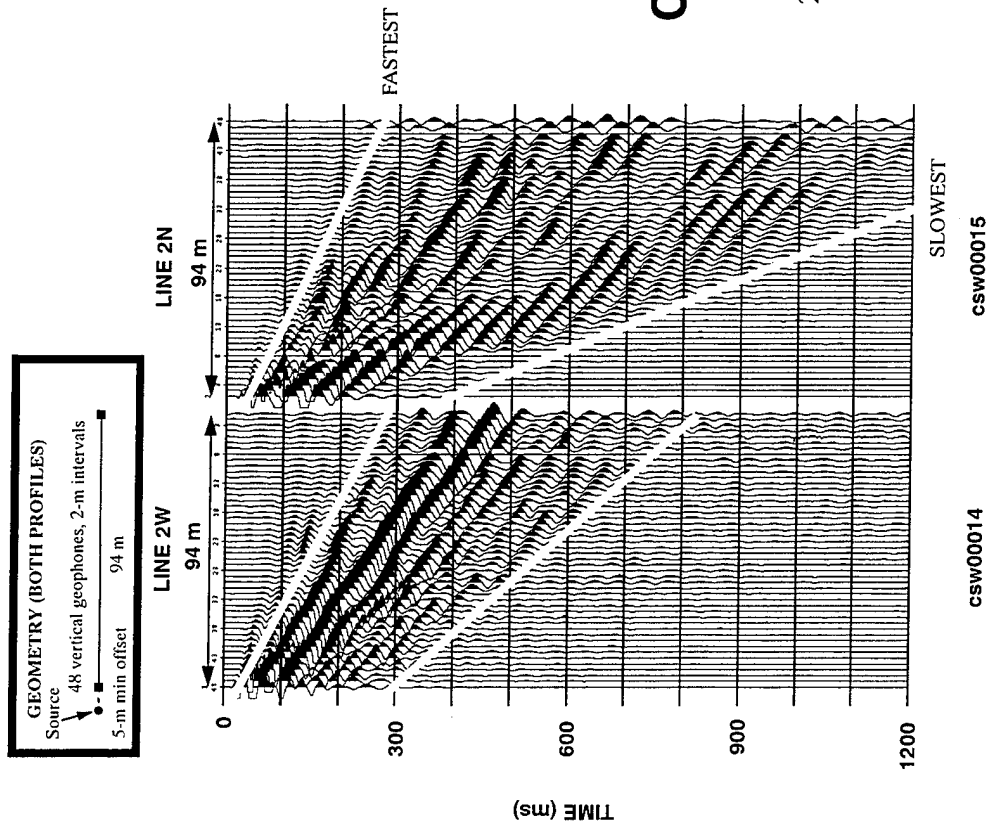
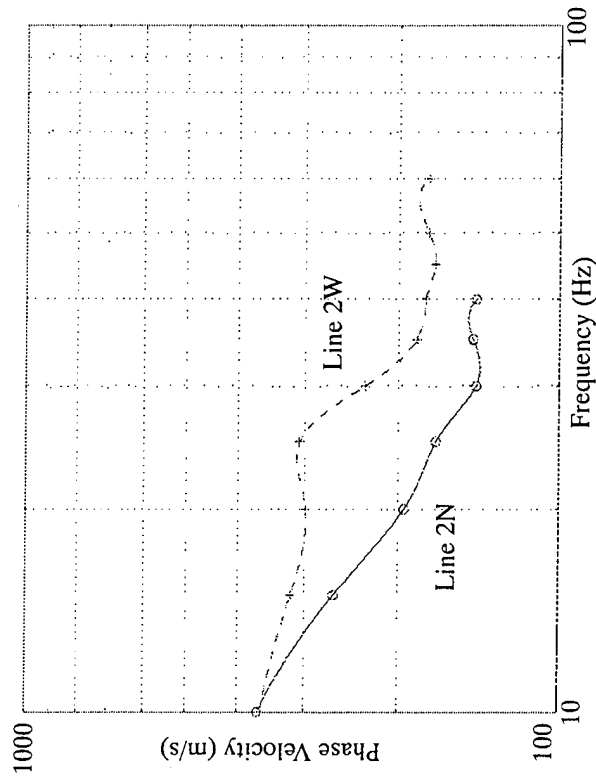


Figure 3. VSP at ST3. Wavefield separation methods were applied to the 3-component VSP. A) Up-going P-wave reflections recorded (vertical component) from a repeatable vertical hammer source. Note the strong reflection at the water table (6 m depth). Delayed arrivals of the deeper reflections suggest mode conversions (P to S) may have occurred at the water table. B) Horizontal geophone waveforms from a repeatable horizontal hammer source. A strong S-wave reflection occurs at the water table depth. C) Direct wave travel times as measured from the broad-band waveforms. The break in slope at the water table indicates the changes in velocity for both the P and S waves that contributed to the reflections imaged in A and B. Symbols: g (natural gamma log), n (neutron log).

A) Seismic Records



B) Dispersion Data



C) Shear-Wave Velocity Models



Figure 4. Seismic surface wave data and preliminary interpretations for Lines 2W and 2N at Capital Station site: A) 48-channel records with surface-wave window indicated by white lines, traces scaled individually; B) phase-velocity dispersion curves; C) preliminary single layer over half-space shear-wave velocity models interpreted from phase-velocity dispersion curves.

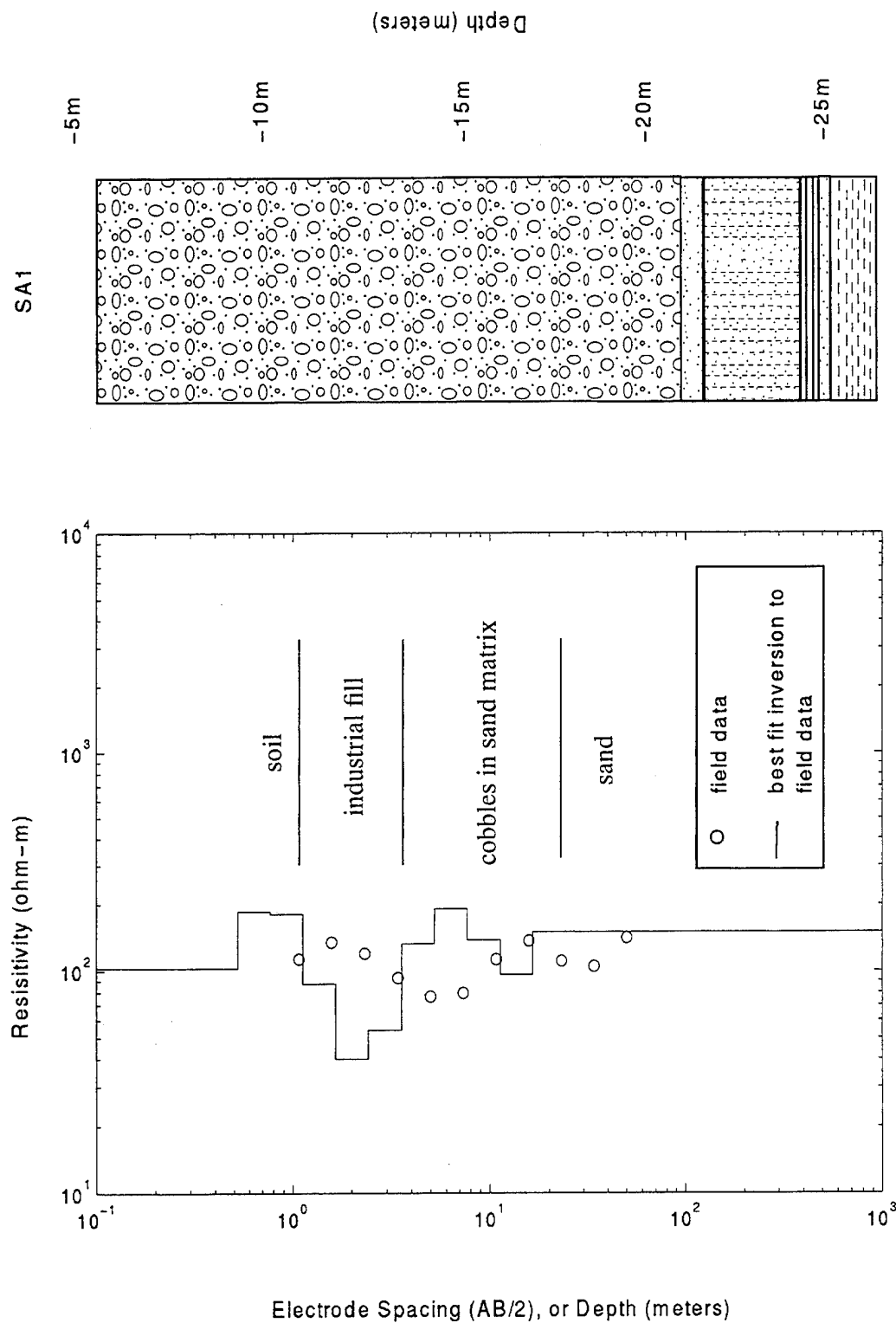


Figure 5. Schlumberger resistivity sounding 2N (see Fig. 1B) centered on well SA1. Depth scale for resistivity interpretation is logarithmic; depth scale for lithologic log is linear. Note that lithologic log starts below a depth of 5 m (below the top of the cobble layer). The resistivity data do not distinguish layers beneath the base of the cobbles.

LINEARIZED INVERSION IN ATTENUATIVE MEDIA - A VISCOELASTIC EXAMPLE

Joakim O. Blanch

Department of Geology and Geophysics
Rice University, Houston TX 77251-1892

William W. Symes

Department of Computational and Applied Mathematics,
Rice University, Houston TX 77251-1892

Roelof Versteeg

Department of Geology and Geophysics
University of Connecticut, Storrs, CT 06269-2045

Summary The adjoint state computation is essential for iterative linearized inversion using full wave equation simulation. For dissipative systems like viscoacoustics however this computation appears to require storage of the entire time history of the forward reference field, or else its recomputation at every time step, both prohibitively expensive in a multidimensional setting. The computational complexity and storage requirements can both be reduced to a level only exceeding that of the forward computation by a logarithmic factor, through retention of a few carefully selected intermediate time levels during the forward calculation. The feasibility of the resulting adjoint state computation is illustrated by linearized viscoacoustic 2D inversion of a small part of a field seismic data set.

The Rice Site Characterization Project The project plan includes two major emphases: development of modeling methods for ground penetrating radar waves, and employment of these methods to evaluate the potential of inversion of GPR data as a tool for hazardous waste site characterization and monitoring. Modeling issues to be studied include accuracy and efficiency of explicit finite element methods in smooth and irregular models, and approximation of complex boundary conditions and antenna simulation. Inversion issues will echo those studied in The Rice Inversion Project for exploration scale seismology: estimation of the velocity field (index of refraction), calibration of sources, and effects of attenuation and dispersion on linearized inversion for wavelength scale features. As attenuation and dispersion are of considerably greater importance in shallow seismology and GPR studies than in exploration seismology, this presentation reviews some recent work of our group on viscoelastic inversion and its application to seismic field data.

Linearized Inversion The linear viscoelastic wave equation may be written in the form

$$\frac{\partial U}{\partial t} = LU + F; \quad U, F \equiv 0, \quad t \ll 0$$

Here the vector U consists of particle velocity and stress components, as well as so called memory variables which permit a differential implementation of the viscous stress-strain relation. The resulting system is quite similar to Maxwell's equations with Debye-type relaxation modeling. The coefficients of the partial differential operator L are (functions of) the mechanical parameters of the viscoelastic medium, such as density, wave velocities, and relaxation times, and express Newton's law and the constitutive relation (generalized Hooke's law) of the material. The vector valued function F models the energy source mechanism. Finally let M denote the measurement operator, i.e. sampling at receivers.

The linearized forward map relates perturbations in the coefficients of L to the corresponding perturbations in MU . The least squares formulation of the linearized inverse problem consists in minimizing the mean square error $\|M\delta U - \delta D\|^2$, where δD is the residual data not already explained by the current reference model (coefficients of L). Minimization by descent methods requires calculation of the gradient, which in turn demands computation of the adjoint operator to $\delta L \mapsto M\delta U$. The following trick computes the adjoint: solve the final value problem

$$\frac{\partial W}{\partial t} = -L^*W + M^*\Phi; \quad W \equiv 0, \quad t \gg 0$$

Then integration by parts shows that $\langle \Phi, M\delta U \rangle = \langle W, \delta LU \rangle$ where the angle brackets represent appropriate L^2 inner products. From this formula one reads off the adjoint of the linearized map, hence the gradient of the mean square error (using $\Phi = \delta D$).

For more details on of linearized inversion in viscoacoustic media see [1], also Tarantola [4].

Recomputation scheme As one sees from last two equations, calculation of the adjoint map involves accessing the solutions of initial and final value problems at the same instant of time. One could recompute the solution of the initial value problem for each time step (after discretization!), or retain in core memory the entire solution of the initial value problem, not just the simulated measurements. For problems in more than one space variable, both alternatives are infeasibly expensive. A third, compromise alternative saves a number of "snapshots" (intermediate complete states, or Cauchy data) and restarts the computation. We call such an approach a *recomputation scheme*. Griewank [2] devised a recomputation scheme which is optimal in both computation effort and memory use. It allows for logarithmic growth in computation effort and memory with linearly increasing problem size. We have adapted Griewank's scheme to linearized viscoacoustic inversion.

The algorithm is very efficient. For 10,000 timesteps, memory available for only 10 snapshots (out of 10,000 for a "store it all" algorithm) is sufficient to limit the computational effort to roughly 3 times more than for a "store it all" algorithm. For merely 5 available snapshots, roughly 5 times larger computational effort is sufficient.

Viscoacoustic Inversion of the Mobil AVO data set In 1994 Mobil Research and Development Corporation made a marine data set publicly available for Amplitude - Versus - Offset ("AVO" - roughly synonymous with "linearized inversion") studies. Many research groups, including TRIP, presented initial results at a Society of Exploration Geophysicists workshop in 1994 entitled "Comparison of seismic inversion methods on a single real dataset", organized by Robert Keys and Douglas Foster. The data is supplemented by measurements in several nearby wells.

To demonstrate the viscoacoustic algorithm we performed two crude linearized inversions of a (small) part of the data set, one with physically realistic attenuation and one with no attenuation (elastic modeling). We selected nine shot records located close to one of the wells. Preprocessing included multiple reflection removal (to make the linearization hypothesis more accurate), amplitude compensation (to enable 2D treatment of data recorded in 3D), editing, downfiltering to allow use of a coarser finite difference grid, and source ghost removal. Background (smooth) velocity, bulk modulus, density, and attenuation models were derived from the well log and vertical seismic profile data. The background fields were assumed to depend only on depth, and are smooth on the wavelength scale. The linearized inversion is designed to recover the wavelength scale fluctuations ("reflectivity") in bulk modulus and density, treated as perturbations of the background fields.

The forward and adjoint state computations were based on a finite difference simulator for viscoelastic waves developed at Rice ([3]), coupled to generic optimization software. Five steps of the conjugate residual algorithm required approximately 10 CRAY C90 CPU hours, reducing the normal residual in each experiment to roughly 20% of its initial value. Use of 64 MW of memory accommodated 20 snapshots, which made 3 recomputations using Griewank's scheme sufficient to compute the adjoint involving 2272 timesteps. The total of floating point operations was increased by less than 100 percent over that needed by a "store it all" algorithm.

The inverted wavelength scale fluctuations in bulk modulus are shown in Figure 1; the analogous density result is very similar. Figure 2 and 3 show cross sections of the parameter estimate from viscoacoustic and acoustic inversion, bulk modulus and density reflectivity respectively, to more clearly show the difference between the results from the viscoacoustic and acoustic inversion. The shallow reflectors are the same for the viscoacoustic and acoustic inversion, but deeper reflectors are underestimated in the purely acoustic inversion. The positions of the reflectors are also slightly shifted due to dispersion in the more realistic viscoacoustic medium. The bulk modulus and density reflectivity are for the most part completely correlated. Figure 4 shows one of the few places in the estimates where they are not correlated (1800 *m* depth and 840 *m* offset). There is a zero crossing in the density reflectivity, with hardly any accompanying wiggle in the bulk modulus reflectivity. This anomaly could indicate a significant lithological change. The result is very preliminary, since the normal equations have been solved rather imprecisely.

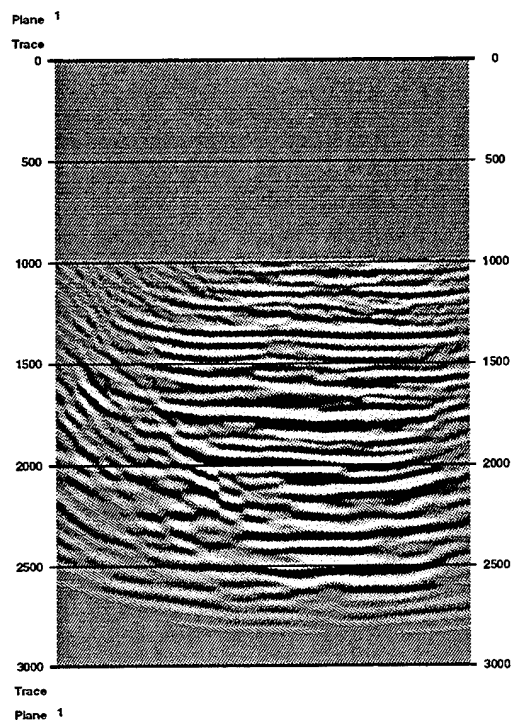


Figure 1: The estimated bulk modulus from viscoacoustic inversion. Reflectivity was not estimated above 1000 *m* depth, roughly corresponding to mute of the data. Depth scale in meters. Aspect ratio approximately 1:1

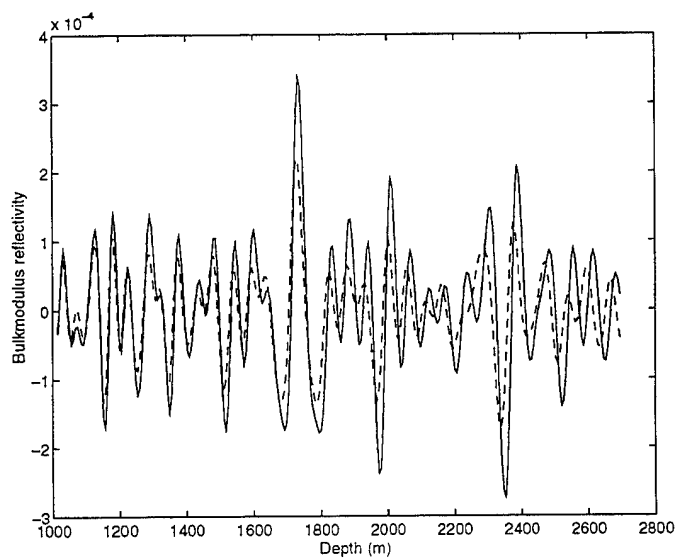


Figure 2: A depth cross section of the estimated bulk modulus reflectivity at 750 *m* offset. Solid - Estimate from viscoacoustic inversion. Dashed - Estimate from acoustic inversion.

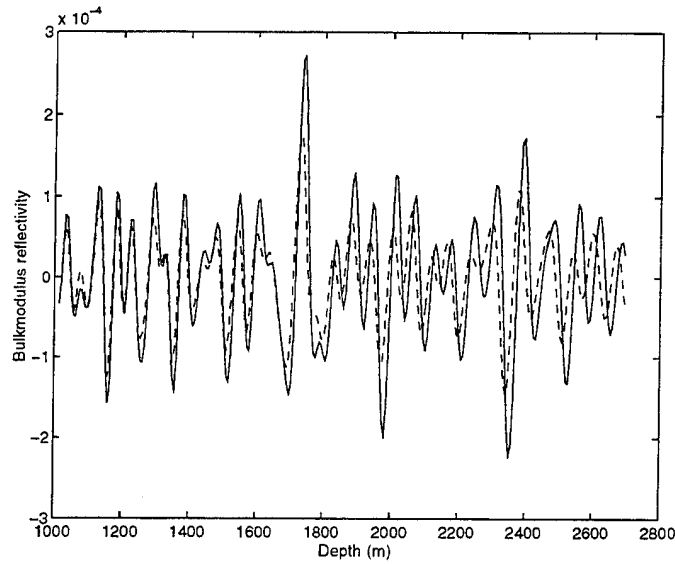


Figure 3: A depth cross section of the estimated density reflectivity at 750 *m* offset. Solid - Estimate from viscoacoustic inversion. Dashed - Estimate from acoustic inversion.

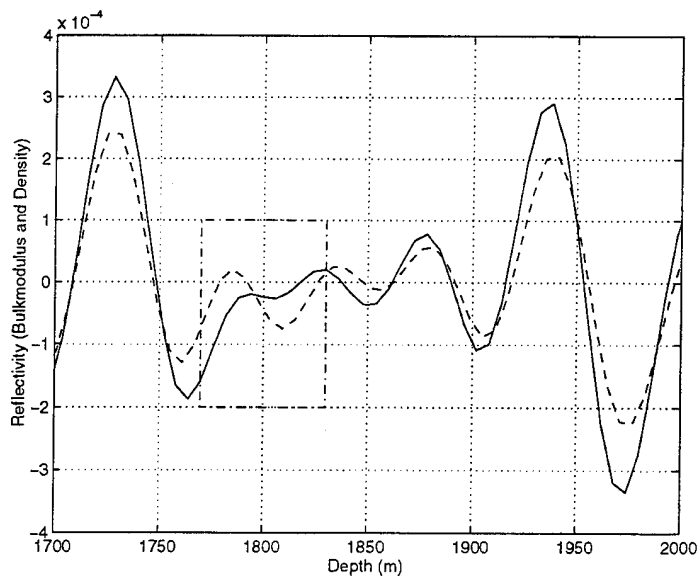


Figure 4: A depth cross section of the estimated bulk modulus and density reflectivity at 840 *m* offset. Solid - Estimated bulk modulus reflectivity. Dashed - Estimated density reflectivity. Dash-dotted encircled area contains the anomaly.

Conclusions Griewank's algorithm decreases computational cost and storage requirements dramatically for calculations of adjoints of non-conservative systems. The use of the algorithm enabled a viscoacoustic inversion of a real data set.

Reflectivity is consistently underestimated and incorrectly located if anelastic effects are neglected. Inversion of the Mobil AVO data set revealed a tentative reflectivity anomaly below a prominent reflector, which could point to an interesting lithology.

The methods developed by our group for viscoacoustic inversion will apply as well to other dissipated transient inverse problems, and specifically to GPR inversion. Interestingly, radar waves penetrate only one third to one half as many wavelengths into the subsurface, even under ideal conditions, as do seismic waves at exploration wavelengths. Therefore finite difference and finite element based inversion, barely within the realm of feasibility for exploration seismology, should be a viable approach for GPR processing.

Acknowledgments This work was partially supported by ONR grant N00014-89-J1115, NSF, IBM, the Schlumberger Foundation, the Texas Geophysical Parallel Computation Project, and The Rice Inversion Project. TRIP Sponsors for 1995 are Advance Geophysical, Amerada Hess, Amoco Production Co., Conoco Inc., Cray Research Inc., Discovery Bay, Exxon Production Research Co., Interactive Network Technologies, Mobil Research and Development Corp., and Texaco Inc.

References

- [1] J. O. Blanch and W. W. Symes. Linearized inversion in viscoelastic media. In O. Diachok, A. Caiti, P. Gerstoft, and H. Schmidt, editors, *Full field inversion methods in ocean and seismic acoustics*. Kluwer Academic Publishers, 1995. In press.
- [2] A. Griewank. Achieving logarithmic growth of temporal and spatial complexity in everse automatic differentiation. *Optimization Methods and Software*, 1:35-54, 1992.
- [3] J. O. A. Robertsson, J. O. Blanch, and W. W. Symes. Viscoelastic finite-difference modeling. *Geophysics*, 59:1444-1456, 1994.
- [4] A. Tarantola. Theoretical background for the inversion of seismic waveforms, including elasticity and attenuation. In A Aki and R. S. Wu, editors, *Scattering and attenuation of seismic waves, PAGEOPH*. Birkhäuser Verlag, Basel, 1988.

THEORETICAL AND EXPERIMENTAL RESEARCH STUDIES OF FULL VECTOR 3-D QUANTITATIVE INVERSE SCATTERING GROUND PENETRATING RADAR

David T. Borup
TechniScan Inc.
Salt Lake City, Utah

Steven A. Johnson
TechniScan Inc.
Salt Lake City, Utah

Abstract

Recent advances in inverse scattering algorithms, coupled with the availability of 1-10 GFLOP computer technology, have made the application of vector electromagnetic inverse scattering methods to GPR imaging problems practical. Inverse scattering methods offer the promise of quantitative reconstruction of the 3-D variation of dielectric constant and conductivity (and possibly the magnetic parameters) in the earth.

TechniScan Inc. (TSI) has developed a variety of algorithms for the simulation of scalar and vector EM scattering problems in two and three dimensions [1-4]. These algorithms include frequency domain integral equation (FDIE), finite-difference-time domain (FDTD), and frequency domain recursion (for example, one way parabolic spatial marching) methods. Exact Bessel series solutions for circular cylindrical (2-D) objects buried in a vertically stratified medium illuminated by 3-D scalar and vector fields have also been developed for testing the accuracy of the general scattering methods. The FDIE algorithms are particularly advanced and have been successfully applied to scalar (TM polarization) 1-12.4 GHz laboratory GPR data for 2-D cylindrical targets (Figures 1-5). Extension of the algorithms and experimental hardware to 3-D vector GPR is the major goal of our present research. The results of simulations and laboratory experiments will be shown.

A critical component of a successful GPR imaging approach is the accurate calibration of the antenna fields in the earth. Inverse scattering methods require an accurate model of the magnitude and phase of the applied field in the absence of the targets (incident field) for both the transmitting and receiving antennas. In previous 2-D work, TSI has developed an optimized equivalent source (OES) field calibration method. In this approach, calibration objects of known properties, both in air and buried in soil, are scanned. Equivalent source currents postulated on a surface surrounding the antennas (a line segment is used for aperture sources in 2-D) are then found by optimization over the calibration data. This approach has been verified for 2-D acoustic and electromagnetic data collected in the laboratory. Extension of this approach to 3-D vector field calibration is an important goal of our present research. Simulations and experimental results will be shown.

Another problem we are working on is the difficulty involved in imaging in dispersive soils. Sufficient data for the inversion of a general material frequency dependence at each image pixel is not available in reflection mode. TSI has developed an approach involving the application of the Kramers-Kronig causality constraints [5] to image frequency dispersion and thus, attenuation. Details of this approach will be discussed and preliminary results for 1-D depth profile inversion will be shown.

In order to image 3-D volumes in reasonable time using $O(\text{GFLOP})$ computers, further advances in algorithm speed and memory efficiency will be needed. TSI has recently developed a 3-D parabolic (one way wave equation) algorithm for transmission mode (single frequency) imaging of low contrast acoustic objects. The algorithm has $O(N^3 \log(N))$ complexity for one transmitter location and frequency. Simulations of the female breast have shown sufficient accuracy and speed to image $(100 \lambda)^3$ volumes. Modifications of this approach have been shown to provide accurate backscattered fields [6], and a new approach [7] uses the full Helmholtz equation and thus, removes the 1-way restriction completely. For time domain reflection mode imaging, the parabolic approach requires $O(N^4 \log(N))$ computations for the evaluation of the time waveforms for one source location. We are examining the extension of this approach to 3-D vector EM reflection mode imaging. Another algorithm option to examine is 3-D vector FDTD which has the advantage of providing the full time waveform in one $O(N^4)$ iteration. We intend to compare the speed and accuracy of these two methods. A preliminary analysis will be presented.

Algorithm and experimental research plans for this year will be outlined.

Acknowledgment/Disclaimer

This work was sponsored (in part) by the Air Force Office of Scientific Research, USAF, under grant/contract number FQ8671-95-0-0740. The views and conclusions contained herein are those of the authors and should not be interpreted as necessarily representing the official policies or endorsements, either expressed or implied, of the Air Force Office of Scientific Research or the U.S. Government.

References

1. D. T. Borup, S. A. Johnson, and M. J. Berggren, Nonperturbative Diffraction Tomography via Gauss-Newton Iteration Applied to the Scattering Integral Equation, Ultrasonic Imaging, Academic Press, 1991.
2. D. T. Borup, J. W. Wiskin, S. A. Johnson, and M. J. Berggren, An Integral Equation Method for Nonlinear Imaging of Acoustic and Elastic Parameters, Poster paper and short talk: Society of Exploration Geophysicists Research Workshop on Recording and Processing Vector Wave Field Data, 1989, Aug. 13-17, Snowbird, Utah.
3. J. W. Wiskin, S. A. Johnson, D. T. Borup, and M. J. Berggren, Non-Perturbative Modeling and Inversion of Elastic and Acoustic Inhomogeneous Structures Imbedded within a Layered Half Space, Poster paper and short talk: Society of Exploration Geophysicists Research Workshop on Recording and Processing Vector Wave Field Data, 1989, Aug. 13-17, Snowbird, Utah.
4. S. A. Johnson, M. J. Berggren, D. T. Borup, J. W. Wiskin, R. S. Eidens, and H. Leng, Comparison of Inverse Scattering and Other Tomographic Imaging Algorithms Using Simulated and Tank Data for Modeling Subbottom Imaging Systems, IEEE Oceans 1993 Symposium, 1993, vol. I: 458-492.
5. M. O'Donnell, E. T. Jaynes, and J. G. Miller, Kramers-Kronig Relationship Between Ultrasonic Attenuation and Phase Velocity, Journal of the Acoustical Society of America, 1981, vol. 69, no. 3.
6. M. D. Collins, A Two-Way Parabolic Equation for Acoustic Backscattering in the Ocean, Journal of the Acoustical Society of America, 1992, vol. 91: 1357-1368.
7. F. Natterer and F. Wübbeling, A Finite Difference Method for the Inverse Scattering Problem at Fixed Frequency, Lecture Notes in Physics, 1993, vol. 422: 157-166.

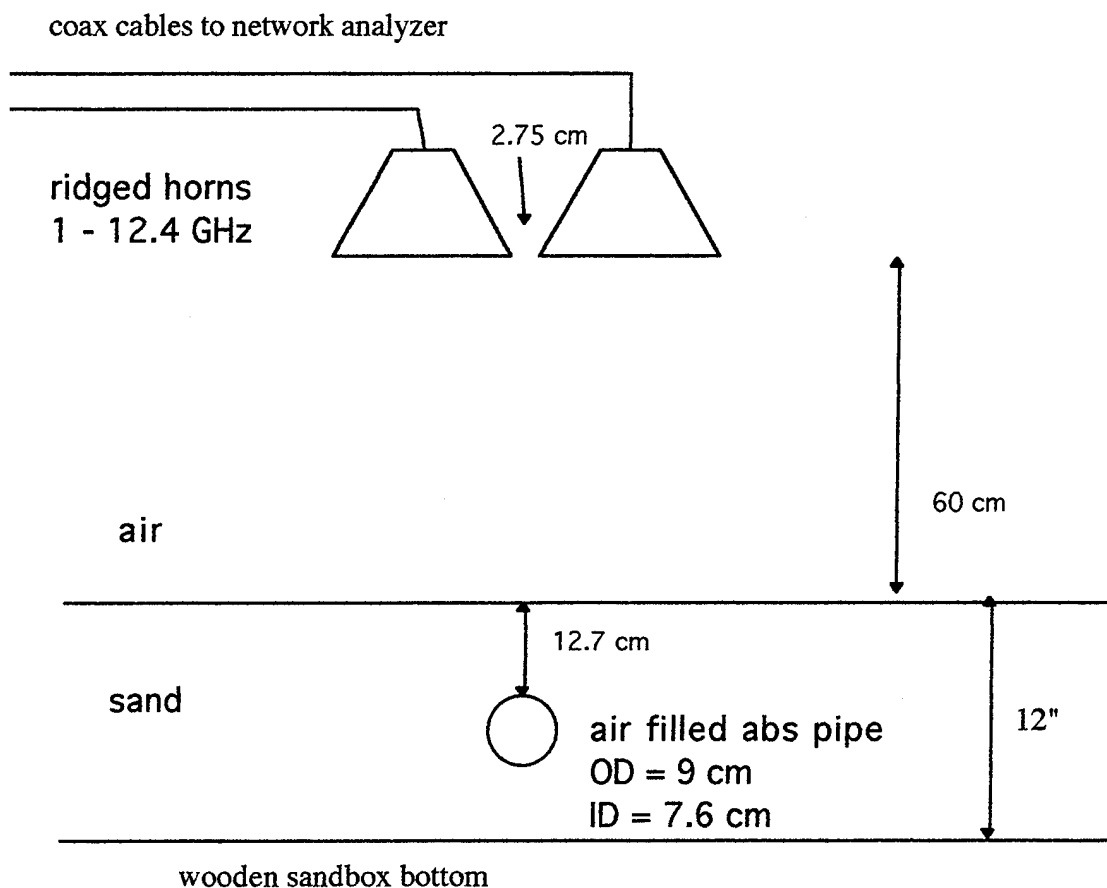


Figure 1: Experimental geometry of the laboratory scale GPR scanner. An air-filled ABS pipe buried in sand was scanned over the 1-12.4 GHz bandwidth for a single transmitter/receiver location over the pipe. This is sufficient data for inversion if an angular symmetry constraint of the target is applied. A 1/2" buried aluminum rod was used for time signal calibration. Cylindrical wave models were used for the antenna field spatial variation (in air).

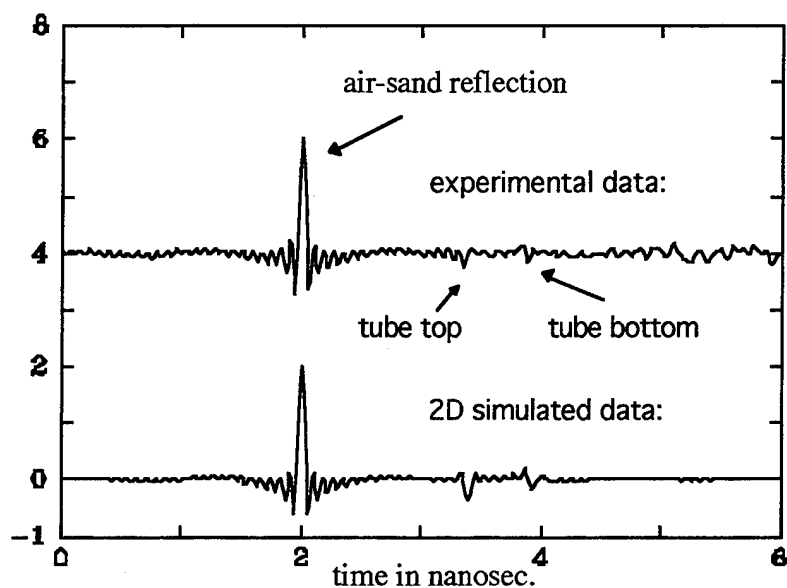


Figure 2: Comparison of the lab data with 2-D scalar theory for the experiment shown in Fig. 1. Air-sand vs. pipe amplitude ratio error in the simulated data is attributed to inadequate calibration of the antenna field spatial variation.

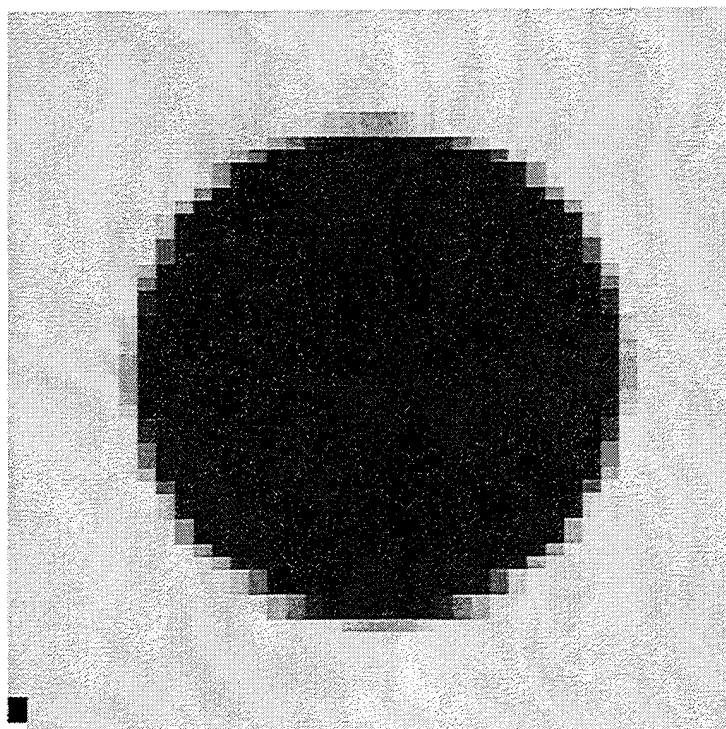


Figure 3: Grayscale of the true $\text{Re}(\gamma = \epsilon_r - 1)$ (the plastic annulus is ignored since its dielectric constant is very close to that of sand). The scale is 0.2 (white) to -0.7 (black).

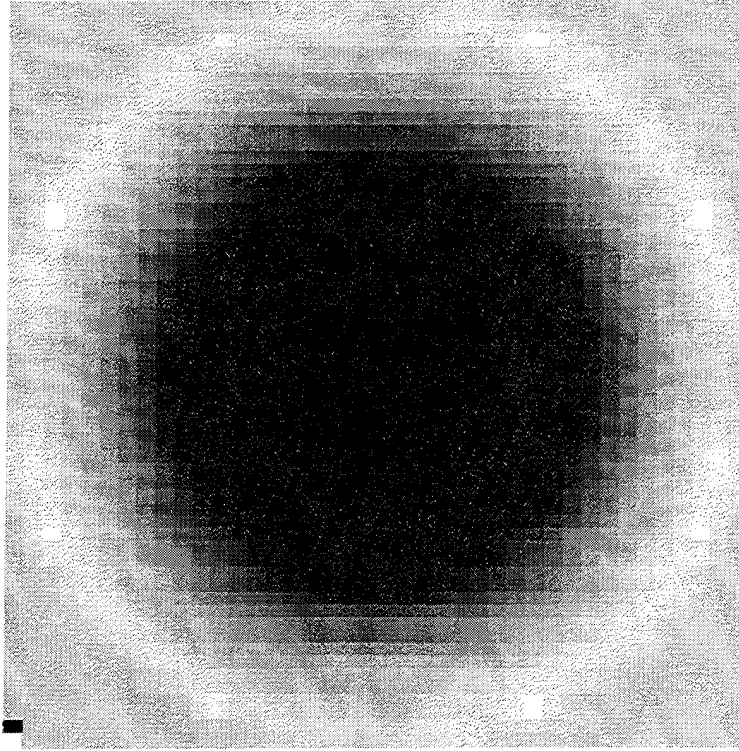


Figure 4: Inverse scattering image of the air-filled pipe from lab data.

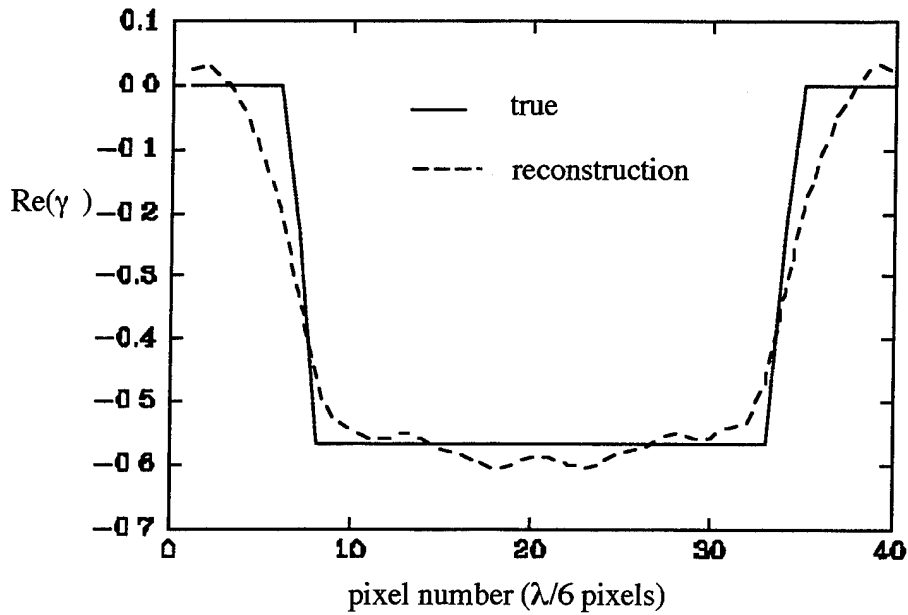


Figure 5: Centerline profile comparison of the true and reconstructed $\gamma \equiv \epsilon_r - 1$. Accuracy of the image, considering the air-sand/tube signal ratio error, is attributed to the angular symmetry constraint, coupled with the accurate arrival times. Refinement of calibration methods and multiple T/R positions should obviate the need for this constraint.

INTEGRATED GEOPHYSICAL METHODS FOR ENVIRONMENTAL SITE CHARACTERIZATION AND MONITORING

Steve Cardimona
Analytical Systems Engineering Corporation
Air Force Phillips Laboratory, Hanscom AFB, MA

Katharine Kadinsky-Cade
Earth Sciences Division, Geophysics Directorate
Air Force Phillips Laboratory, Hanscom AFB, MA

Abstract

We seek a thorough understanding of the factors that affect the recorded response of electromagnetic and seismic wave propagation in the shallow subsurface. This information will help us to evaluate the limitations of current GPR data collection and processing methods and allow us to investigate ways to improve image resolution and target recognition. A typical target of interest in this research would be a contaminant such as a DNAPL (Dense Non-Aqueous Phase Liquid).

In an effort to understand the physical contributions to ground penetrating radar (GPR) response of contaminants and shallow earth media, we are using a wave propagation modeling method developed in the frequency-wavenumber domain. Plane waves are propagated through a layered earth described by variations in dielectric permittivity, magnetic permeability and/or electrical conductivity. The ability to model GPR propagation in realistic earth media (dielectric soils with conductive losses) will help us investigate ways to improve image resolution and target recognition using GPR data. We also hope to understand the limitations of current GPR data collection methods and determine the benefits of integrating seismic (acoustic and/or elastic) data with the radar data.

Maxwell's equations of electrodynamics define a differential system that can describe the propagation of plane waves in lossy-dielectric layered media. Exact solutions are obtained for the electric and magnetic field intensities by solving an eigenvalue problem (ref. 1). The local characteristic vectors are used to match boundary conditions across interfaces between layers, and the local characteristic values are the permissible vertical wave numbers within the medium. Attenuation due to non-zero conductivity is included directly through the complex wavenumber. This is not as easily done with time-domain methods (ref. 2). Because the solutions are obtained in the frequency domain, wave dispersion effects can also be incorporated through the permittivity, permeability and conductivity functions. A fundamental matrix describes propagation through the layered medium, and the reflection and transmission response of the medium in the space-time (recording) domain is determined through an integration of the fundamental matrix (refs. 3,4). The matrix method described allows us to calculate both the reflection response (reflectivity) and the transmission response (transmissivity) of the layered medium.

When modeling monostatic (vertically incident) radar reflection profiles, we can include lateral variations in the layered earth model along the profile (a different model for each coincident source-receiver pair), and combine signals from multiple receivers into a cross-section image of the subsurface (refs. 5,6). We introduce perturbations to the background layered medium through an approximate form for the 3-D response of point scatterers (ref. 7). This result is derived from the calculation of an analytic form for the convolution involving the scattered wavefield and the full (background plus scattered) wavefield. Building up the response of (the Green's function for) the background medium one layer at

a time, the response of any point scatterer is added into each layer calculation, and thus incorporated directly into the 1-D matrix algorithm described above. We use a superposition of the scattered wavefield from a number of points acting as Huygens' sources to simulate the GPR response due to laterally varying media (fig. 1).

The GPR transmissivity calculation provides an indication of the electrical skin-depth of the layered medium. The matrix methods above allow us to study amplitude-as-a-function-of-depth for a variety of GPR source characteristics (frequencies, angles of incidence) and earth parameters (varying conductivity, dielectric constant, magnetic permeability) (figs. 2,3). Since we calculate full waveform data, we can also study the phase of the GPR signal in reflection and transmission (refs. 6,8). High contrasts in conductivity throughout the earth model affect the reflection and transmission coefficients, and this produces change in both the amplitude and the phase of the traveling waves (fig. 4).

Shallow seismic data and GPR will be collected along coincident profiles during a field experiment at a controlled spill test site at Dover AFB, Delaware. Seismic signals are sensitive to the mechanical properties of the earth, while GPR is sensitive to the subsurface electrical properties. GPR operates at higher frequencies than shallow seismic, but does not penetrate as far. Seismic surface waves may inhibit interpretation of the shallowest body wave data, however this region is well sampled by the GPR. Through analysis of field data and computer modeling, we will explore ways to integrate the two data sets.

Acknowledgment/Disclaimer

This work is sponsored by the Air Force Office of Scientific Research, USAF, under Lab Task number 94PL001. The views and conclusions contained herein are those of the authors and should not be interpreted as necessarily representing the official policies or endorsements, either expressed or implied, of the Air Force Office of Scientific Research or the U. S. Government.

References

1. B. Ursin, Review of Elastic and Electromagnetic Wave Propagation in Horizontally Layered Media, *Geophysics*, 1983, 48: 1063-1081.
2. D. Goodman, Ground-Penetrating Radar Simulation in Engineering and Archaeology, *Geophysics*, 1994, 59: 224-232.
3. F. Gilbert and G.E. Backus, Propagator matrices in elastic and vibration problems, *Geophysics*, 1966, 31: 326-332.
4. B.L.N. Kennett and N.J. Kerry, Seismic waves in a stratified half space, *Geophysical Journal of the Royal Astronomical Society*, 1979, 57: 557-583.
5. S. Cardimona, The eigenvalue problem for electrodynamics in lossy-dielectric media, *Proceedings of the Fifth International Conference on Ground Penetrating Radar*, Kitchener, Ontario, Canada, 12-16 June 1994.
6. S. Cardimona and K. Kadinsky-Cade, Modeling electromagnetic wave propagation in lossy-dielectric media, paper in preparation.
7. S. Cardimona, Modeling scatterers in layered media, submitted to *Geophysics*, 1994.
8. S. Cardimona and K. Kadinsky-Cade, Rapid Modeling of GPR Transmission Properties, *Annales Geophysicae*, 1995, 13, Supplement #1: C97.

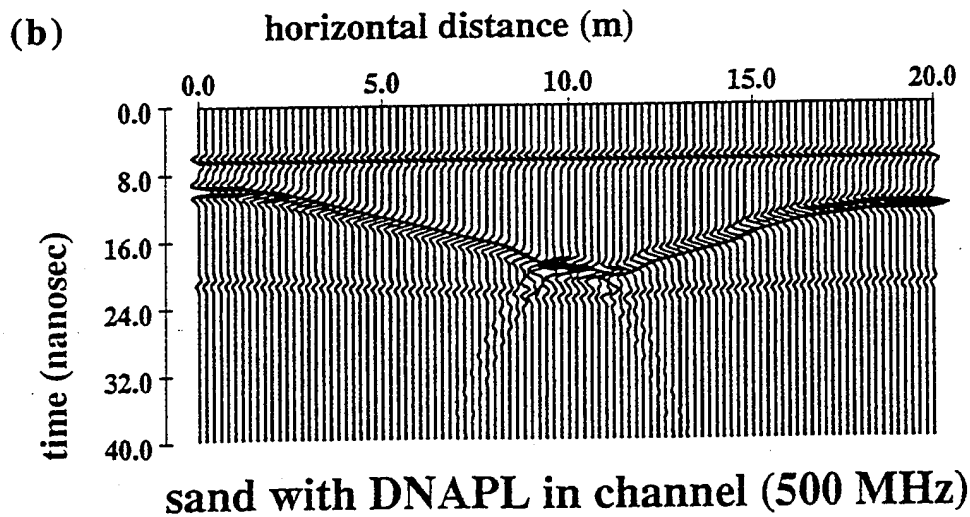
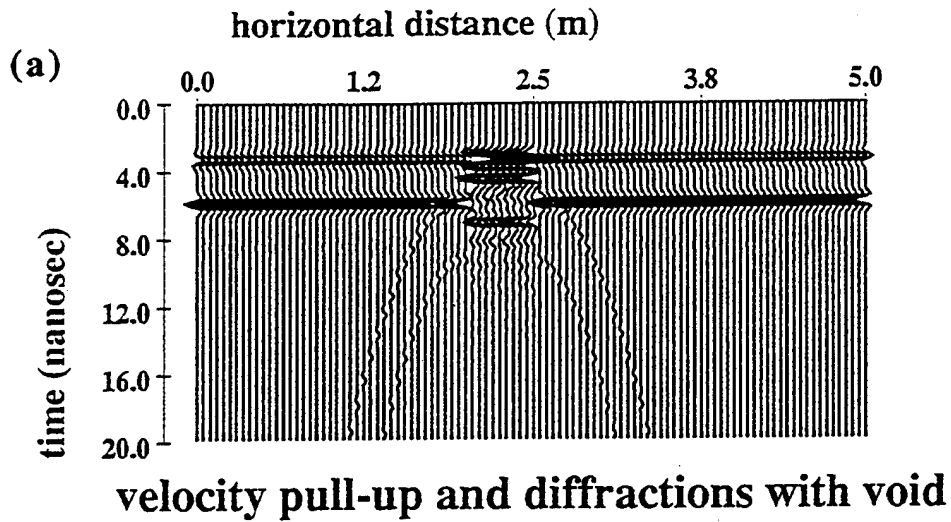
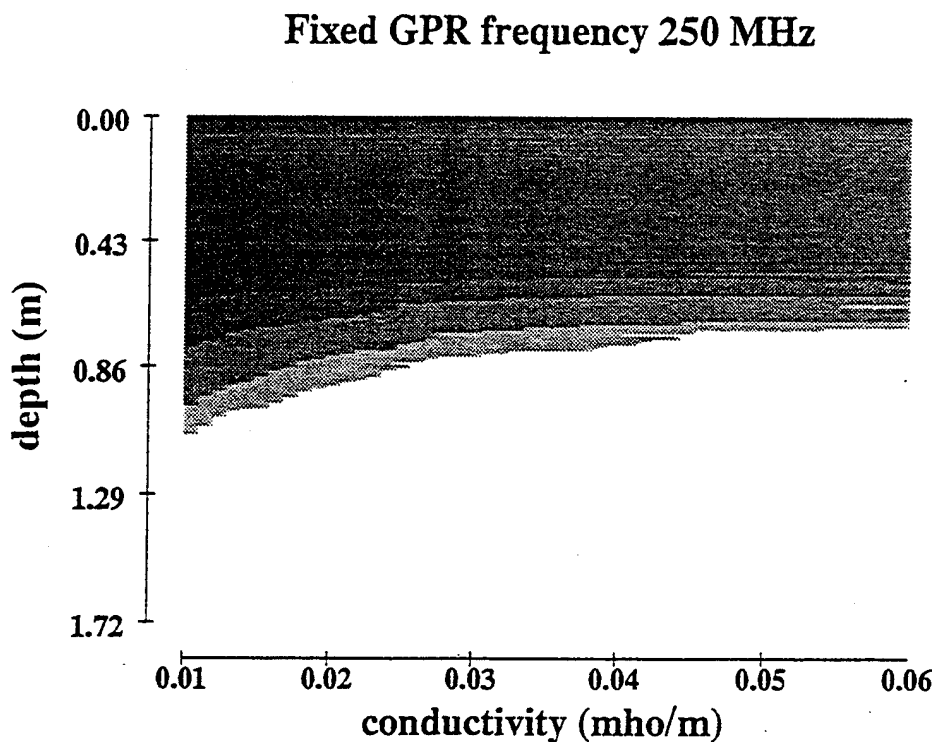


Figure 1. Monostatic GPR reflection profiles over two simple earth models. (a) GPR at 1GHz for road-bed-with-void model; (b) GPR at 500 MHz for buried-sand-channel-over-clay model with DNAPL simulated by small perturbation in the propagation constant.



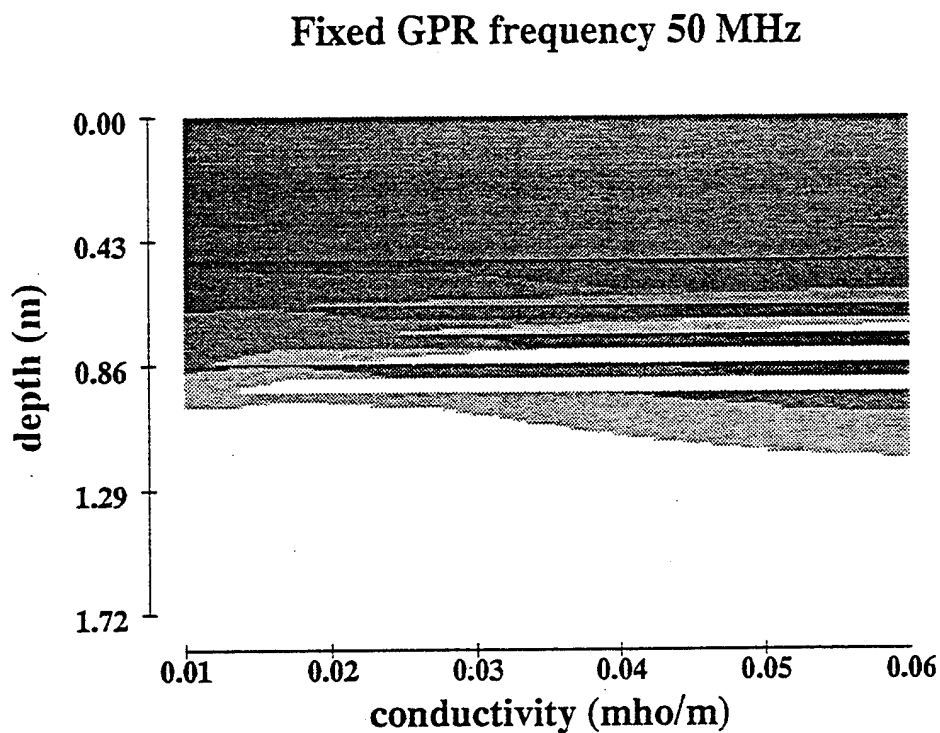
Interbedded Layer Earth Model

depth (m)	dielectric constant	conductivity (mho/m)
	10	.001
0.5	7	.01
1.0	8	.01
1.25	9	.01
halfspace	9	.01

10 layers alternating

varied from .01 - .06

Figure 2. Transmission amplitude versus depth for a layered earth model where conductivity is varied in alternating layers to simulate interbedded clays and sands. At zero depth, medium grey designates unit source amplitude for monochromatic 250 MHz wavefield. Lightening of the grey shades designates reduction of amplitude in transmission down to the depth of penetration indicated by a change to white ($1/e$ level, or skin depth).



Interbedded Layer Earth Model

depth (m)	dielectric constant	conductivity (mho/m)
	10	.001
0.5	7	.01
1.0	8	.01
1.25	9	.01
halfspace	9	.01

10 layers alternating

varied from .01 - .06

Figure 3. Transmission amplitude as a function of depth for monochromatic 50 MHz source wavefield. Earth model and grey-scale as in fig. 2.

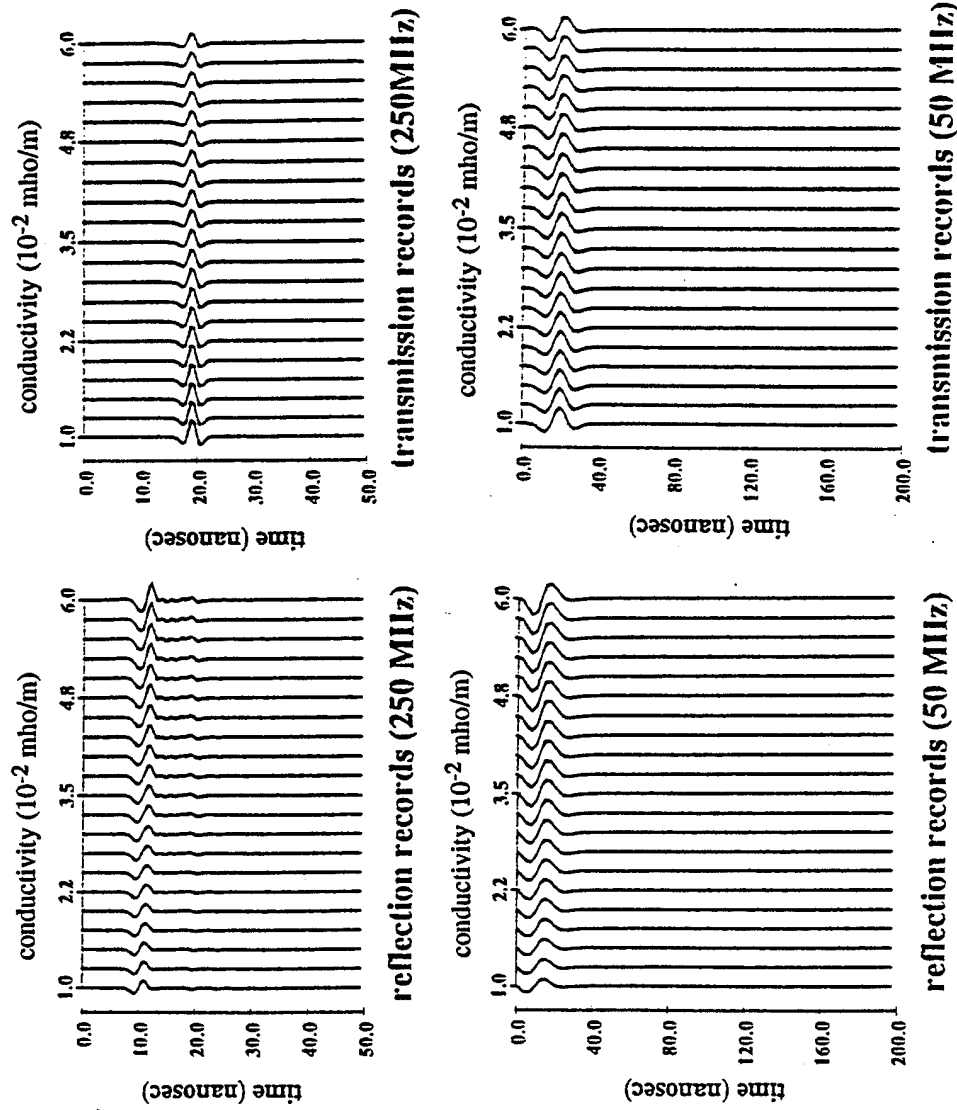


Figure 4. Reflection and transmission GPR records after varying conductivity in interbedded earth model of figures 2 and 3. Pulse radar source is a zero-phase Ricker wavelet. Amplitude and phase are sensitive to changes in conductivity through the complex permittivity.

CHARACTERIZING SCALE DEPENDENT HYDRAULIC PROPERTIES WITH MEASUREMENT OF DIELECTRIC PROPERTIES

Rosemary Knight
Department of Geophysics and Astronomy
Department of Geological Sciences
University of British Columbia, Vancouver, Canada

Abstract

Groundwater flow and contaminant transport are largely governed by the hydraulic conductivity of the subsurface. A first step in modeling groundwater flow and/or contaminant transport at a site is to obtain a 3-D model of the hydraulic conductivity of the subsurface. Past practice has often involved assigning average values of hydraulic conductivity to simple layered models of the subsurface. However it is now widely recognized that using averaged values is insufficient; the spatial variability in conductivity, the natural heterogeneity of the subsurface, has a significant effect on groundwater flow and is a critical parameter in modeling contaminant transport. There are two key issues associated with the observed variability in conductivity that are the focus of the proposed research:

- 1) the measured hydraulic conductivity of a volume of the subsurface can vary depending upon the size of the sampled volume;
- 2) at any given volume-scale the hydraulic conductivity exhibits pronounced spatial variability.

Our interest in this proposal is in addressing both of these issues from a geophysical perspective. Specifically, we plan to investigate the way in which measurements of dielectric properties, at various scales, can be used to characterize the scale-dependence and spatial variability of hydraulic properties.

Methods exist that allow for the measurement of dielectric properties, at high resolution, and across a wide range of volume-scales. Dielectric properties can be measured in the laboratory, in a borehole using logging tools, in a borehole or across a 2-D exposure using time domain reflectometry (TDR), at the surface using ground penetrating radar (GPR), and for tomographic imaging using borehole antennas. Given the wide variety of methods available for in situ dielectric measurement, and the variation in sampled volume-scale, there is tremendous potential for using dielectric properties to characterize the hydraulic properties. This can only be done successfully however if we develop a clear understanding of the link between dielectric properties and hydraulic properties, across a wide range of volume-scales. Of particular interest in this proposal is the use of ground penetrating radar as a means of obtaining a 3-D dielectric "map" of the subsurface. The central objective of the proposed research is to determine the ways in which the measured dielectric properties can then be related to unknown hydraulic properties.

Our first step has been to define a terminology for referring to the different volume scales. The following series of scales is adapted from those used in modeling fluid flow in oil reservoirs¹:

- microscopic scale: 10's to 100's of microns
- macroscopic scale: a few centimeters
- megascopic scale: 10's to 100's of meters
- gigascope scale: kilometers

The microscopic scale is the size of a few pores. At this scale there is a high degree of variability in the properties of the porous medium, and the continuum equations used to

describe flow and transport are not considered to be valid. The macroscopic scale is the size of laboratory samples and measurements, on the order of two to five centimeters. It is also generally assumed that this is the scale at which all the variability seen at the microscale is averaged, and the continuum description of transport becomes valid. Up-scaling from the macroscopic scale, we reach the megascopic scale. This scale is defined as corresponding to the size of hydrogeologic units such as sand channels, clay lenses, gravel beds. The largest scale is the gigascopic scale, which is defined as the scale of the aquifer.

Our research approach is a combination of laboratory experiments, theoretical modeling and field experiments. We divide the research problem into two regimes: those length scales (microscopic and macroscopic) at which the scale of dielectric measurement can be the same as the required conductivity structure; and the larger volume-scales (megascopic and gigascopic) at which the scale of the measured dielectric properties is much smaller than that of the hydraulic conductivity structure.

The relationship between dielectric and hydraulic properties in the first regime is addressed through a series of laboratory studies on cylindrical cells of standard dielectrics and unconsolidated materials, in which we systematically vary the material properties and scales of heterogeneity. Measurements are made of dielectric properties and hydraulic conductivity. We investigate, at the laboratory scale, the scale-dependence of each property and of the relationship between the two. These results will have implications for field sites where multi-frequency GPR can be used to obtain dielectric data across a range of scales. - Can this be transformed into a map of scale-dependent hydraulic conductivity across that same range?

In our laboratory studies we are working with a silica sand and a standard kaolinite clay. The sand is from Lane Mountain, Washington, and is essentially pure quartz. The clay is from the Clay Mineral Repository at the University of Missouri. These two end-member materials are well characterized in that we know grain densities, grain size of the sand, particle size of the clay, surface areas, and cation exchange capacity of the clay. In our previous research using these two materials we have developed a dielectric model, based on the complex refractive index model CRIM², that can accurately predict that variation of dielectric constant with porosity and clay content. We start by defining the properties of each solid component in its "wetted" state; i.e. we determine the dielectric constant of the solid in equilibrium with a few monolayers of adsorbed water³. Once these input parameters are known, we find that our measured data can be well modeled using the simple volumetric mixing law, CRIM:

$$\sqrt{K_T} = \sum_i f_i \sqrt{K_i}$$

where K_T is the dielectric constant of the total measured system and f_i and K_i are the volume fraction and dielectric constant of the i th component.

From our experiments with the sand/clay mixtures we have obtained initial results that indicate a direct link between dielectric constant and permeability. These results are shown in Figure 1 as a plot of measured dielectric constant versus permeability for a suite of sand/clay mixtures. The dielectric constant was measured on the sand/clay mixtures at a frequency of 1 MHz using an impedance analyzer. Permeability was measured on different sand/clay mixtures, but with the same composition, using a falling head permeameter. There is very good agreement between our predicted relationship and that observed with our data. The predicted relationship is derived using CRIM as a model for dielectric properties and the Kozeny-Carmen equation as a model for permeability.

The results in Figure 1 are for a very simple, homogeneous mixture of sand and clay. Due to the constraints of the measurement techniques, the measurements of dielectric constant and permeability were made on different samples, with different sizes. Our present extension of this research is to conduct experiments on heterogeneous materials, and to assess the effect of sample size. We have recently obtained a time domain reflectometry probe which can be used with the same samples on which the permeability measurements are made. The only result to date with the new TDR probe is a measurement of the dielectric constant of water; not a new result! but evidence that we now have a working and accurate probe. We are presently designing the samples cells for the joint permeability/dielectric measurements.

The second regime of scale in our research is that at which large-scale hydrogeologic structures are assumed to dominate the flow. This is the scale at which the architecture of the aquifer needs to be characterized in terms of features such as sand channels, gravel bars, clay lenses. The proposed methodology for aquifer characterization at this scale involves determining the sedimentological environment from outcrop and core and then generating a sedimentological facies model of the subsurface⁴. Values of hydraulic conductivity can be assigned to the various sedimentary units, thus creating a hydrogeologic facies model. This approach has great potential to provide realistic models of hydraulic conductivity variation, as it is based on years of research by sedimentologists who have studied in detail the spacial variation in material properties within different sedimentary units. A limitation to this method is the need to adequately characterize the sedimentary environment in order to generate the facies model. This is essentially impossible to do in areas of limited outcrop and core data.

At this megascopic scale, there is enormous potential for using GPR to image the size, shape, distribution and internal structure of the megascopic hydrogeologic units. In Figure 2 is shown a GPR profile from an area east of Vancouver, British Columbia where we are attempting to image these larger-scale units. As shown in the interpreted section there is evidence that we are able to detect cross-stratified gravel units, clay layers, and channels. The use of GPR for identifying such larger-scale units, may prove to be an extremely useful way of obtaining a quantitative description of the mega-scale heterogeneities controlling flow in an aquifer. In order to do this successfully however, there need to be integrated field studies that allow us to determine the electromagnetic signature of various types of sedimentary units; i.e. when an electromagnetic wave interacts with a sand channel in a stratified sand/gravel background - what is the resulting appearance of that feature in the GPR record in terms of the velocity structure, and the amplitude and continuity of reflectors?

The key to successful imaging and thus characterization of this type with GPR, is the development of a fundamental understanding of which hydrogeologic features are "seen" with GPR and why. A series of cliff face experiments has been started in which we image features visible in the face and then sample in detail the imaged interface to determine the dominant parameters responsible for the successful imaging. Equally important will be the detailed study of those features that cannot be imaged with GPR. We conducted our first such study last summer, with GPR surveys conducted along the top of the cliff and samples taken for measurement of porosity, grain size and moisture content. This summer we will add the use of TDR to measure in situ dielectric constants. We are proposing to conduct several of these experiments, imaging specific features to determine which can be detected with GPR. An obvious extension of these experiments is the use of forward modeling to attempt to simulate the recorded GPR data.

Having completed the proposed experiments that span scales from centimeters to 10's of meters, we will be in a position to attempt to develop a conceptual framework for the scale-dependent relationship between dielectric and hydraulic properties. At this point in this project it appears that the two defined regimes will necessarily correspond to two separate regimes for theoretical modeling of the dielectric and hydraulic behavior. There is however the intriguing possibility that we will discover a means of scaling the physics, so that we can cross the boundary from macro-scopic to mega-scopic in a way that integrates a knowledge of geological processes to predict the relationship between resulting properties.

In conclusion, the objective of our laboratory, theoretical and field study is to investigate the relationship between dielectric properties and hydraulic properties across a wide range of volume-scales. Our approach will advance the understanding of the scale-dependence of these properties, and more importantly, the scale-dependence of the relationship between these two properties. Ultimately this will allow us to more effectively use remote measurement of dielectric properties as a means of characterizing the spacial variability in hydraulic properties.

Acknowledgment/Disclaimer

This work was sponsored in part by the Air Force Office of Scientific Research, USAF, under grant number F49620-95-1-0166. The views and conclusions contained herein are those of the authors and should not be interpreted as necessarily representing the official policies or endorsement, either expressed or implied, of the Air Force Office of Scientific Research or the U.S. Government.

References

1. Haldorsen, H.H. and Lake, L.W., 1984, A New Approach to Shale Management in Field-Scale Models, *Journal of the Society of Petroleum Engineers*, 447-457.
2. R. P. Wharton, G. A. Hazen, R. N. Rau, and D. L. Best, 1980, Electromagnetic Propagation Logging: Advances in Technique and Interpretation, *Society of Petroleum Engineers*, Paper 9267.
3. R. J. Knight and A. L. Endres, 1990, A New Concept in Modeling the Dielectric Response of Sandstones: Defining a Wetted Rock and Bulk Water System, *Geophysics*, 55, 586-594.
4. M. P. Anderson, 1989, Hydrogeologic Facies Models to Delineate Large-Scale Spacial Trends in Glacial and Fluvio-Glacial Sediments, *Bulletin of the Geological Society of America*, 101, 501-511.

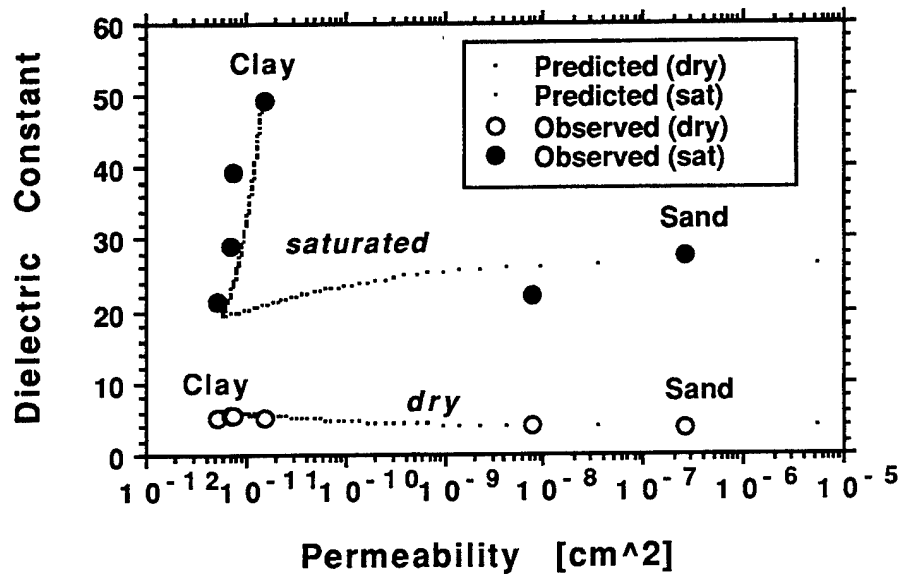


Figure 1: Modeled relationship between the dielectric constant of sand-clay mixtures and permeability for both saturated and dry materials. The measured data points (observed) show good agreement with the model (predicted). The model combines a complex refractive index model of the dielectric behavior with permeability predictions from the Kozeny-Carmen relationship.

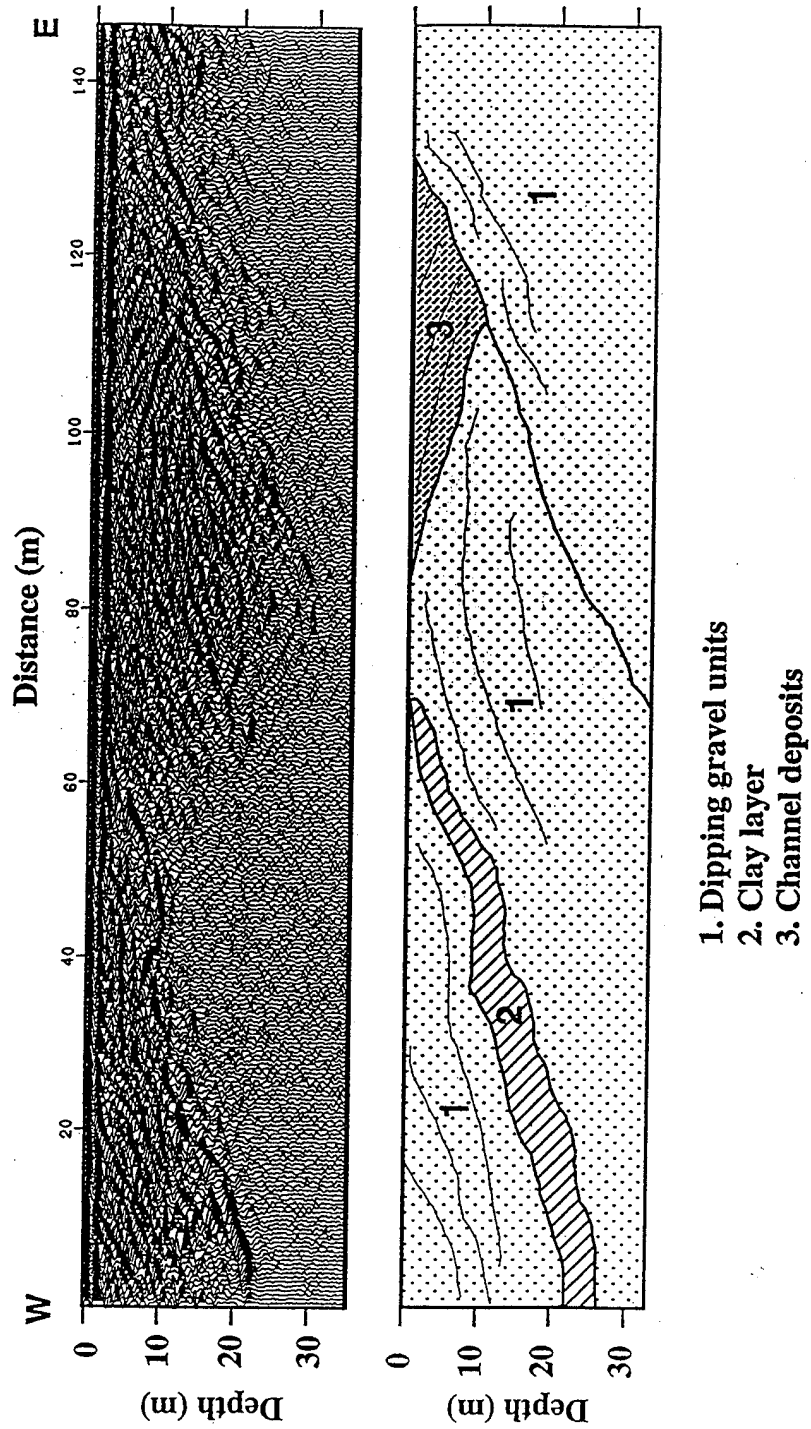


Figure 2: Example of GPR data collected with 100 MHz antennas. Note the imaging of large-scale hydrogeologic features as interpreted in the lower section.

NONINVASIVE COMPLEX RESISTIVITY MEASUREMENTS OF CLAY-ORGANIC PROCESSES TO MAP ORGANIC CONTAMINATION AND DEGRADATION OF CLAY BARRIERS

Gary R. Olhoeft*
Department of Geophysics
Colorado School of Mines

Introduction and Background

One of the most difficult problems in environmental remediation is location of subsurface organic contaminants [2, 18, 31, 32]. Most common organic contaminants [8, 20, 22] are known to react with clay minerals [13, Table 16, and references therein]. However, while many clay-organic reaction processes are known, only a few have been the subject of detailed studies, and mostly for agricultural purposes [5, 7, 13, 21, 29]. Worse yet, some of these reactions alter the physical properties of the clays, allowing contaminant migration through supposedly impermeable clay barriers [4, 6, 10, 11, 12, 34, and earlier references reviewed in 13, p. 516-525).

Although the induced polarization (IP) process was observed by Conrad Schlumberger as early as 1912, it was not until the 1950's that mining companies used the induced polarization (or complex resistivity) method to detect economic minerals (see reviews in 3, 28)). Complex resistivity does this by detecting the electrochemical processes that occur between minerals and water (such as oxidation-reduction corrosion of sulfides, see review in [15, 17]). Petroleum companies have exploited IP effects caused by hydrocarbon seepage that results in iron sulfide geochemical alteration halos [26]. More recently, complex resistivity has been exploited to observe cation exchange at clay-water surfaces and to directly measure the reactions between organics and clay minerals (see reviews in [15, 18]).

In 1984, the U. S. Environmental Protection Agency Environmental Monitoring Systems Laboratory and the U. S. Geological Survey Water Resources Division were investigating organic contamination problems in Nevada and Louisiana, and requested geophysical assistance. At that time, the detection of organics with geophysics was not at all understood nor expected. Core samples of representative uncontaminated and organic-contaminated materials from the sites were measured and a large IP difference was observed in the laboratory between the uncontaminated and contaminated materials [16]. Although the cause of the IP response was not known nor understood, it was large enough to be exploited in the noninvasive mapping of organics in the subsurface [16]. It also showed that at the Nevada site, reaction of the organic with a impermeable clay

* 1500 Illinois St., Golden, CO 80401-1887, (303) 273-3458, -3478 fax,
golhoeft@mines.colorado.edu; formerly with the U. S. Geological Survey, Denver, CO

barrier supporting a perched water table had caused the contaminants to penetrate through more than a meter of 100% montmorillonite clay [16]. The clay layer was of the swelling type that would squeeze a drill hole shut in a few days, so the penetration by the organics was a surprise. Unfortunately at the Nevada site, the contaminant plume was formed from many disparate sources and a large variety of organic chemicals, which have reacted amongst themselves to create new, not-before-known organics, and it has not been possible to determine which ones are specifically causing the clay-organic response.

The Louisiana site was a much simpler mix of contaminants resulting from the disposal of oil field brines and hydrocarbons in a landfill [16]. To understand and better exploit the field observations, a systematic laboratory investigation was begun to identify the organics reacting with the clays [23] and to identify the mechanisms and reaction processes. Toluene was identified as the reactive organic at the Louisiana site, allowing duplication of the field observations and core studies with synthetic mixtures of toluene and montmorillonite [23] using clay mineral standards [33]. Further laboratory investigations [9, 19] found the reaction mechanism to be the polymerization of toluene to bibenzyl in the Lewis Acid surface environment of montmorillonite clay. Identifying and understanding the mechanism of the clay-organic (montmorillonite-toluene) reaction (polymerization to bibenzyl) allowed calibrating the geophysical field measurements and turning anomaly mapping into quantitative toluene concentration mapping (Olhoeft, in press).

In addition to mapping organic contamination by their reactions with clays, complex resistivity should also be able to monitor changes in the properties of the clays caused by reaction with the organics. As mentioned and referenced above, such processes can have adverse impact on contaminant migration by causing the breach of otherwise impermeable clay barriers. Thus, complex resistivity could be a useful monitoring tool to periodically test the integrity of landfill clay mineral liners or natural clay mineral impermeable barriers.

Finally, the complex resistivity monitoring of clay-organic processes could also be useful in monitoring unanticipated and undesirable changes during a site remediation. In particular, it should be an excellent tool to monitor remediation using electrokinetic effects [1, 24, 25].

Research Effort

Synthetic mixtures of clay minerals and selected organic contaminants will be measured in the laboratory to determine which combinations produce observable complex resistivity responses as a function of frequency. Those with observable responses will be further tested as a function of clay mineral type, water chemistry and organic concentration to determine the limits of the complex resistivity response. Those with useful response limits will be investigated to determine the mechanisms and processes of clay-organic interaction using standard geochemical laboratory procedures.

The details of this investigation will have to evolve as the investigation proceeds as it is basic research into the unknown. In the beginning, mixtures of single components of most common organic contaminants [13] will be mixed with standard and well characterized clay minerals [33] and the complex resistivity response will be measured. Cross-discipline expertise in Geophysics, Geology, Chemistry and Geochemistry, Petroleum Engineering and in Environmental Sciences will be required to follow whatever path the clay-organic investigation requires. In the case of the montmorillonite-toluene reaction [19], diffuse infrared reflectance spectroscopy proved the most useful tool in unravelling the process. In other cases, different tools may prove more useful and a comprehensive suite of investigatory techniques is required and available through interdisciplinary cooperation.

Natural soil samples from the Air Force testbed at Dover, Maryland will also be run through the laboratory investigations to determine the possible clay-organic interactions at the site for the organic contaminants to be tested at that site. If the site materials show promising complex resistivity response, noninvasive field complex resistivity measurements will be performed to map the geochemical reactive heterogeneity of the site and provide a baseline for future testing.

Acknowledgment/Disclaimer

This work was originally funded (1984-1994) by the U. S. Environmental Protection Agency Environmental Monitoring Systems Laboratory (Las Vegas, NV) and the U. S. Geological Survey Water Resources Division Toxic Substances Hydrology Program. Beginning June 1, 1995, it will be funded (in part) by the Air Force Office of Scientific Research. The views and conclusions contained herein are those of the author and should not be interpreted as necessarily representing the official policies or endorsements, either expressed or implied, of the Air Force Office of Scientific Research or the U. S. Government.

References

1. Acar, Y. B. and Alshawabkeh, A. N., Principles of electrokinetic remediation: Environ. Sci. Tech., 1993, v. 27, pp. 2638-2647.
2. Chem-Nuclear Geotech, Inc., Technology needs assessment final report: U.S. Department of Energy Report DOE/ID/12584-92, var. pag., 1992.
3. Collett, L. S., History of the induced polarization method: in Induced polarization, applications and case histories, J. B. Fink, B. K. Sternberg, E. O. McAlister and W. G. Wieduwilt, eds., Tulsa, Soc. Explor. Geophys., p. 5-21, 1990.
4. Crisanto, T., Sanchez-Martin, M.J., Sanchez-Camazano, M., and Arienzo, M., Mobility of pesticides in soils. Influence of soil properties and pesticide structure: Toxicol. Environ. Chem., 1994, v. 45, pp. 97-104.
5. Dragun, J., The soil chemistry of hazardous materials: Silver Spring, MD, HMCRI, 458p., 1988.

6. Gerstl, Z., Galin, T., and Yaron, B., Mass flow of a volatile organic liquid mixture in soils: *J. Environ. Qual.* , 1994, v.23, pp. 487-493.
7. Goring, C. A. I. and Hamaker, J. W., eds., *Organic chemicals in the soil environment*: NY, NY, Marcel Dekker, 968p. , 1972.
8. Hallstedt, P. A., Puskar, M. A., and Levine, S. P., Application of the hazard ranking system to the prioritization of organic compounds identified at hazardous waste remedial action sites: *Hazardous Waste and Hazardous Materials*, 1986, v. 3, p. 221-232.
9. King, T.V.V., and Olhoeft, G.R., Mapping organic contamination by detection of clay-organic processes, in *Proc. Petroleum Hydrocarbons and Organic Chemicals in Ground Water: Prevention, Detection and Restoration Conference*, Nov. 15-17, 1989, Houston, AGWSE/NWWA/API, Dublin, OH, NWWA, p. 627-640, 1989.
10. Kowalska, M., Gueler, H., and Cocke, D.L., Interactions of clay minerals with organic pollutants: *Sci. Total Environ.* , 1994, v. 141, pp. 223-240.
11. Li, Y. and Gupta, G., Adsorption of hydrocarbons by clay minerals from gasoline: *J. Haz. Mat.* , 1994, v. 38, pp. 105-112.
12. Li, Y. and Gupta, G., Adsorption/desorption of hydrocarbons on clay minerals: *Chemosphere*, 1994, v. 28, pp. 627-638.
13. Lucius, J. E., Olhoeft, G. R., Hill, P. L., and Duke, S. K., Properties and hazards of 108 selected substances - 1992 edition: U.S. Geological Survey Open-File Report 92-527, 554 p. , 1992.
14. Meegoda, N. J., and Rajapakse, R. A., Short-term and long-term permeabilities of contaminated clays: *J. Environ. Eng.* , 1993, v. 119, pp. 725-745.
15. Olhoeft, G. R., Low frequency electrical properties: *Geophysics*, 1985, v. 50, p. 2492-2503.
16. Olhoeft, G. R., Direct detection of hydrocarbon and organic chemicals with ground penetrating radar and complex resistivity, in *Proc. of the NWWA/API Conference on Petroleum Hydrocarbons and organic chemicals in ground water -- prevention, detection and restoration*, Nov., 12-14, 1986, Houston: Dublin, OH, NWWA, p. 284-305, 1986.
17. Olhoeft, G. R., Monitoring geochemical processes with geophysics, *Proceedings of a U.S. Geological Survey Workshop on Environmental Geochemistry*, Doe, B.R., ed.: U.S. Geological Survey Circular 1033, p. 57-60, 1990.
18. Olhoeft, G. R., Geophysical detection of hydrocarbon and organic chemical contamination: in Bell, R.S., ed, *Proceedings on Application of Geophysics to Engineering, and Environmental Problems*, Oakbrook, IL: Society of Engineering and Mining Exploration Geophysics, Golden, CO, p. 587-595, 1992.
19. Olhoeft, G. R., and King, T. V. V., Mapping subsurface organic compounds noninvasively by their reactions with clays: in U.S. Geological Survey Toxic Substance Hydrology Program, *Proceedings of the technical meeting*, Monterey, California, March 11-15, 1991, USGS WRI 91-4034, p. 552-557, 1991.
20. Plumb, R. H., Jr. and Pitchford, A. M., Volatile organic scans -- implications for ground water monitoring: in *Proc. of the API and NWWA Conf. on Petroleum*

- Hydrocarbons and Organic Chemicals in Ground Water -- Prevention, Detection and Restoration, Houston, TX, November 13-15, 1985, p. 207-222, 1985.
21. Rausell-Colom, J. A. and Serratosa, J. M., Reactions of clays with organic substances: in Chemistry of clays and clay minerals, A. C. D. Newman, ed., NY, Wiley, p.371-422, 1987.
 22. Riley, R. G., Zachara, J. M. and Wobber, F. J., Jr., Chemical contaminants on DOE lands and selection of contaminant mixtures for subsurface science research: U. S. Dept. of Energy Report DOE/ER-0547T, 77p. , 1992.
 23. Sadowski, R. M., Clay-organic interactions: MSc thesis T-3551, Dept of Geochemistry, Colorado School of Mines, Golden, 209p. , 1988.
 24. Segall, B. A. and Bruell, C. J., Electroosmotic contaminant-removal processes: J. Environ. Eng. , 1992, v. 118, pp. 84-100.
 25. Shapiro, A. P. and Probstein, E. F., Removal of contaminants from saturated clay by electroosmosis: Environ. Sci. Tech. , 1993, v. 27, pp. 283-291.
 26. Sternberg, B. K. and Oehler, D. Z., Induced-polarization hydrocarbon surveys: Arkoma Basin case histories: in Induced polarization, applications and case histories, J. B. Fink, B. K. Sternberg, E. O. McAlister and W. G. Wieduwilt, eds., Tulsa, Soc. Explor. Geophys., p. 354-378, 1990.
 27. Stolpe, N. B., McCallister, D. L., Shea, P. J., Lewis, D. T., and Dam, R., Mobility of aniline, benzoic acid, and toluene in four soils and correlation with soil properties: Environ. Pollut. , 1993, v. 81, pp. 287-295.
 28. Sumner, J. S., Principles of induced polarization for geophysical prospecting: NY, Elsevier, 277p. , 1976.
 29. Theng, B. K. G., The chemistry of clay-organic reactions: NY, NY, Wiley, 343p., 1974.
 30. Uppot, J. O. and Stephenson, R.W., Permeability of clays under organic permeants: J. Geotech. Eng. , 1989, v. 115, p. 115-.
 31. USDOE (U.S. Dept. of Energy), Basic research for environmental restoration, U. S. Department of Energy Report DOE/ER-0482T, 156 p. , 1990.
 32. USEPA (U.S. Environmental Protection Agency), Dense nonaqueous phase liquids - a workshop summary, Dallas, TX, April 16-18, 1991, U.S. Environmental Protection Agency Report EPA/600/R-92/030, 82p. , 1992.
 33. van Olphen, H. and Fripiat, J. J., Data handbook for clay minerals and other non-metallic minerals: NY, Pergamon, 346p. , 1979.
 34. Zytner, R. G., Sorption of benzene, toluene, ethylbenzene and xylenes to various media: J. Haz. Mat., v. 38, pp. 113-126, 1994.

UNDERGROUND IMAGING IN HIGH CONTRAST CASES

George Papanicolaou

Department of Mathematics

Stanford University

Stanford CA 94305

Internet: papanico@math.stanford.edu

Abstract

Imaging methods are based mostly on small variation representations of the unknown parameters of the medium (the Born representation). This is done extensively in cross-hole electromagnetic imaging of the earth (D. L. Alumbaugh, Berkeley Thesis 1993) and in impedance tomography in general. In travelttime tomography Berryman (Inverse Problems, **6**, 21-42, 1990) introduced constrained reconstruction algorithms based on Fermat's variational principle that work even with high-contrast media. This idea extends to impedance tomography whenever variational principles are available as in the static or very low frequency cases.

In this lecture I will discuss the use of variational principles to analyze direct and inverse problems with high contrast in the low frequency or quasistatic regime which is most useful for underground imaging. I will present extensive numerical results that show how high-contrast difficulties can be approached and sometimes overcome.

This is joint work with J. Berryman and L. Borcea.

Acknowledgement/Disclaimer

This work is sponsored by the Air Force Office of Scientific Research under Grant F49620-94-1-0436. The views and conclusions contained herein are those of the authors and should not be interpreted as necessarily representing the official policies or endorsements, either expressed or implied, of the Air Force Office of Scientific Research or the US Government.

MODELING AND INVERSION OF SHALLOW SEISMIC DATA INCLUDING NONGEOMETRICAL WAVES

John Scales and Ilya Tsvankin
Center for Wave Phenomena
Colorado School of Mines, Golden

Abstract

Our research is focused on advanced seismic inversion and imaging methods based on a more comprehensive treatment of wave propagation than the classical ray theory. A major component of the project is investigation of the so-called "nongeometrical" waves in realistic models of the subsurface (the term "nongeometrical" refers to waves that cannot be accounted for by the geometrical-seismics approximation conventionally used in seismology). Nongeometrical waves can supply information about some parameters of the medium that are poorly constrained by conventional waves, such as the elastic properties of waveguides. The information contained in full waveforms makes it possible to devise enhanced methods of imaging of complicated geologic structures and different types of inhomogeneities.

To take full advantage of this comprehensive treatment of seismic wavefields, we are developing inversion methods capable of producing subsurface images with higher accuracy and resolution than conventional algorithms.

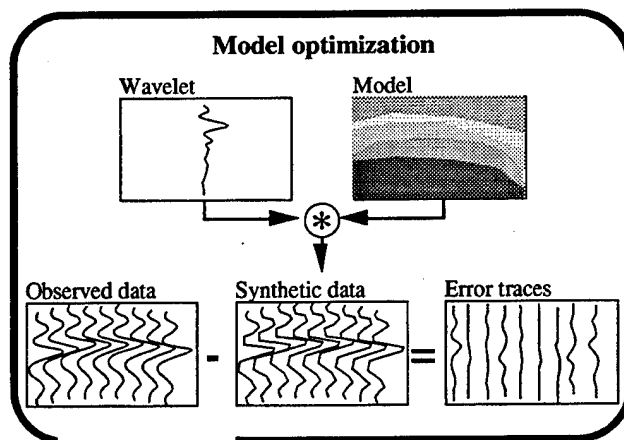


FIG. 1.

We have adopted a multi-faceted approach to full-waveform inversion including: (1) investigation of novel objective functions which reduce the extreme non-convexity of full-waveform inverse problems; (2) a new statistical approach to incorporation of realistic prior

information; (3) effective combination of global optimization methods with rapid, gradient-descent algorithms. We have begun developing an extensive modeling capability (based on finite-difference methods) on the massively parallel Connection Machine (CM-5). We are also working on a library of nonlinear local and global optimization routines, including a variety of Monte Carlo methods, nonlinearly constrained downhill simplex, as well as other direct search methods.

The advantages of our approach should be especially significant in shallow surveys, which are strongly affected by near-field phenomena and, consequently, nongeometrical waves. The level of resolution to be achieved with our new technologies will depend on the probing wavelength and the scattering/attenuative properties of the subsurface. While it is difficult to give a quantitative estimate of the resolution before the work is complete, we expect a significant improvement over conventional methods because our algorithms will treat the whole wavefield (including nongeometrical, refracted waves etc.) rather than just the first arrivals and make no smoothing assumptions about the medium. We expect that our methods will be helpful in different aspects of site characterization and monitoring, such as subsurface contaminant location, groundwater studies, and other environmental problems.

Our project is currently at its initial stage. In the near future we will be working on full-waveform modeling and inversion of cross-hole seismic data with the goal of obtaining high-resolution seismic images. In addition to synthetic models, we will apply our algorithms to a multicomponent cross-hole data set recorded by Conoco at its Newkirk, Oklahoma, test site. This site is characterized by a vertically stratified geology showing large velocity contrasts. This combination results in complicated raypaths, guided wave phenomena, and possible generation of nongeometrical waves. Figure 2 is a sample three-component, common-receiver gather showing significant energy in late arrivals. The horizontal components contain intensive low-frequency guided waves marked by B. It is likely that other nongeometrical waves contribute to the wavefield between the first arrivals and guided modes (A in Figure 2). Obviously, these are only preliminary observations which should be supported by a more detailed investigation.

Although we are not planning on studying other geophysical techniques within the framework of the project, the inversion methods we are working on will be generally applicable in a wide variety of imaging technologies. For instance, our inversion algorithms can be used to enhance radar detection methods by properly modifying the objective functions.

Acknowledgment/Disclaimer

This work was sponsored (in part) by the Army Research Office under grant/contract number DAAH04-95-1-0173. The views and conclusions contained herein are those of the authors and should not be interpreted as necessarily representing the official policies or endorsements, either expressed or implied, of the Army Research Office or the U.S. Government.

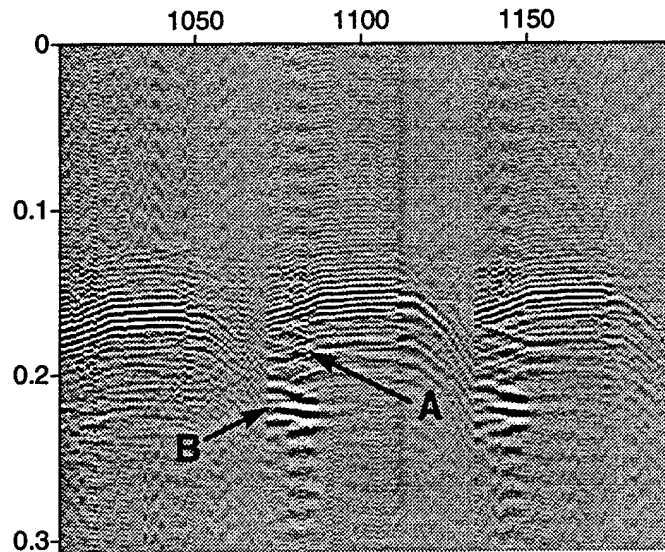


FIG. 2. Three-component common-receiver gathers for a single source polarization. The left column is the vertical displacement component, the next two columns represent horizontal components. A and B are explained in the text. Data courtesy of Conoco.

References

- A. Devaney, Geophysical diffraction tomography, *IEEE Trans. Geosc. Rem. Sens.*, 1984, GE 22: 3-13.
- S. Gray and L. Lines, Cross-borehole tomographic migration, *Seismic Exploration*, 1992, 4: 315-324.
- F. Hron and B.G. Mikhailenko, Numerical modeling of nongeometrical effects by the Alekseev-Mikhailenko method, *Bull. Seismol. Soc. Am.*, 1981, 71: 1011-1029.
- J.Y. Kim and J. Behrens, Experimental evidence of S*-wave, *Geophys. Prosp.*, 1986, 34: 100-108.
- L. Lines, K. Kelly, and J. Queen, Channel waves in cross-borehole data, *Geophysics*, 1992, 57: 334-342.
- J. Scales, P.C. Docherty, and A. Gersztenkorn, Regularization of nonlinear inverse problems—Imaging the near-surface weathering layer, *Inverse Problems*, 1990, 6: 115-131.
- J. Scales, M.L. Smith, and T.L. Fischer, Global optimization methods for multimodal inverse problems, *Journal of Computational Physics*, 1992, 102: 258-268.
- I. Tsvankin, Determination of shear-wave velocities using nongeometrical waves, 61 SEG Annual Meeting, Expanded Abstracts, 1991: 1587-1590.
- R. Wu and N. Toksöz, Diffraction tomography and multisource holography applied to seismic imaging, *Geophysics*, 1987, 52: 11-25.

BASIC RESEARCH ON THREE-DIMENSIONAL (3D) ELECTROMAGNETIC (EM) METHODS FOR IMAGING THE FLOW OF ORGANIC FLUIDS IN THE SUBSURFACE

Dr. Ben K. Sternberg
Department of Mining and Geological Engineering
University of Arizona

Dr. Steven L. Dvorak
Department of Electrical and Computer Engineering
University of Arizona

Introduction

High-frequency (100 MHz to 1 GHz) ground-penetrating radar methods have shown excellent resolving capabilities at very shallow depths. The depth of penetration of radar energy, however, varies widely depending on the soil electrical properties, and is generally too shallow for many environmental site characterization surveys. A promising technique for imaging shallow buried targets is electromagnetic induction. In order to have reasonable penetration into the subsurface, we must use relatively low frequencies, e.g., a few kHz to a few tens of MHz. The equation that applies to electromagnetic induction, over most of the frequency range of interest, is actually the diffusion equation, rather than the wave equation. Objects are detected in the subsurface via secondary fields induced in the buried objects rather than propagating energy being reflected off the objects.

A number of commercial electromagnetic instruments are currently used for shallow subsurface electromagnetic induction surveys. These systems are effective for determining depths to layers (for example, depth to water table or depth to bedrock) and for detection of buried targets. They have had limited success for imaging of buried targets in the subsurface.

The LASI High-Resolution EM Systems

The University of Arizona, Laboratory for Advanced Subsurface Imaging (LASI) has developed research electromagnetic (EM) sounding systems that provide a significant advance in the state-of-the-art for shallow subsurface imaging (Sternberg et al., 1991; Sternberg and Poulton, 1994). These systems record the ellipticity of the received magnetic field signal. The received magnetic field from a remote transmitter traces an ellipse as a function of time. The ellipticity is defined as the ratio of the minor axis of the ellipse to the major axis. Ellipticity is a particularly sensitive parameter for mapping depths to buried layers in the subsurface (Hoversten, 1981).

Figure 1 shows a photograph of the LASI high-resolution EM transmitter. The electronics are mounted on a 6-wheel drive all terrain vehicle (ATV). The transmitting coil is mounted on a boom extended in front of the ATV. Figure 2 shows a photograph of the receiver ATV. The receiver coil is mounted on the boom at the rear of the ATV. This EM system measures ellipticity over frequency ranges of 1 kHz to 1 MHz or 32 kHz to 32 MHz. An earlier version

of this system recorded over a frequency range of 30 Hz to 30 kHz. These systems incorporate a number of unique features, including: (1) high-accuracy simultaneous calibration, (2) automated data acquisition, (3) high signal/noise ratio, and (4) rapid surveying with very dense measurements. The LASI systems represent a significant advance in the state-of-the-art for shallow EM sounding.

These EM sounding systems form the foundation for the new methods that are being developed on this project.

Testing and Demonstration

Initial testing and demonstration of the imaging techniques developed in this project will be carried out at a physical modeling facility that we recently built at our Avra Valley Test Site. The upper end of the frequency range in the EM imaging systems will include effects from both conduction currents and displacement currents. It is difficult to obtain reliable numerical modeling calculations of theoretical responses to complex targets in this frequency range. We will therefore use full-size physical models.

The modeling tank is located at our test site in Avra Valley, Arizona, west of the University of Arizona campus. The tank is 20 m long by 3 m deep by 6 m wide (see Figure 3). The transmitter-receiver array will be kept stationary in order to avoid variations in response due to background effects. Various targets will be moved in the tank along a profile line under the array. Repeated measurements will be made with the targets at different depths, orientations, and with different types of targets. The background conductivity and dielectric constant of the fluid in the tank will be varied by using mixtures of different fluids. Only non-hazardous fluids will be used. This physical modeling facility provides a unique capability for testing and demonstration of the new EM imaging techniques.

Final testing of the EM imaging techniques developed in this project will be carried out at a lined basin which is also located at our Avra Valley Test Site. The basin was designed to test the ability of the high-resolution EM system to image the flow of fluid in the subsurface. It is approximately 5 m deep, and 30 m x 30 m square. Heavy-duty high-density polyethylene (HDPE) plastic was used to line the bottom and sides of the excavated basin. Gravel was then placed in the bottom of the basin along with drain pipes. Figure 4 shows a photograph of the liner and the completed pit after the gravel layer had been placed in the bottom and before soil had been filled in. The lined basin provides a closed system for injection experiments. It is a unique facility for monitoring the flow of fluids which provides minimal interference from the bottom and sides of the pit.

EM Sounding with the LASI Systems

Figures 5 and 6 show examples of EM soundings with the LASI high-resolution EM Sounding system (Sternberg, 1993). This example used the lined basin shown in Figure 4.

During the summer of 1992, 24,170 liters of fluid were injected along a 1 m x 25 m strip through the middle of the lined basin. High-resolution subsurface-imaging ellipticity surveys were made over the injection region prior to and during the injection. Figure 5 shows an

image of the electrical resistivity of the ground immediately after the injection started. Figure 6 shows the electrical resistivity of the ground 17 days after the start of the injection. These images produced by the EM system agree very well with cross-sections of ground resistivity as determined by well-log measurements that were made in 25 boreholes which span the injection region. The EM imaging system was very successful in imaging the location of the fluid during the entire course of the injection. Note, however, that this fluid plume is relatively large and extended effectively infinite in and out of the section.

Current Research

Ellipticity measurements contain information about the average properties of the earth between the transmitter and receiver. Thus, ellipticity is best suited for measuring the properties of a layered earth. Tests have shown ellipticity measurements to be relatively insensitive to small three-dimensional targets. In order to detect relatively small 3D targets, we have redirected our current research toward improving the imaging capabilities of these EM systems. Specifically, we are studying arrays of magnetic field sensors, including: (1) null-coupling arrays for greater sensitivity, (2) focusing arrays for greater resolution, (3) three-dimensional arrays for improved target identification, and (4) large, dense arrays for faster, lower-cost acquisition.

The initial results with prototype arrays are very encouraging. Greatly improved sensitivity and resolution appear to be obtainable. Some fundamental problems remain, including: (1) reducing the capacitive coupling between the transmitter and receiver, and (2) determining optimum array sizes and configurations.

Acknowledgment/Disclaimer

This work was sponsored (in part) by the Air Force Office of Scientific Research, USAF, under grant/contract number F49620-95-1-0004. The views and conclusions contained herein are those of the authors and should not be interpreted as necessarily representing the official policies or endorsements, either expressed or implied, of the Air Force Office of Scientific Research or the U.S. Government.

References

1. G. M. Hoversten, Comparison of Time and Frequency Domain EM Sounding Techniques, Ph.D. Thesis, University of California, Berkeley, 1981.
2. B. K. Sternberg, S. J. Thomas, N. H. Bak and M. M. Poulton, High-Resolution Electromagnetic Imaging of Subsurface Contaminant Plumes, EPRI EN-7519, 1991.
3. B. K. Sternberg, Construction of a Lined Basin for Tests of a High-Resolution Subsurface Imaging Ellipticity System, EPRI TR-103462, 1993.
4. B. K. Sternberg and M. M. Poulton, High-Resolution Subsurface Imaging and Neural Network Recognition, Proc. SAGEEP '94, Boston, 1994, pp. 847-855.

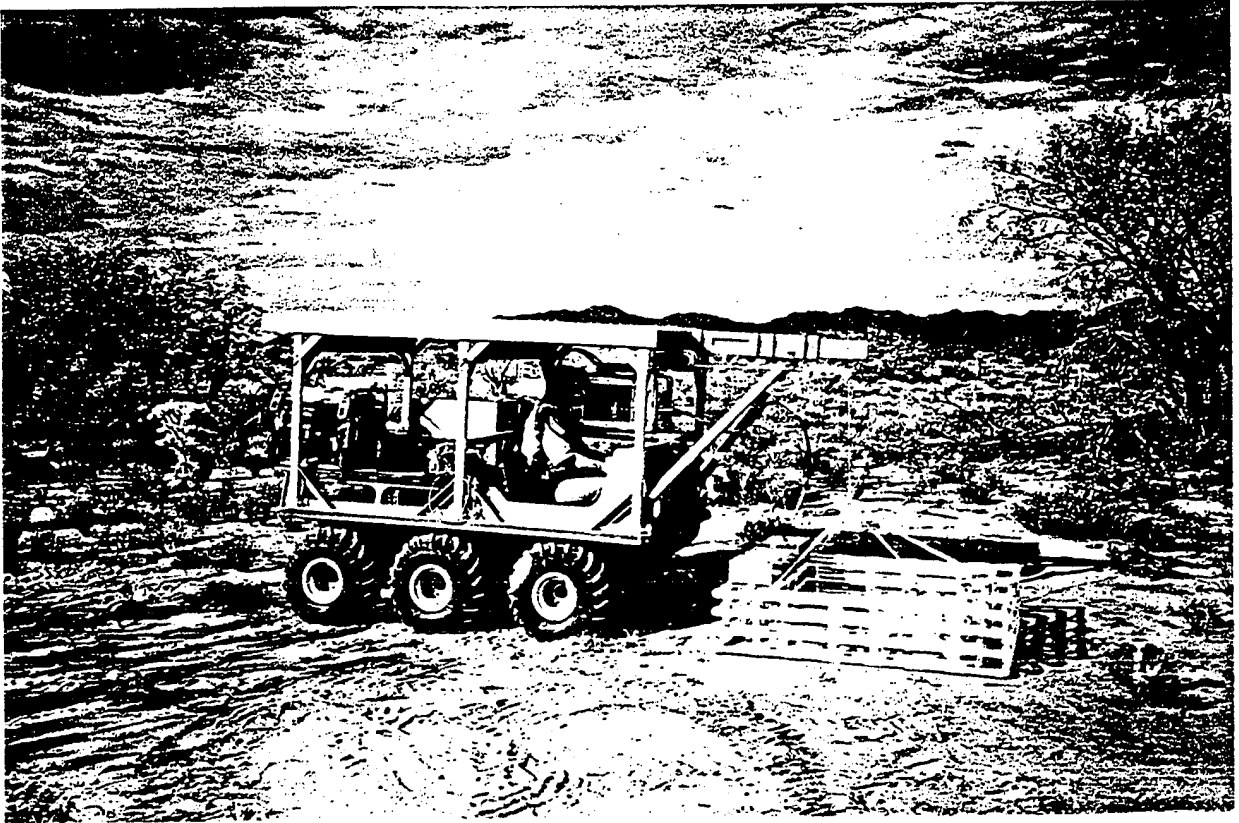


Figure 1. LASI high-resolution EM system -- transmitter ATV.

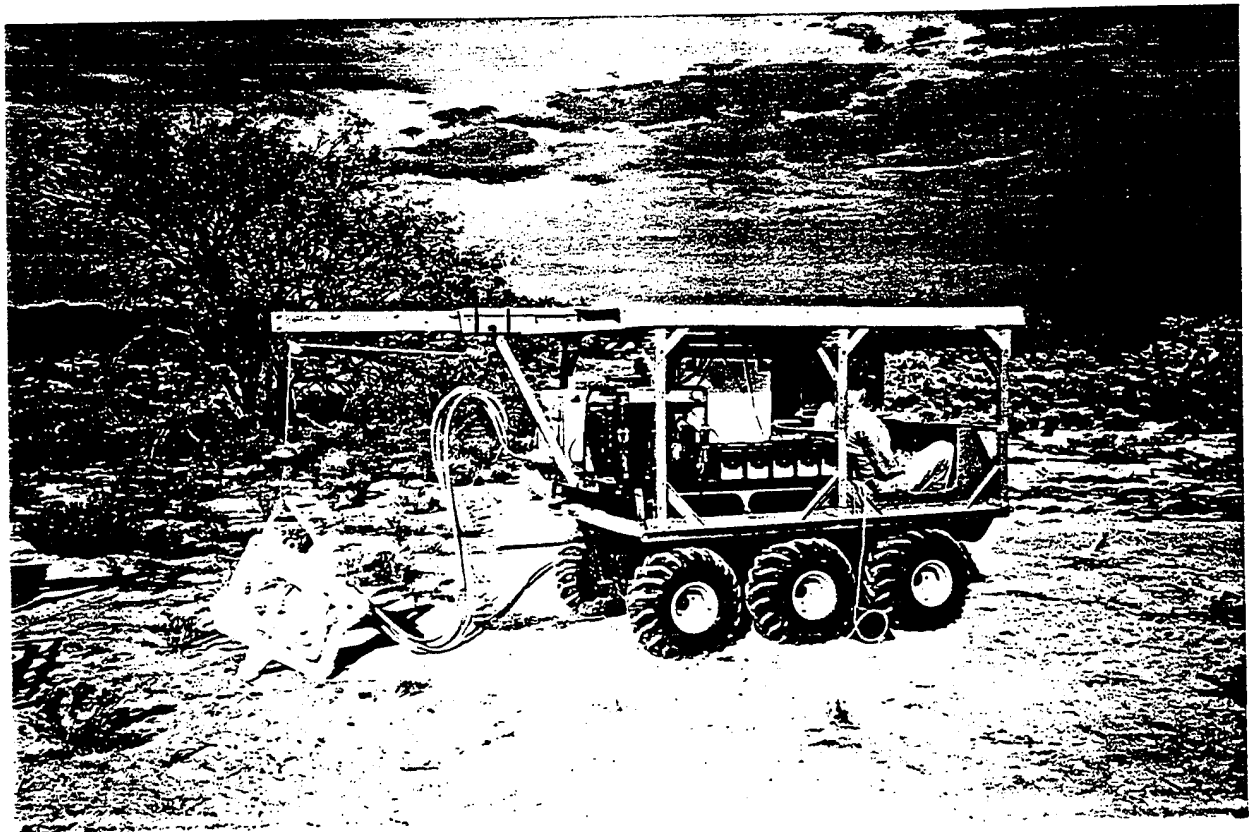


Figure 2. LASI high-resolution EM system -- receiver ATV.

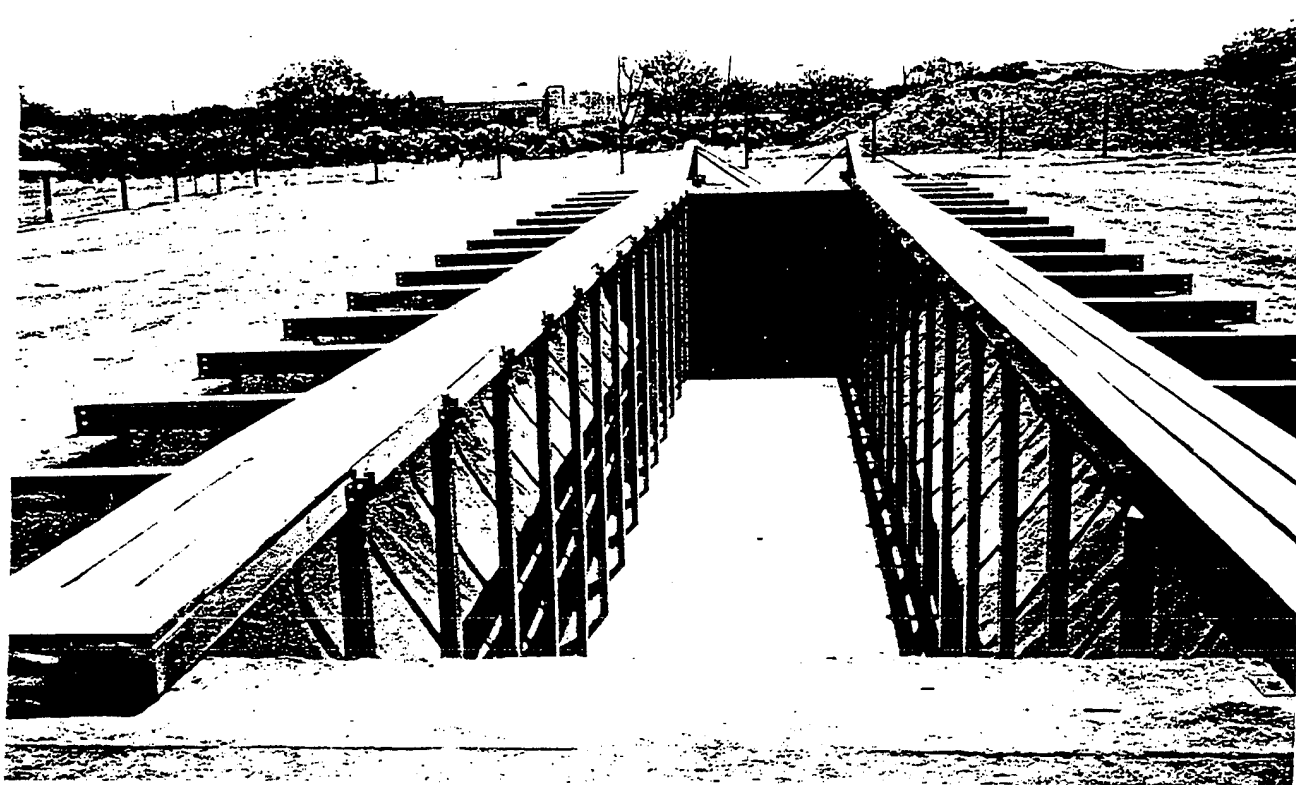


Figure 3. Physical modeling facility.

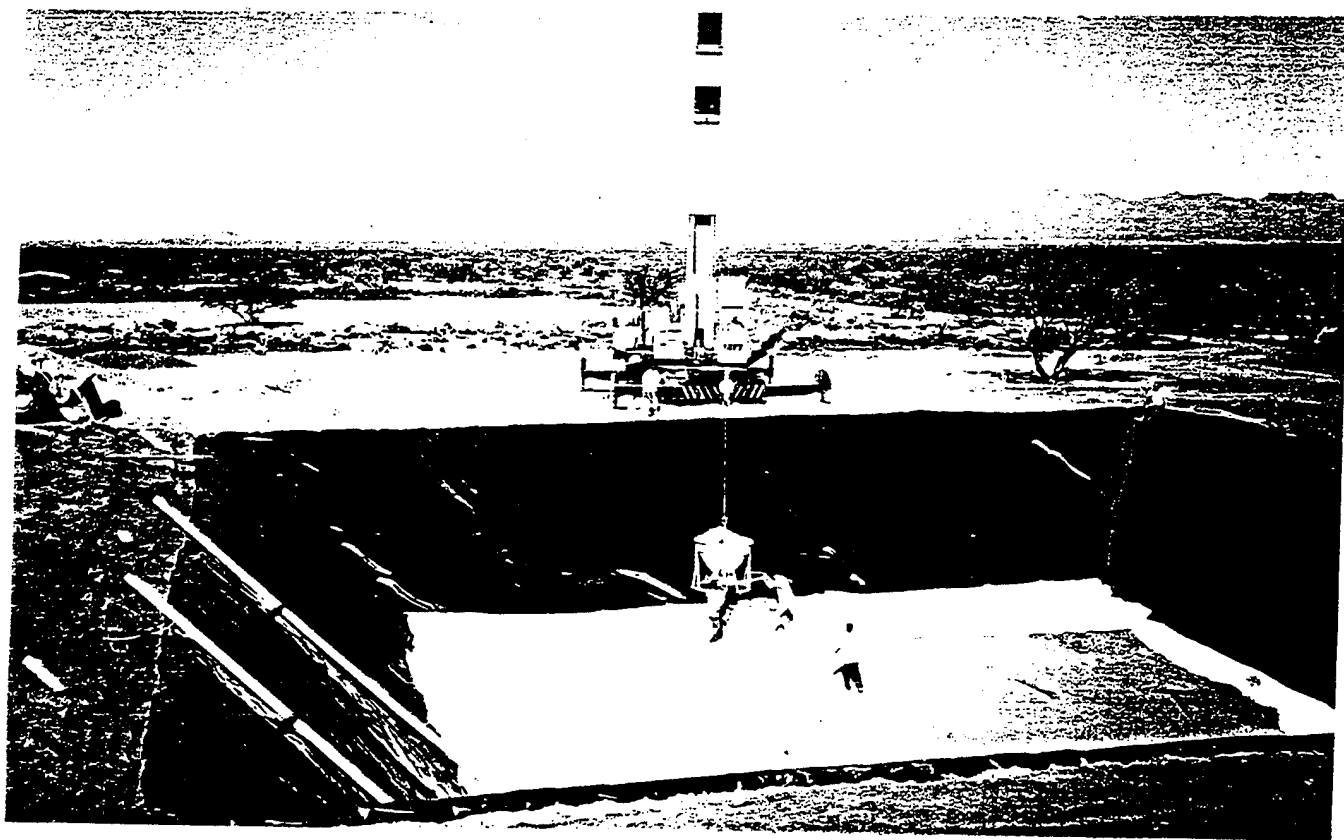


Figure 4. Lined-basin fluid injection test site during construction

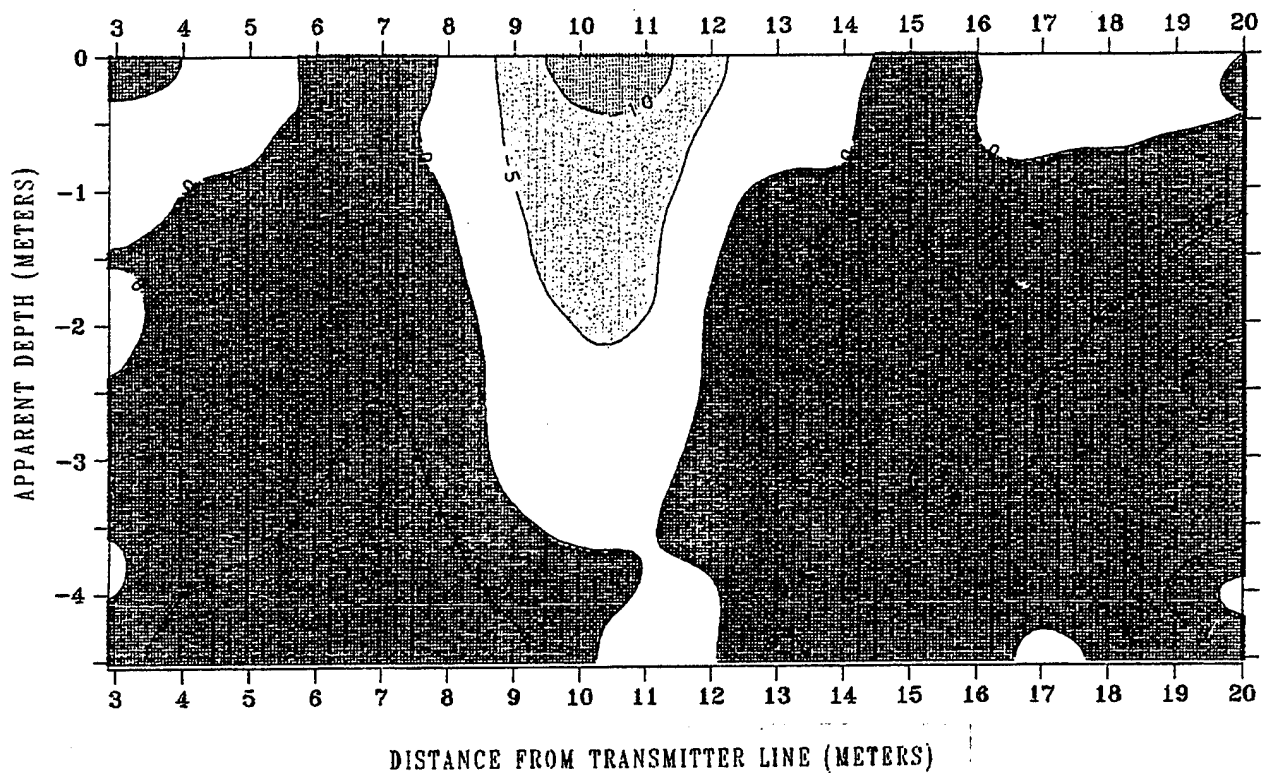


Figure 5. Apparent resistivity image one day after the start of injection.

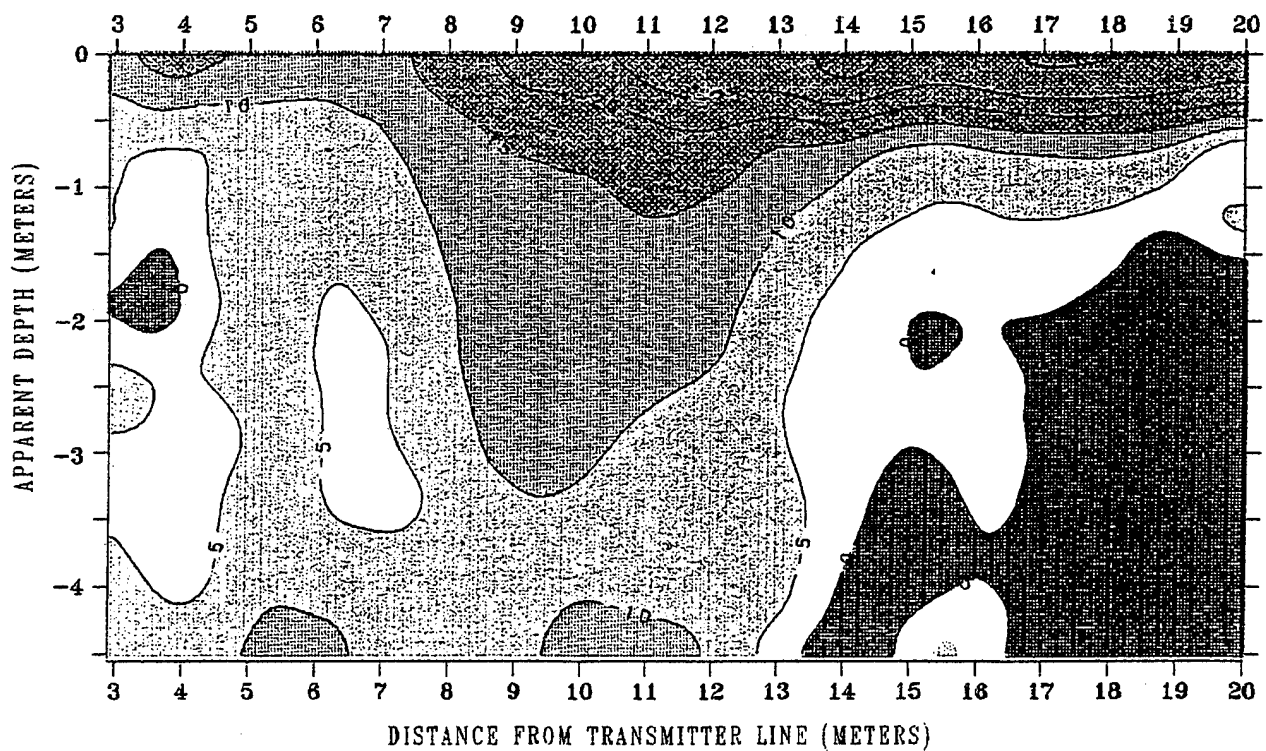


Figure 6. Apparent resistivity image 17 days after the start of injection.

A PDE BASED APPROACH TO DISPERSIVE INVERSE PROBLEMS

Yun Wang
Mathematical Products Division
Armstrong Laboratory, OES
Brooks AFB, TX 78235

Abstract

A time domain approach for study of electromagnetic inverse problems is presented in this note. Maxwell equations coupled with a generalized dispersion model, an electric polarization equation governed by an n -th order differential equation are considered. Well posedness is presented for a one-dimensional dispersive medium case. Parameters representing the electromagnetic property of a medium are the static permittivity, relaxation time, natural frequency, static conductivity, etc.. The number of parameters involved depend on the choice of order of derivatives in the polarization equation.

In environmental, clinical medicine and many other areas, the microwave images of tissue structures and soils play very important roles. The microwave images are useful in detection/remediation of underground toxic wastes, and detection/enhanced treatment of abnormality of human organs and tissue. The electromagnetic properties of a medium are characterized by its electric polarization mechanisms and its static conductivity. In this note we focus on the development of partial differential equations (Maxwell equations) based identification techniques for physical and biological distributed parameter systems, with those for living tissue being a special case. We attempt to estimate the conductivity and parameters which characterize the polarization of living tissue based on the incident and scattered electromagnetic signals. We point out that in literature the complex permittivity and conductivity which depend on frequency of the emitting signal are commonly used as electromagnetic properties. The functions of complex permittivity and conductivity are determined by a polarization mechanism which is assumed to be governed by an n -th order ordinary differential equation (see [11, 16] for the case $n = 2$). Since our approach is in the time domain, we focus directly on the polarization equations.

The electromagnetic inverse problem has been studied for at least two decades. A good survey of existing methods is given by Albanese et al. in [1]. However, there is very little literature on the study of electromagnetic inverse problems in the time domain employing variational formulations. The variational formulation approach has been successfully applied to damped hyperbolic systems in [5, 6, 7] and hybrid systems in [4]. A similar approach applied to Maxwell equations can be found with focus on well posedness and control problems. For example, Duvaut and Lions [9] proved existence and uniqueness of Maxwell equations for a three-dimensional inhomogeneous medium with superconductive boundary. The medium is stable (nonzero static conductivity) and polarization is assumed to be proportional to the electric field. Other

efforts focused on controllability and stabilization in the context of semigroups and variational formulations can be found in [3, 12, 13, 14, 15].

We consider different dispersion models (i.e. models for polarization) in the context of Maxwell equations in a theoretical study of the type and rate of attenuation of signals associated with a given dispersion model for living tissue.

For a three-dimensional inhomogeneous medium, the equation governing electromagnetic phenomena are Maxwell equations

$$\begin{aligned}\nabla \cdot \mathbf{D} &= 0 \\ \nabla \cdot \mathbf{B} &= 0 \\ \nabla \times \mathbf{E} &= -\frac{\partial \mathbf{B}}{\partial t} \\ \nabla \times \mathbf{H} &= \frac{\partial \mathbf{D}}{\partial t} + \mathbf{J}_i + \mathbf{J}_c\end{aligned}\tag{1}$$

and constitutive relations

$$\mathbf{J}_c = \sigma \mathbf{E} \tag{2}$$

$$\mathbf{D} = \epsilon_0 \mathbf{E} + \mathbf{P} \tag{3}$$

$$\mathbf{B} = \mu_0 \mathbf{H} + \mathbf{M}, \tag{4}$$

where \mathbf{E} is the electric field intensity, \mathbf{D} is the electric flux density, \mathbf{H} is the magnetic field intensity, \mathbf{B} is the magnetic flux intensity, \mathbf{J}_i is the source electric current density, \mathbf{P} is the electric polarization, \mathbf{M} is the magnetic polarization, σ is the position dependent static conductivity, ϵ_0 and μ_0 are the permittivity and permeability in vacuum respectively. The bold faced characters are vectors in Cartesian coordinates.

In preliminary research, the propagation of a plane wave is investigated. Assuming the plane wave is to be uniform in planes parallel to the x - y plane and propagates in z direction, then the electric and magnetic field intensity are reduced to

$$\begin{aligned}\mathbf{E} &= E(t, z) && \text{in } x \text{ direction} \\ \mathbf{H} &= H(t, z) && \text{in } y \text{ direction.}\end{aligned}$$

The scalar fields E and H will be adopted from now on with understanding the E is polarized in x direction and H is polarized in y direction. Furthermore, we assume that magnetic polarization is zero, i.e., $M(t, z) = 0$ which is a good approximation to human tissue [2]. With the above assumptions, Maxwell equations coupled with the constitutive relations yield a second order equation

$$\mu_0 \epsilon_0 \frac{\partial^2 E}{\partial t^2} + \mu_0 \epsilon_0 \frac{\partial E}{\partial t} + \mu_0 \frac{\partial^2 P}{\partial t^2} - \frac{\partial^2 E}{\partial z^2} = -\mu_0 \frac{\partial J_s}{\partial t}, \quad t > 0, \quad 0 \leq z \leq 1. \tag{5}$$

While tissue is thought to have magnetic properties of vacuum, dispersion of electromagnetic signals in heterogeneous media is a complex phenomenon which is usually accounted for in the polarization vector P . In the case of dispersive media (here, we adopt the definition by Stratton [16] which states that a medium is said to be dispersive if the phase velocity in the medium is a function of frequency), we consider a general representation for the electric polarization described by n -th order ordinary differential equation

$$\frac{\partial^n P}{\partial t^n} + \sum_{i=1}^n a_i \frac{\partial^{n-i} P}{\partial t^{n-i}} = a_0 E, \quad (6)$$

where the coefficients $\{a_i\}_{i=1}^n$ are constants. This representation of polarization takes into account the molecular constitution of matter and treats the molecules as dynamical systems possessing natural frequency. For the case of $n = 0, 1, 2$ the polarization mechanisms have been studied extensively [11, 16]. When $n = 0$, the nonzero constant a_0 is identified as the product of electric susceptibility χ_E and ϵ_0 , hence the electric flux density (3) becomes

$$D = (1 + \chi_E) \epsilon_0 E = \epsilon E,$$

in which ϵ is called the static permittivity of the medium. Many media (such as metals) exhibit this property.

When $n = 1$, we can identify (6) with the Debye model (which is considered to the polarization mechanism of water [1])

$$\frac{\partial P}{\partial t} + a_1 P = a_0 E$$

which is commonly expressed as

$$\frac{\partial P}{\partial t} + \frac{1}{\tau} P = \frac{\epsilon_s - \epsilon_\infty}{\tau} E$$

where ϵ_s is the static relative permittivity and ϵ_∞ is the limiting permittivity in the field subject to increasingly high frequencies, and τ is the relaxation time.

In case $n = 2$, we obtain the Lorentz model

$$\frac{\partial^2 P}{\partial t^2} + a_1 \frac{\partial P}{\partial t} + a_2 P = a_0 E$$

or with the physical parameters

$$\frac{\partial^2 P}{\partial t^2} + \omega_0^2 \frac{\partial P}{\partial t} + \frac{1}{\tau} P = \omega_p^2 E$$

where ω_0 is the natural frequency and ω_p is a constant related to the charge of the medium oscillator. In this model, media are treated as a fine-grained assembly of molecular oscillators. Such a treatment has gained substantial support due to our knowledge of molecular and atomic structure [11].

We study a general n -th order ODE polarization equation since there is still a substantial lack of understanding related to the inability to explain the electromagnetic wave propagation phenomena in some media by employing one of the three dispersion models mentioned above.

Next, we define a one-dimensional inhomogeneous dispersive slab occupying $[z_1, z_2]$ such that $0 < z_1 < z_2 < 1$ as our example geometry. The medium outside the slab is filled with air in which $\epsilon_0, \mu_0, \sigma = 0$. We assume absorbing boundary conditions; that is,

$$\begin{aligned}\frac{\partial E}{\partial t}(t, 0) - c \frac{\partial E}{\partial z}(t, 0) &= 0, \\ \frac{\partial E}{\partial t}(t, 1) + c \frac{\partial E}{\partial z}(t, 1) &= 0,\end{aligned}\tag{7}$$

where c is the speed of light in vacuum.

It will be shown that under certain conditions the system (5) and (6) coupled with boundary conditions (7) is well posed in a properly defined space in the context of a variational formulation.

The identification of electric polarization mechanisms is formulated as parameter estimation problems. For given incident (pulse modulated microwave signals, for the importance of such input signals, see [2]) and scattered electric field, the parameter estimation problems it to find a set of parameters such that the estimated electric field matches the measured data optimally under some criterion. Let the collection of unknown parameters be denoted by a vector $q = (\sigma, a_0, \dots, a_n)$. For given observations $\{\tilde{E}_{i,j}\}$ corresponding to measurements at times t_i and position z_j , we consider the least squares estimation problem of minimizing over $q \in Q$ the least squares functional

$$J(\tilde{E}, E; q) = \left| \{E(t_i, z_j; q)\} - \{\tilde{E}_{i,j}\} \right|^2, \tag{8}$$

where $\{\tilde{E}(t_i, z_j; q)\}$ are the parameter dependent weak solutions of (5)–(7) evaluated at each time $t_i, i = 1, 2, \dots, N_t$ and each position $z_j, j = 1, \dots, N_z$, and $|\cdot|$ is an appropriately chosen Euclidian norm. The set Q is some admissible parameter set.

The minimization in our parameter estimation problems involves an infinite dimensional state space and an infinite dimensional admissible parameter set (e.g., of functions $\sigma(z)$). We thus consider Galerkin type approximations in the context of the variational formulation of (5)–(7). Solving the approximate estimation problems, we obtain a sequence of estimates $\{\bar{q}^{N,M}\}$. Parameter estimate convergence and continuous dependence (with respect to the observations $\{\tilde{E}_{i,j}\}$) results can be obtained

under certain assumptions.

The convergence results allowing approximation of the parameter set provides a sound necessary basis for the reconstruction of conductivity and coefficients in polarization equation (6).

It is well known that evaluation of electric and magnetic fields in the microwave range is computationally expensive. To minimize the number of function evaluations, a Trust Region algorithm [8] is employed in solving the minimization problem. Moreover, the algorithm has potential to provide a global minimal.

Our research in electromagnetic inverse problems is at its preliminary stage. Our goal is to demonstrate the ability to reconstruct the physically related parameters in the time domain with the expectation of (a) incorporating the temperature dependence of the structure into our model, (b) using various type of incident signals such as short pulses and broad band continuous signal, and (c) utilizing the transient responses to improve the quality of identification.

References

- [1] Richard A. Albanese, Richard L. Medina and John W. Penn, "Mathematics, medicine and microwave," *Inverse Problems*, vol. 10, 1994, pp. 995-1007.
- [2] Richard Albanese, John Penn and Richard Medina, "Short-rise-time microwave pulse propagation through dispersive biological media," *J. of Optical Society of America A*, vol. 6, 1989, pp. 1441-1446.
- [3] R. Assous, P. Degond, E. Heintze, P. A. Raviart and J. Segre, "On a finite-element method for solving the three-dimensional Maxwell equations," *J. of Computational Physics*, vol. 109, 1993, pp. 222-237.
- [4] H. T. Banks, S. Gates, G. I. Rosen and Y. Wang, "The identification of a distributed parameter model for a flexible structure," ICASE Report 86-71, NASA Langley Res. Center, Hampton, VA, September 1986; *SIAM Journal on Control & Optimization*, vol. 26, 1988, pp. 743-762.
- [5] H. T. Banks and K. Ito, "A unified framework for approximation and inverse problems for distributed parameter systems," *Control Theory and Advanced Technology*, vol. 4, 1988, pp. 73-90.
- [6] H. T. Banks and Yun Wang, "Damage detection and characterization in smart material structures," CRSC-TR93-17, N. C. State University, November 1993; in *Control and Estimation of Distributed Parameter Systems*, Birkhäuser ISNM, vol. 118, 1994, pp. 21-43.
- [7] H. T. Banks, Y. Wang, D. J. Inman and J. C. Slater, "Approximation and parameter identification for damped second order systems with unbounded input operators," CRSC-TR93-9, N. C. State University, May 1993; *Control: Theory and Advanced Technology*, to appear.
- [8] J.E. Dennis Jr. and Robert B. Schnabel, *Numerical Methods for Unconstrained Optimization*, Prentice Hall, 1983.

- [9] G. Duvaut and J. L. Lions, *Inequalities in Mechanics and Physics*, Springer-Verlag, Berlin Heidelberg, 1976.
- [10] E. H. Grant, R. J. Sheppard and G. P. South, *Dielectric Behavior of Biological Molecules in Solution*, Oxford University Press, London, 1978.
- [11] J. D. Jackson, *Classical Electrodynamics*, 2nd Ed., John Wiley & Sons, New York, 1975.
- [12] B. V. Kapitonov, "Stabilization and exact boundary controllability for Maxwell's equations," *SIAM J. Control and Optimization*, vol. 32, 1994, pp. 408-420.
- [13] Katherine A. Kime, "Boundary controllability of Maxwell's equations in a spherical region," *SIAM J. of Control and Optimization*, vol. 28, 1990, pp. 294-319.
- [14] J. Lagnese, "Exact boundary controllability of Maxwell's equations in a general region," *SIAM J. of Control and Optimization*, vol. 27, 1989, pp. 374-388.
- [15] D. L. Russell, "The Dirichlet-Neumann boundary control problem associated with Maxwell's equations in a cylindrical region," *SIAM J. of Control and Optimization*, vol. 24, 1986, pp. 199-229.
- [16] Julius Adams Stratton, *Electromagnetic Theory*, McGraw-Hill, New York, 1941.

ULTRA-WIDEBAND TECHNIQUES FOR CLASSIFICATION AND IMAGING OF BURIED TARGETS

Lawrence Carin
Department of Electrical Engineering
Polytechnic University, Brooklyn

Leopold B. Felsen
Department of Aerospace and Mechanical Engineering
Boston University, Boston

Abstract

Object recognition can be parametrized systematically through physically robust wave objects by linking features (observables) in scattered field data with features on the object (target) giving rise to the data. The wave objects are broadly separated into global (mode) and local (wavefront) categories. Their parametrization requires different wave-oriented signal-processing algorithms which are implemented conveniently in relevant subdomains of the configuration (space-time) - spectrum (wavenumber-frequency) phase space [1]. We have found that confidence in any phase-space processing scheme is gained through "proper" physical understanding of scattering phenomenologies, and that the signal-processing algorithms can be fully calibrated by applying them to fully controlled and quantified canonical prototypes [2]. We have illustrated these processing strategies on several examples [1,3,4]. Because of space limitations, we discuss here only the numerical techniques that have been employed to generate the data base. The examples include short-pulse scattering from a perfectly conducting wire [3] or body of revolution (BOR) [4] buried in a lossy, dispersive halfspace (see Sec. I). The forward modeling is performed via the Method of Moments (MoM) and allows for the study of short-pulse scattering from fairly realistic (though specially oriented) three-dimensional targets, for example, a perfectly conducting buried mine. In Sec. II we consider scattering from a target in a halfspace with inhomogeneities in the soil profile and/or interface roughness; to account for such situations, we have developed an FDTD code (so far in two dimensions). Concerning the inverse problem, we have performed a systematic investigation of the resonant frequencies of buried targets. The late-time resonant frequencies of targets in unbounded space are aspect independent and therefore have been utilized for target identification. However, for targets buried near the soil interface, the resonant frequencies will in general be aspect dependent due to target-interface reverberations. This issue is investigated in detail in [3]. We have also performed space-wavenumber processing on buried-target scattering data, with the phase-space signature calculated using the windowed Fourier transform, wavelet transform, and windowed superresolution processing. All of the issues omitted here are dealt with in the oral presentation or in the cited references. Concerning analytical aspects, the wave-oriented modeling utilizes local-global decomposition (hybrid ray-mode and wavefront-resonance schemes), Gaussian steady-state and pulsed beams, deterministic-stochastic interactions [5], and others. The wave objects associated with these models can be forward and backward propagated for task-oriented reconstruction; these aspects are now under consideration.

I. Short-Pulse Scattering from Buried Bodies of Revolution: MoM Solution

Most previous investigations of ground penetrating radar (GPR) phenomenology have been based on narrowband operating conditions. Recently, however, there has been an interest in ultra-wideband short-pulse inputs for ground penetrating applications, because of the accompanying space-time resolution. Such systems generate short pulse waveforms with large instantaneous bandwidth, giving rise to time-domain phenomenology which is fundamentally different from that of narrowband systems. As a first step toward understanding the wave physics associated with short-pulse scattering from buried targets, we consider here short-pulse plane-wave scattering from buried perfectly conducting bodies of revolution (BOR). To make such a study tractable, the soil is modeled as a lossy, dispersive halfspace, and the axis of revolution of the buried target is assumed normal to the air-ground interface; this assumption restricts the target orientation but allows one to view the target-halfspace composite as a single BOR with consequent simplification in analysis and numerics. We solve the scattering problem in the frequency domain via MoM, using an algorithm analogous to those developed previously for scattering from BORs in freespace. After performing the MoM analysis over the bandwidth of the incident pulse, the time-domain scattered fields are synthesized via Fourier transform.

Several authors have investigated the MoM analysis of plane-wave scattering from conducting, dielectric, and composite BORs in free space. These algorithms take advantage of the azimuthal periodicity inherent in the incident fields, induced currents, and the free-space Green's function. Scattering from a buried BOR is complicated significantly by the fact that the half-space Green's function is a dyadic, each term of which is expressed in terms of highly oscillatory Sommerfeld integrals and their spatial derivatives. Thus, to make the MoM analysis of a buried BOR tractable, highly efficient techniques are required for the computation of the dyadic half-space Green's function, especially for the wideband applications here.

To compute the components of the half-space Green's function efficiently over wide bandwidths, we employ the method of complex images, developed by Chow *et al.* [3,4]. In this technique, the spectral Green's function inside the Sommerfeld integral is fit via Prony's method (or any other parametric algorithm, such as the matrix-pencil method) to a finite sum of complex exponentials, the integrals of which can be expressed in closed form via Sommerfeld's identity [3,4]. This formulation is highly efficient because the numerical burden is shifted from laboriously computing the Sommerfeld integrals via brute-force numerical integration to the relatively efficient task of performing a parametric fit to the spectral Green's function. For the BOR problem, after applying the method of complex images, each component of the dyadic Green's function is written as a sum of free-space Green's function (or its spatial derivatives) with complex source points. Thus, after applying the method of complex images, the techniques used for the MoM analysis of scattering from BORs situated in freespace – which take advantage of properties of the freespace Green's function – can be transferred directly to the problem of scattering from buried BORs.

For illustration, we consider short-pulse scattering from a perfectly conducting sphere and cylinder buried within a lossy, dispersive half space. The incident pulse is described by the waveform in Fig. 1, using a free-space center wavelength $\lambda_c = 1$ m ($f_c = 300$ MHz) consistent with

many ultra-wideband radar systems of interest. The frequency-dependent complex permittivity is taken from measured data for Puerto Rico clay with 10% water [3,4]. Although the algorithm is general, for these examples we assume that the pulsed plane-wave is incident normal to the air-ground interface. Further, results are presented for the scattered fields at the interface, since it is there that many GPR systems perform their measurements. We therefore do not employ a far-zone approximation; rather, we calculate the scattered fields using the complete dyadic Green's function applied in the MoM computations – again utilizing the complex image technique. For airborne GPR systems, one is usually interested in the far-zone fields, which can be calculated more easily by taking advantage of asymptotic simplifications to the Green's function.

The perfectly conducting sphere has a 30 cm diameter, and its center is situated 30 cm from the air-ground interface. The time-domain fields for this example are shown in Fig. 2. For the parameters considered, the first creeping wave response (also present in the freespace case) is clearly visible, arriving after the wavefront scattered by the initial interaction of the incident wave with the target. For this example, multiple reverberations between the surface of the sphere and the air-ground interface contribute negligibly to the total scattered field (we detect no scattered fields at times for which such multiple reverberations are expected). With the incident wave from the air described in Fig. 1, the incident waveform that hits the target is determined by the transmission coefficient at the interface as well as the propagation properties (dispersion and loss) between the interface and the target.

The next example considers short-pulse scattering from a perfectly conducting cylinder of radius 12.8 cm and thickness 8.5 cm buried inside the Puerto Rican soil used in Fig. 2; the distance from the top of the cylinder and the air-ground interface is 29.8 cm. The scattered fields for this example, observed along the axis of the cylinder, are shown in Fig. 3. Again, the scattered fields are characterized by a strong return from the top of the cylinder followed closely in time by a weaker return. However, now, this later response is attributed to a reverberation between the air-soil interface and the flat surface at the top of the target; this additional waveform after the specular return was not visible in the scattered signature from the same target in freespace (with the physical size of the cylinder modified such that it was the same size electrically with respect to the incident waveform). For the target orientation and excitation considered, there are no creeping waves.

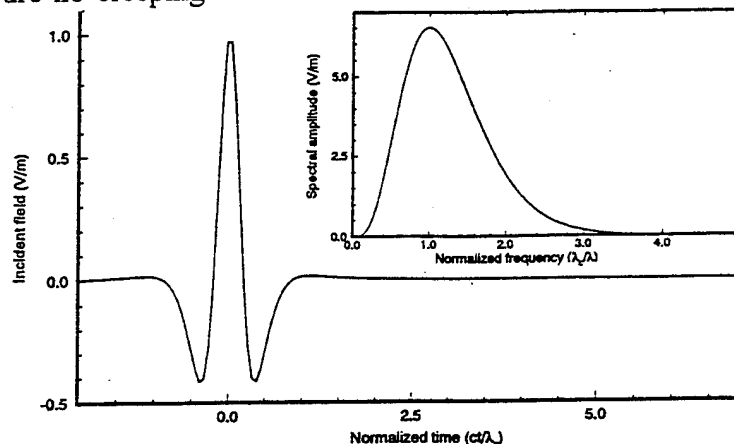


Figure 1. Incident pulse and its spectrum (inset) used for all numerical examples.

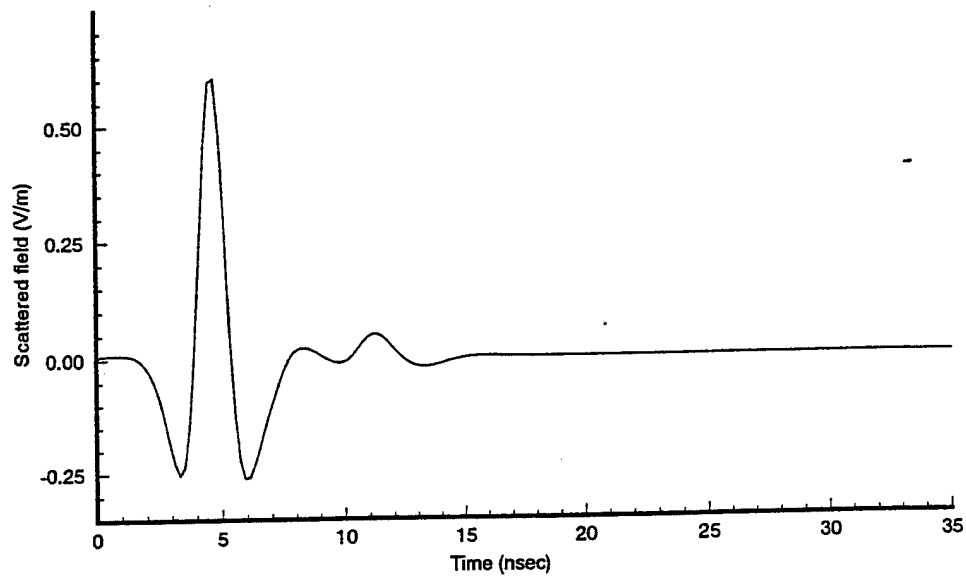


Figure 2. Time-domain fields scattered from a perfectly conducting sphere of radius 15 cm buried in a lossy, dispersive half space. The center of the sphere is 30 cm from the soil-air interface, the angle of incidence is $\theta_i=0^\circ$, the scattered fields are observed at the interface directly above the sphere center, and the polarization of the plotted scattered fields is the same as that of the incident wave. The arrow identifies the first creeping wave arrival.

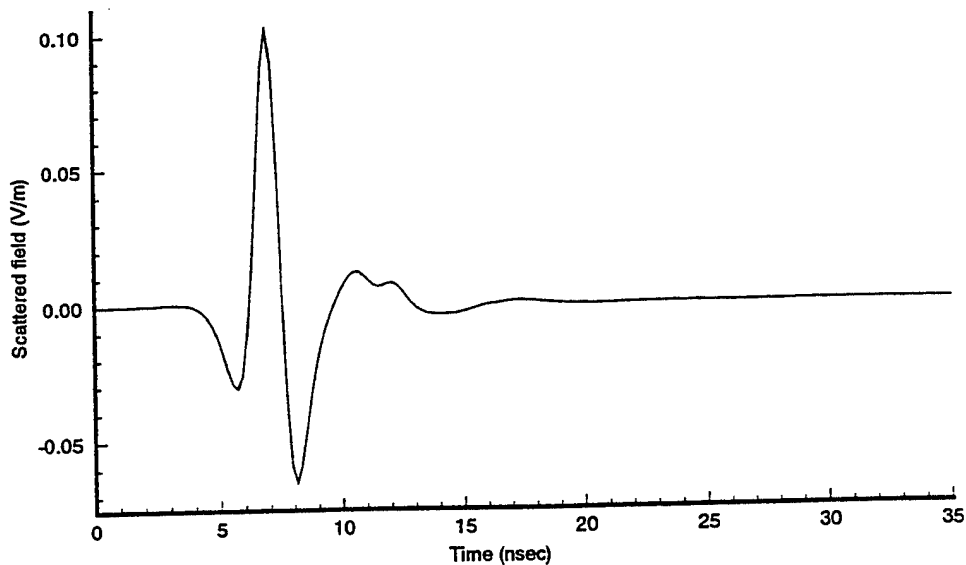


Figure 3. Time-domain fields scattered from a perfectly conducting cylinder of 12.8 cm radius and 8.5 cm thickness buried in a lossy, dispersive half space. The top of the cylinder is 29.8 cm from the air-soil interface; the angle of incidence is $\theta_i=0^\circ$; the scattered fields are observed at the air-soil interface, along the cylinder axis; the polarization of the plotted scattered fields is the same as that of the incident wave. The arrow identifies the first target-interface reverberation.

II. Short-Pulse Scattering from Buried Targets: FDTD Solution

For this class of problems, we have implemented a two-dimensional FDTD algorithm which utilizes a Huyghens surface for the incident field and a second-order Mur absorbing boundary condition (ABC). The GPR problem involves a difficulty which is not encountered for short-pulse scattering from targets in free space. Namely, to model plane-wave incidence, one must modify the FDTD algorithm to simulate an infinite soil region without introducing artifacts at the terminations of the model soil. This has been done by placing the model soil in direct contact with the ABC. However, one must now use a Huyghens surface for the incident field which simulates a pulsed plane wave interacting with an infinite half space. Thus, the Huyghens currents account for the wave which is transmitted into the soil as well as the reflected wave excited at the air-soil interface; if the geometry inside the Huyghens surface is a homogeneous half space, the fields outside the Huyghens surface vanish. However, discontinuities introduced into the half space (inhomogeneities in the soil profile, surface roughness, and targets) excite scattered fields, and these fields propagate outside the Huyghens surface and can therefore be separated from the incident waveform. It is in this manner that our FDTD GPR calculations have been performed and an example is shown here.

The problem geometry is shown in Fig. 4, with a pulsed plane wave incident at 45° (the shape of the incident pulse is as in Figs. 2 and 3). This geometry has been selected to simulate a rough soil surface and a buried perfectly conducting target located in a region of recently replaced excavated soil (rectangular enclosure); it has been shown in numerous GPR measurements that recently replaced excavated soil has an index of refraction different from that of undisturbed soil. The results in Figs. 5 (a)-(c) demonstrate the space-time evolution of the scattered fields. We can see that the surface roughness introduces interesting focusing effects inside the soil. Further, the scattered field from the target in Fig. 5(c) is seen to be affected by phenomena due to the contrast in dielectric constant. Such phenomenological studies yield insight into the GPR scattering and propagation mechanisms, and therefore are useful in guiding the development of wave-parametrized signal processing and imaging architectures.

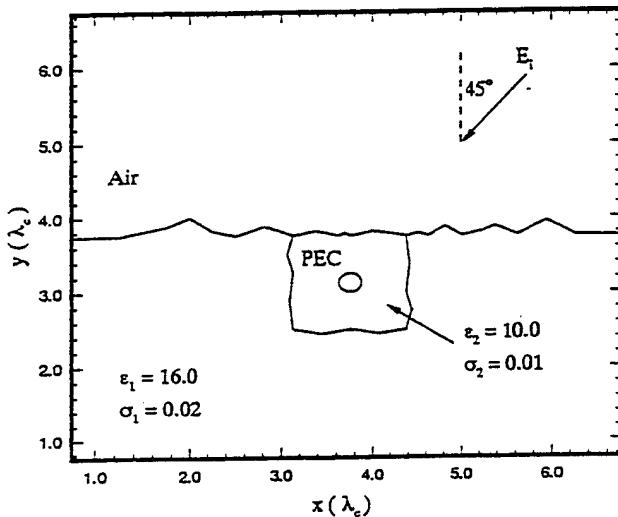


Figure 4. Geometry used in FDTD example.

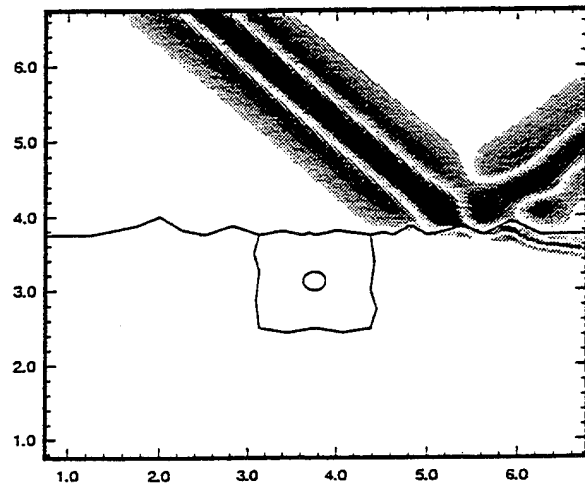


Figure 5(a)

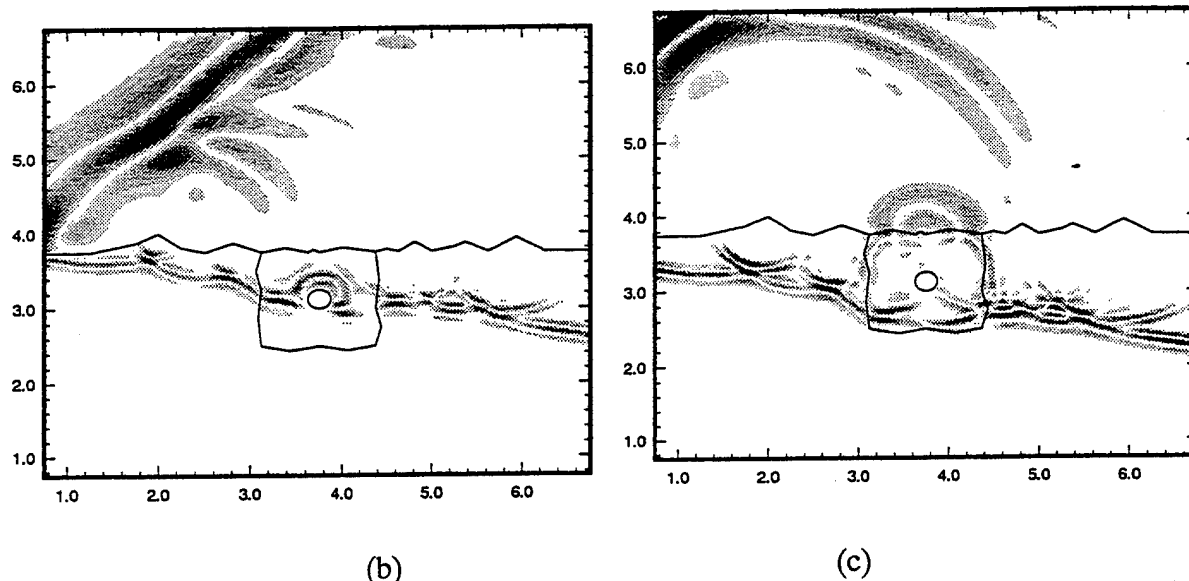


Figure 5. Space time evolution of fields scattered from rough-soil-surface and buried target. Time increases from (a) to (c), with each plot representing the spatial distribution of the fields at a snapshot in time.

Acknowledgement

This work was sponsored in part by the Army Research Office under Cooperative Agreement DAAH04-93-02-0010 and by the Air Force Office of Scientific Research under grant F49620-93-1-0093. The views and conclusions contained herein are those of the authors and should not be interpreted as necessarily representing the official policies or endorsements, either expressed or implied, of the Army Research Office, Air Force Office of Scientific Research, or the U.S. Government.

References

- [1] L. Carin and L.B. Felsen, "Wave-oriented data processing for frequency and time domain scattering by nonuniform truncated array," *IEEE Antennas and Propagation Magazine*, June. 1994.
- [2] L. Carin, L.B. Felsen, D.R. Kralj, H.S. Oh, W.C. Lee, and S.U. Pillai, "Wave-Oriented Data Processing of Dispersive Time-Domain Scattering Data," submitted to *IEEE Trans. Antennas Prop.*
- [3] S. Vitebskiy and L. Carin, "Short-pulse plane-wave scattering from and the resonances of a dipole buried inside a lossy, dispersive half space," submitted to *IEEE Trans. Antennas Prop.*
- [4] S. Vitebskiy, K. Sturgess and L. Carin, "Short-pulse plane wave scattering from a buried perfectly conducting body of revolution," submitted to *IEEE Trans. Antennas Prop.*
- [5] L.B. Felsen, "On local vs. global parametrization of short-pulse excited scattering and spectra: Poisson summation revisited," Dept. of Aerospace and Mechanical Engineering, Boston Univ., Boston, MA 02215. Technical Report No. AM-94-026.

Processing Experimental Ground Penetrating Radar Data.

R. Deming and A.J. Devaney

Center for Electromagnetic Research
Department of Electrical and Computer Engineering
Northeastern University, Boston, MA 02115

1 Introduction.

In this study, the maximum likelihood estimation procedure is used to locate buried pipes based on experimental ground penetrating radar (GPR) return data. The report begins with a review of the relevant estimation theory, then describes how the theory is applied to our particular application. Finally, results are reported from an experimental GPR survey.

2 Estimating parameters from noisy measurements - probability densities and log-likelihood functions.

This report is based on the general problem of estimating a set of parameters from noisy observations. Here, the parameters are the location coordinates of a buried object, while the observations are voltage samples of radar return pulses. Assume the following model for the measurement of data s in the presence of additive noise n :

$$s = d(x) + n. \quad (1)$$

Here, $\mathbf{x} = (x_1, x_2, x_3, \dots, x_n)$ is the vector of parameters to estimate given the measured data vector $\mathbf{s} = (s_1, s_2, s_3, \dots, s_m)$, while $\mathbf{d}(\mathbf{x}) = (d_1(\mathbf{x}), d_2(\mathbf{x}), \dots, d_m(\mathbf{x}))$ is the parameter-dependent data model, i.e. the data that would be expected in the absence of noise.

A natural way to estimate \mathbf{x} would be to construct the conditional probability density function $p(\hat{\mathbf{x}}/\mathbf{s})$, to evaluate it for the measured data \mathbf{s} , then to maximize the function over the domain of $\hat{\mathbf{x}}$. The function is relatively easy to compute assuming uncorrelated, Gaussian white noise. Then [1]

$$p(\hat{\mathbf{x}}/\mathbf{s}) = \frac{p(\mathbf{s}/\hat{\mathbf{x}})p(\hat{\mathbf{x}})}{p(\mathbf{s})}, \quad (2)$$

where, for independent data elements s_i ,

$$p(\mathbf{s}/\hat{\mathbf{x}}) = \prod_{i=1}^m \frac{1}{\sqrt{2\pi\sigma_i^2}} \exp \left[\frac{-1}{2\sigma_i^2} |(s_i - \mu_i) - d_i(\hat{\mathbf{x}})|^2 \right]. \quad (3)$$

Here, the noise component n_i has mean μ_i and variance σ_i^2 .

Often, however, the *a priori* probabilities $p(\hat{\mathbf{x}})$ and $p(\mathbf{s})$ will not be known. In "maximum likelihood estimation", these probabilities are set to unity, and \mathbf{x} is estimated simply by maximizing $p(\mathbf{s}/\hat{\mathbf{x}})$ as given in equation(3). Or, since the natural log function is monotonic, the estimate can be made by maximizing the log of equation(3), i.e.

$$L(\hat{\mathbf{x}}) = \sum_{i=1}^m \frac{-1}{2\sigma_i^2} |(s_i - \mu_i) - d_i(\hat{\mathbf{x}})|^2. \quad (4)$$

This function is known as the log-likelihood [1].

An alternate expression results from expanding the squared term and retaining only the terms which depend on $\hat{\mathbf{x}}$. Then

$$L(\hat{\mathbf{x}}) = \sum_{i=1}^m \frac{1}{\sigma_i^2} (2\Re[(s_i - \mu_i)^* d_i(\hat{\mathbf{x}})] - |d_i(\hat{\mathbf{x}})|^2), \quad (5)$$

where the $*$ indicates the complex conjugate of any non-real values.

The log-likelihood function $L(\hat{\mathbf{x}})$ can be computed over a range of parameters $\hat{\mathbf{x}}$, i.e. a "log-likelihood image" can be constructed, where the estimate $\hat{\mathbf{x}}$ will correspond to the location of the image peak. If the signal-to-noise ratio of the data is high enough, the peak of the log-likelihood image should roughly correspond to the actual object location.

Note that the first term in equation(5) is simply the correlation between the measured data and the data model (after subtracting μ_i and weighting by $\frac{1}{\sigma_i^2}$). The second term, which may be called the "energy term", is often slowly varying over the domain $\hat{\mathbf{x}}$ relative to the correlation, and therefore may not significantly affect the maximum likelihood peak within a local radius. Therefore, in certain cases the log-likelihood function is simply the weighted correlation between the measured data and the data model.

3 Estimation theory for GPR surveys.

The general notation of the preceding section is now adapted to the particular application of time domain GPR. Suppose that a GPR survey consists of a series of experiments, from which it is hoped to locate a buried target object with known characteristics (e.g. a six inch steel pipe). An "experiment" is defined as a collection of measurements made at a single receiver location simultaneous with the excitation of a single transmitter. The experiments can be either monostatic or bistatic. At each receiver, measured data consists of a time domain pulse, scattered by the target object, corrupted by noise, and then sampled. Thus, the following signal model results in the time domain:

$$s_{jk}(t_l) = d_{jk}(t_l; \mathbf{x}_0) + n_{jk}(t_l), \quad (6)$$

where

- $s_{jk}(t_l)$ is the noisy signal, sampled at time t_l , and measured at receiver k simultaneous to the excitation of transmitter j ;
- $d_{jk}(t_l; \mathbf{x}_0)$ is the data model for an object located at coordinates $\mathbf{x}_0 = (x_0, y_0, z_0)$;
- $n_{jk}(t_l)$ is additive Gaussian white noise with variance $\sigma_{jk}^2(t_l)$ and mean $\mu_{jk}^2(t_l)$.

As described above, the log-likelihood function has the following expression:

$$L(\hat{\mathbf{x}}) = \sum_{j=1}^J \sum_{k=1}^K \sum_{l=1}^L \frac{1}{\sigma_{jk}^2(t_l)} \left[2[s_{jk}(t_l) - \mu_{jk}(t_l)]d_{jk}(t_l; \hat{\mathbf{x}}) - d_{jk}^2(t_l; \hat{\mathbf{x}}) \right]. \quad (7)$$

It is evident that the total log-likelihood function can be computed by adding the individual log-likelihood functions from each of the JxK experiments.

4 A simple data model for time domain, monostatic experiments.

In the time domain, a simple data model can be derived which is valid for monostatic experiments, and is based on the following approximations:

- the soil and buried object are nondispersive (frequency independent);
- the target object is far enough from the antennas that radiation incident on the object looks locally like a plane wave, as does radiation scattered to the receiving antenna;
- the target object is small compared with all wavelengths of the radar, thus it can be treated as a point scatterer;
- the radiation pattern of the antennas is independent of the radar frequency.

Using the approximations, for a receiver located at the origin the data model can be expressed as

$$d(t; \mathbf{x}) = A^2(\hat{\mathbf{r}})p(t - 2r/c)F^2(r)D, \quad (8)$$

where

- r is the length of the vector \mathbf{x} , while $\hat{\mathbf{r}}$ is a unit vector with the direction of \mathbf{x} ;
- $2r/c$ is the round-trip propagation time for the pulse (c is the propagation velocity);
- $p(t)$ is the second derivative of the transmitted pulse [5];
- $F(r)$ is a radial gain function consisting of geometrical spreading, soil attenuation, and any other losses (e.g. energy loss from ground surface reflection);
- D is a quantity representing the scattering strength of the target;
- $A(\hat{\mathbf{r}})$ gives the directional dependence of the power radiated by the antennas.

Using equation(7), the time domain log-likelihood function for each experiment is then

$$L(\hat{\mathbf{x}}) = A^2(\hat{\mathbf{r}})F^2(r)D \sum_{l=1}^L \frac{2}{\sigma^2(t_l)} [s(t_l) - \mu(t_l)]p(t_l - 2r/c), \quad (9)$$

where the energy term has been ignored. Notice that the directional $\hat{\mathbf{r}}$ dependence of this expression is a multiplicative factor. Thus the log-likelihood function for a single experiment can be quickly computed by first evaluating L along a radius in a single direction, then sweeping this one dimensional vector over all directions $\hat{\mathbf{r}}$, and finally multiplying by the directionally dependent function $A(\hat{\mathbf{r}})$. The total log-likelihood function is then obtained by adding the subimages from all monostatic experiments.

4.1 Estimating the noise variance and radial gain function from measured data.

In preceding section a method was outlined for computing log-likelihood functions in time domain GPR. However, the method depends on knowing both the noise statistics, $\sigma^2(t_k)$ and $\mu(t_k)$, and the soil-dependent gain function $F(r)$. Due to the variable nature of soil (electrical properties and clutter content), these functions cannot be accurately predicted in practice. However, we can estimate them from our data.

Based on observations of actual GPR return signals, it is evident that noise results mainly from ground clutter. For a particular experiment in a GPR survey, the return data will be mostly noise if the target object is in the periphery of the antenna. This will be the case with most experiments in a typical survey, therefore the noise mean and variance can be estimated simply by averaging across all experiments in a survey.

It is also possible to approximate the radial gain function $F(r)$ by using the estimated noise variance. Consider the subsurface of the earth as a distribution of tiny clutter volumes, where scattering from each volume contributes to the total noise. Assume that the scattering potential of each volume is a zero-mean random process, which is reasonable if air pockets as well as rocks may be embedded in the soil. The variance of the noise component from each tiny volume is governed by a relation similar to that of the target signal in equation(8), i.e.,

$$\sigma_{\Delta n}^2(t; \mathbf{X}) = [A^2(\hat{\mathbf{r}})F^2(ct/2)]^2 \sigma_c^2, \quad (10)$$

where the transmitted signal is assumed to be a very short pulse $p(t) = \delta(t)$. Here, σ_c^2 is the variance of the scattering potential for each tiny volume of clutter.

For a short pulse, at each time t , the total noise received originates from clutter contained in a cylindrical shell with radius $r = ct/2$, i.e. with volume proportional to $r = (ct/2)$ (we are treating the problem as 2D). Therefore, the total noise variance at time t is described by the relation

$$\sigma_n^2(t) \propto (ct/2)[F^2(ct/2)]^2. \quad (11)$$

The radial dependence of the gain function is therefore given by the relation

$$F^2(r) \propto \frac{\sigma_n(2r/c)}{\sqrt{r}}. \quad (12)$$

It should be noted that, in practice, this function will diverge as r goes to zero. Since it was derived using some farfield approximations, it should therefore not be used for small radial distances. Work is being done on near-field modeling.

5 Experimental results.

A multimonostatic GPR survey was conducted using a "Georadar" step frequency radar with a frequency range of 450 steps from 100MHz to 1GHz (2MHz increments). The test site consisted of fairly wet soil in which metal pipes were buried at depths of less than two meters. The survey was performed by moving the radar set continuously in straight lines perpendicular to the axis of the pipes (the direction of motion corresponds to the x axis on all image plots). Each experiment (record) in the survey corresponds to data measured at a certain x coordinate. Radar return data thus consists of 450 complex amplitudes (magnitude and phase at each frequency) per experiment. In order to process in the time domain, the complex amplitude information (frequency domain) was preprocessed by Fourier transforming.

Results from the various stages of processing are shown in Fig.1 for a particular sub-survey. There are known to be two pipes in the corresponding section of ground, at coordinates $(x, z) = (2.8, -0.6)$ (4" diameter) and $(1.8, -1.0)$ (6" diameter). The pipes are evident in all images of Fig. 1. The survey consists of 90 experiments (x positions), with 70 time domain return samples per experiment.

In 1a., the return pulses are simply stacked without range gaining. A surface reflection is evident at shallow depths across all experiments, while the pipe at (2.8, -0.6) appears as a typical hyperbolic arc. It is difficult to observe the second pipe. In 1b., the returns have been weighted by the noise standard deviation, averaged across all experiments for each time sample. This procedure is consistent with the discussion in the preceding sections. Now it is much easier to observe the second pipe, which appears faintly hyperbolic, and seems to be resonating. In 1c., the log-likelihood function has been computed as described by equations(9) and (12), where the transmitted pulse has been approximated as a delta function. The directional dependence of the antennas has been modeled as $\cos^2(\theta)$, which seems consistent with the data. The effect of this processing seems to be a focussing of the hyperbolic arcs. Notice that the surface reflections appear greatly diminished. Finally, in 1d. the log-likelihood function has been thresholded at a level which is 80 percent of the maximum absolute value. This result demonstrates the potential value of the algorithm for an automatic data processing scheme. Both pipes appear in the image, with few false readings. Recall that the processing has required no operator adjustments or interventions.

References

- [1] A. Whalen, Detection of Signals in Noise, Academic Press, 1971.
- [2] A.J. Devaney and A. Schatzberg, "Maximum Likelihood Estimation of Target Location in Electromagnetic and Acoustic Imaging".
- [3] H.L. Van Trees, Detection, Estimation and Modulation Theory, Part I, Wiley, New York, 1968.
- [4] A.J. Devaney Associates Inc., "Detection and Parameter Estimation from Electromagnetic Scattering Data in an Offset VSP Geometry" (Final Report prepared for the U.S. Dept. of Energy), June 21, 1994.
- [5] A.J. Devaney Associates Inc., "Wavelet Processing of Tomographic Data for Medical and Nonmedical Applications" (Final Report prepared for ARPA), Feb.18, 1995.

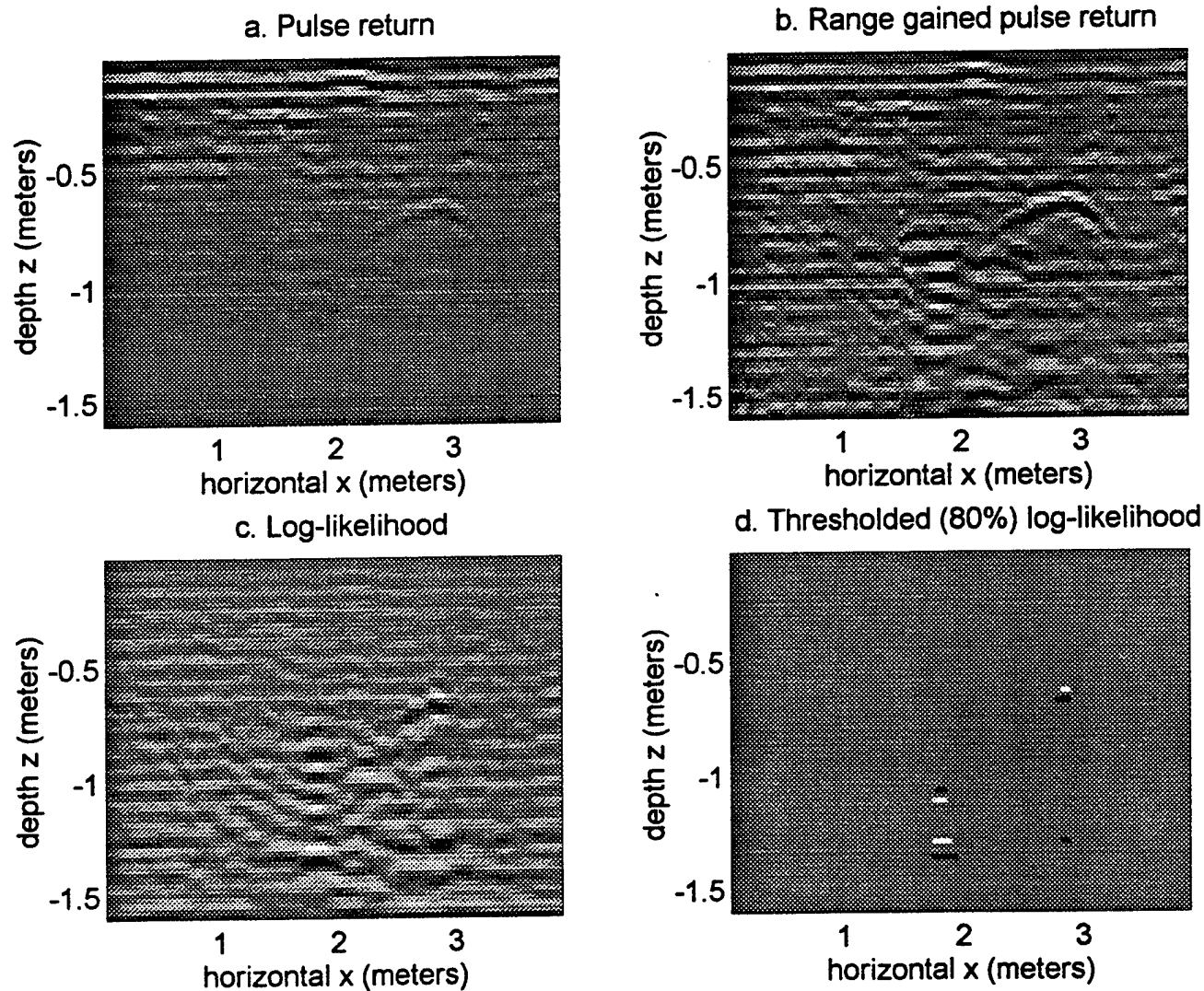


Figure 1.

FREQUENCY DEPENDENT ELECTROKINETIC STUDIES OF ROCKS AND SOILS

David Lesmes, Laurence Jouniaux and Dale Morgan (P. I.)
Earth Resources Laboratory, Dept. of Earth, Atmospheric, and Planetary Sciences.
Massachusetts Institute of Technology, Cambridge.

Abstract

The frequency dependent electrokinetic properties of rocks and soils are currently unknown, even though they are vital to our understanding of the electric signals that are observed to be generated by seismic waves propagating in the earth. These electric fields are caused by relative fluid flow in rocks, induced by a passing seismic wave. This relative flow then induces a streaming current that results in an electric dipole, which is the source of a electromagnetic wave that oscillates with the same frequency as the seismic excitation.

Electroseismic signals have been measured in a variety of field environments, and corresponding theoretical studies are currently under way. The differences in the electroseismic prospecting (ESP) and the seismic sections can reflect the fact that the ESP signals are not only sensitive to the seismic structure, but are also sensitive to the electrokinetic properties of the formation (Thompson and Gist, 1991, 1993). Electroseismic prospecting is potentially a very powerful new exploration method that may provide information both about subsurface hydrogeological parameters (e.g., porosity and permeability) and about the subsurface chemical environment.

The coupling of hydraulic flow and electric currents within the earth is governed by Onsager's laws (1931) of irreversible thermodynamics, namely:

$$q = \frac{-k}{\eta} \nabla P - \sigma_r C_v \nabla V \quad (1)$$

and

$$j = -\sigma_r C_v \nabla P - \sigma_r \nabla V, \quad (2)$$

where q is Darcy's volume fluid velocity per unit cross-sectional area and j is the electrical current density. ∇P and ∇V are the hydraulic pressure gradient and the electrical potential gradient, receptively. The rock permeability is given by k and its electrical conductivity by σ_r . The viscosity of the pore liquid is η . C_v is the voltage cross-coupling coefficient and gives the voltage generated per unit pressure gradient. Fluid flow problems within the earth can be modeled by self-consistently solving equations (1) and (2) with the appropriate boundary conditions (Nourbehecht, 1963; Sill, 1983; Wurmstich *et al.*, 1991; Wurmstich and Morgan, 1992, 1994). The major weak point in solving equations (1) and (2), even for steady state flows, is the sparcity of C_v data.

To better understand and model the electroseismic phenomena, we must know the *frequency dependence* of the electrokinetic coupling coefficients for various rock and soil types. The limited data that exist in the chemistry literature for capillaries and

porous diaphragms indicate that the streaming potential is very sensitive to frequency and that it is a complex function of the capillary geometries and the solution chemistry.

Packard (1953) measured the streaming potential responses of soda glass capillaries of varying radii (1.67 mm and 1.46 mm) (figure 1a). Packard developed a theory for the frequency dependent streaming potential responses of capillaries. His theory predicts that for frequencies greater than a critical pulsation ω_0 the streaming potential response will decrease with increasing frequency (figure 1b). For frequencies less than ω_0 , the streaming potential response asymptotically approaches the (dc) Helmholtz-Smoluchowski value. The critical frequency is given by

$$\omega_0 = \frac{\eta}{\rho a^2}, \quad (3)$$

where η and ρ are the fluid viscosity and density, and a is the capillary radius. The critical frequencies for the G2 and G4 capillaries are 0.051 Hz and 0.067 Hz, respectively.

Cooke (1955) measured the streaming potential responses of porous diaphragms over the frequency range of 1 Hz to 400 Hz (figure 2). The samples were saturated with 0.01 N KCl solutions. The critical frequency is approximately 20 Hz, which is much larger than the critical frequencies for the capillaries.

Streaming potential measurements were made by Sears and Groves (1977) on capillaries coated with bovine serum albumin (BSA) (figure 3). Measurements on a capillary with a radius of $a = 0.508$ mm showed a critical frequency of 0.56 Hz. The streaming potential data begin to flatten off at a slightly higher frequency of approximately 1.0 Hz.

This frequency dependence should be even more pronounced in porous media, such as rocks, in which there are wide distributions of pore/grain sizes. Recently the governing equations for the coupled electromagnetics and acoustics of porous media has been derived (Pride, 1995) and the critical pulsation of the streaming potential in a porous medium has been shown to be

$$\omega_0 = \eta / (F k_0 \rho_f) \quad (4)$$

with F the formation factor measured at high frequency, k_0 the permeability measured at zero frequency and ρ_f the density of the fluid. This critical frequency is the same as the critical frequency in the dynamic permeability theory (Johnson et al., 1987). Knowing that we can expect higher critical frequencies as suggested by some dynamic permeability measurements on glass beads, sandgrains (Smeulders et al., 1992) or on fused glass beads and crushed glass (Charlaix et al., 1988). These authors measured critical frequencies of the order of 100 Hz for very high permeable synthetic samples, and we expect higher critical frequencies for rocks and soils.

Briefly, we propose a project with the following three parts: (1) to design and construct an experimental system to measure frequency-dependent electrokinetic properties of rocks and soils; (2) to measure the cross-coupling coefficients of rock and soil samples as a function of frequency from dc through the seismic frequency band (1 kHz), sample microgeometry, and solution chemistry; and (3) to develop a theory for the frequency dependence of the electrokinetic properties of rocks and soils. This research will be crucial in improving our understanding, modeling, and interpretation of the electroseismic phenomena and in determining its utility in applications, such as hydrological characterization, contaminant detection, and formation evaluation within a borehole environment.

Acknowledgment/Disclaimer

This work was sponsored (in part) by the Air Force Offices of Scientific Research, USAF, under grant/contract number F49620-95-1-0224. The views and conclusions contained herein are those of the authors and should not be interpreted as necessarily representing the official policies or endorsements, either expressed or implied, of the Air Force Office of Scientific Research or the U.S. Government.

References

1. Charlaix E, A.P. Kushnick and J.P. Stokes, Experimental study of dynamic permeability in porous media, *Physical Review Letters*, 61, 1595-1598, 1988.
2. Cooke, C.E., 1955, Study of electrokinetic effects using sinusoidal pressure and voltage, *J. Chem. Phys.*, 23, 2299.
3. Johnson D.L., J. Koplik and R. Dashen, theory of dynamic permeability and tortuosity in fluid-saturated porous media, *J. Fluid Mech.*, 176, 379-402, 1987.
4. Nourbehecht, B., 1963, Irreversible thermodynamic effects in inhomogeneous media and their applications in certain geoelectric problems, Ph.D. thesis, Massachusetts Institute of Technology.
5. Onsager, L., 1931, Reciprocal relations in irreversible processes I, *Phys. Rev.*, 37, 405-426.
6. Packard, R.G., 1953, Streaming potentials across glass capillaries for sinusoidal pressure, *J. Chem. Phys.*, 21, 303.
7. Pride S., Governing equations for the coupled electromagnetics and acoustics of porous media, *Physical Review B*, in press, 1995.
8. Sears, A.R. and J.N. Groves, 1977, The use of oscillating laminar flow streaming potential measurements to determine the zeta potential of a capillary surface, *J. Colloid Int. Sci.*, 65, 479.
9. Sill, W.R., 1983, Self-potential modeling from primary flows, *Geophysics*, 48, 73-86.
10. Smeulders D.M.J., R.L.G. Eggels and M.E.H. van Dongen, Dynamic permeability: Reformulation of theory and new experimental and numerical data, *J. Fluid Mechanics*, 245, 211-227, 1992.
11. Thompson, A.H. and G.A. Gist, 1991, Electrostatic prospecting, *Expanded Abstracts of the 61st Ann. Mtg. of SEG*, Houston, 425-427.
12. Thompson, A. and G.A. Gist, 1993, Geophysical application of electrokinetic conversion, *The Leading Edge*, Dec., 1169.
13. Wurmstich, B. and F.D. Morgan, 1992, Can electrical earthquake precursors be generated by electrokinetic processes?, presented at the International Workshop "Low frequency electrical precursors: Fact or Fiction?", Lake Arrowhead, CA.
14. Wurmstich, B. and F.D. Morgan, 1994, Modeling of streaming potentials due to oil well pumping, *Geophysics*, January.
15. Wurmstich, B., F.D. Morgan, R.L. Lytton, and G.-P. Merkler, 1991, Finite element modeling of streaming potentials due to seepage: Study of a dam, in *Expanded Abstracts, 61st Annual SEG meeting*, Houston, vol. 1, 542-544.

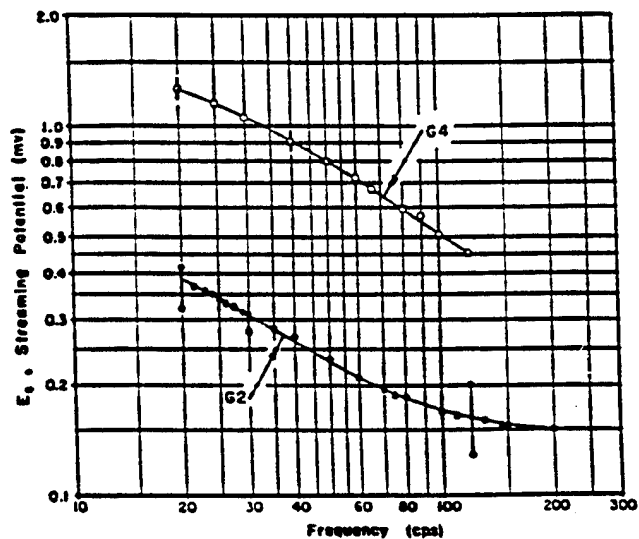


Figure 1a: Effective value of streaming potential versus frequency for a constant pressure amplitude of 10,000 Dynes/cm² (0.1 atm) (from Packard, 1953).

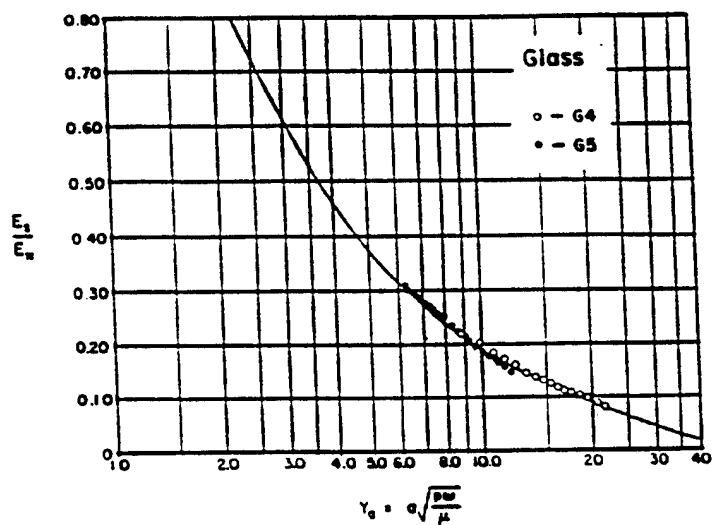


Figure 1b: Comparison of experimental values of streaming potential versus frequency with theory. Y_a is a reduced frequency variable, where ω is the angular frequency, a is the capillary radius, ρ is the fluid density, and μ is the fluid viscosity (from Packard, 1953).

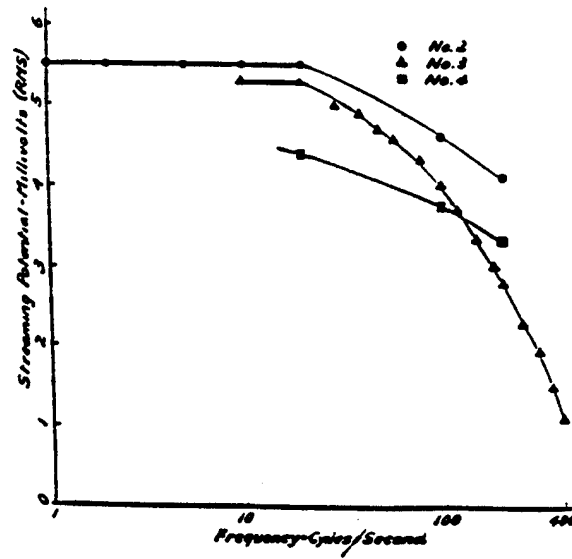


Figure 2: Plots of streaming potential versus frequency for three porous diaphragms (from Cooke, 1955)

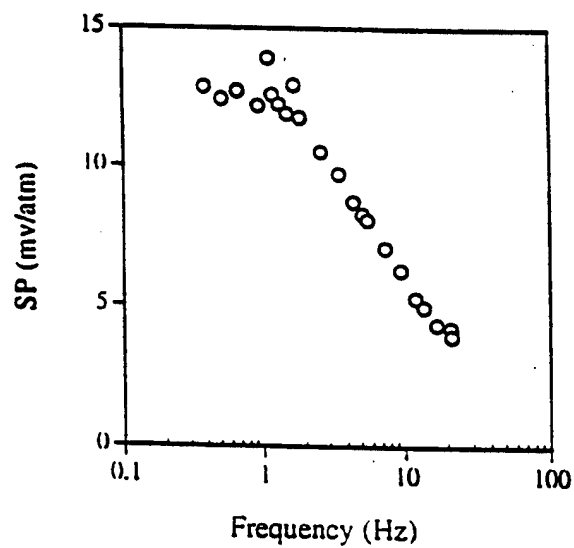


Figure 3: Streaming potential (cross-coupling coefficient) versus frequency for a BSA-coated capillary (from Sears and Groves, 1977).

NONLINEAR FILTERING APPLIED TO SINGLE-VIEW BACKPROPAGATED IMAGES OF STRONG SCATTERERS

J. B. Morris
Rome Laboratory
Hanscom AFB, MA

M. A. Fiddy
Department of Electrical Engineering
University of Massachusetts at Lowell

Abstract

In this abstract, we are concerned with characterizing the internal structure of 2D strongly scattering objects, using a single illumination direction or view and constant wavenumber $k_0 = 2\pi / \lambda_0$. The object is illuminated with the plane wave $e^{ik_0 \hat{\mathbf{r}}_i \cdot \mathbf{r}}$ and simulated scattered far-fields are calculated on a circular aperture in the plane of the object's cross section. A differential cepstral filter is applied to a single-view backpropagated image which relates to the product of the scattering potential and the total field. This nonlinear filter avoids the phase wrapping problems associated with homomorphic filtering, and is used to isolate the scattering potential from single-view backpropagated images.

The scalar Green's function solution to the scattered field from an inhomogeneous region can be written¹

$$\Psi^s(\mathbf{r}_s, \hat{\mathbf{r}}_i) = -k_0^2 \int_D V(\mathbf{r}') \Psi(\mathbf{r}', \hat{\mathbf{r}}_i) G(\mathbf{r}_s, \mathbf{r}') d\mathbf{r}' \quad (1)$$

where $V(\mathbf{r})$ is the scattering potential, $\Psi(\mathbf{r}, \hat{\mathbf{r}}_i)$ is the total (incident $\Psi^i(\mathbf{r}, \hat{\mathbf{r}}_i)$ plus scattered $\Psi^s(\mathbf{r}, \hat{\mathbf{r}}_i)$) field, $G(\mathbf{r}_s, \mathbf{r})$ is the free space Green's function, $\hat{\mathbf{r}}_i$ indicates the illumination direction, and the integral is over the object's compact support D . In two dimensions, $G(\mathbf{r}_s, \mathbf{r}) = \frac{i}{4} H_0^{(1)}(k_0 |\mathbf{r}_s - \mathbf{r}|)$ where $H_0^{(1)}(k_0 |\mathbf{r}_s - \mathbf{r}|)$ represents a zero order Hankel function of the first kind. When $|\mathbf{r}_s - \mathbf{r}| \gg D$ (far-field) one may use the following approximation

$$H_{0,f}^{(1)}(k_0 |\mathbf{r}_s - \mathbf{r}|) = \frac{4}{i} \sqrt{\frac{1}{8\pi k_0 r_s}} e^{i(k_0 r_s + \frac{\pi}{4})} e^{ik_0 \mathbf{r} \cdot \hat{\mathbf{r}}_s} \quad (2)$$

In this case, the scattered far-field in equation (1) may be written

$$\Psi_{ff}^s(\mathbf{r}_s, \hat{\mathbf{r}}_i) = -\sqrt{\frac{2k_0^3\pi^3}{r_s}} e^{i(k_0 r_s + \frac{\pi}{4})} F(\mathbf{r}_s, \hat{\mathbf{r}}_i) \quad (3)$$

where the scattering amplitude $F(\mathbf{r}_s, \hat{\mathbf{r}}_i)$ is defined as

$$F(\mathbf{r}_s, \hat{\mathbf{r}}_i) \equiv \frac{1}{4\pi^2} \int_D V(\mathbf{r}') \Psi(\mathbf{r}', \hat{\mathbf{r}}_i) e^{-ik_0 \hat{\mathbf{r}}_s \cdot \mathbf{r}'} d\mathbf{r}'. \quad (4)$$

It is common to adopt weakly scattering approximations to solve equation (4). For example, under the Born approximation (BA), one uses the incident field as an approximation to the total field reducing the scattering amplitude to the following²

$$F^{BA}(\mathbf{r}_s, \hat{\mathbf{r}}_i) = \frac{1}{4\pi^2} \int_D V(\mathbf{r}') e^{-ik_0(\hat{\mathbf{r}}_s - \hat{\mathbf{r}}_i) \cdot \mathbf{r}'} d\mathbf{r}'. \quad (5)$$

The Fourier transform of the scattering potential is defined as

$$\tilde{V}(\mathbf{k}) \equiv \frac{1}{4\pi^2} \int_{-\infty}^{\infty} V(\mathbf{r}') e^{-i\mathbf{k} \cdot \mathbf{r}'} d\mathbf{r}' \quad (6)$$

and we recognize that $F^{BA}(\mathbf{r}_s, \hat{\mathbf{r}}_i)$ specifies the Fourier transform of the scattering potential at $\mathbf{k} = k_0(\hat{\mathbf{r}}_s - \hat{\mathbf{r}}_i)$. An image of $V(\mathbf{r})$ may be reconstructed by either Fourier-based interpolation or by a backpropagation process³.

In practice, most objects are not weakly scattering and the Born approximation is not a valid one. For these more strongly scattering objects, the total field $\Psi(\mathbf{r}, \hat{\mathbf{r}}_i)$ in equation (4) is difficult to determine *a priori* due to internal multiple scattering effects. This makes the direct problem of calculating the scattered field a difficult one and greatly complicates the inverse problem. However, by multiplying the integrand in equation (4) by unity (i.e. $\Psi^i(\mathbf{r}, \hat{\mathbf{r}}_i) / \Psi^i(\mathbf{r}, \hat{\mathbf{r}}_i)$) one may formulate the scattering amplitude as⁴

$$F(\mathbf{r}_s, \hat{\mathbf{r}}_i) = \frac{1}{4\pi^2} \int_D V_{eff}(\mathbf{r}', \hat{\mathbf{r}}_i) e^{-ik_0(\hat{\mathbf{r}}_s - \hat{\mathbf{r}}_i) \cdot \mathbf{r}'} d\mathbf{r}' \quad (7)$$

where,

$$V_{eff}(\mathbf{r}, \hat{\mathbf{r}}_i) \equiv \frac{V(\mathbf{r}) \Psi(\mathbf{r}, \hat{\mathbf{r}}_i)}{\Psi^i(\mathbf{r}, \hat{\mathbf{r}}_i)}.$$

In equation (7), the scattering amplitude determines Fourier data on $V_{eff}(\mathbf{r}, \hat{\mathbf{r}}_i)$ for those frequencies $k_0(\hat{\mathbf{r}}_s - \hat{\mathbf{r}}_i)$. Under the Born approximation, $V_{eff}(\mathbf{r}, \hat{\mathbf{r}}_i)$ reduces to $V(\mathbf{r})$ and Fourier inversion of the scattering amplitude data collected over many illumination directions yields a low pass estimate of $V(\mathbf{r})$. For strongly scattering objects we

recognize that Fourier inversion of equation (7) is not strictly valid⁵ since $V_{eff}(\mathbf{r}, \hat{\mathbf{r}}_i)$ varies with $\hat{\mathbf{r}}_i$. However, by choosing $\hat{\mathbf{r}}_i$ to be constant, Fourier data limited to the circumference of an Ewald circle may be acquired.

The reconstructed image, using a single-view in the backpropagation algorithm⁶, may be written

$$S(\mathbf{r}', \hat{\mathbf{r}}_i = \text{constant}) = \frac{k_0^2}{2} \int_{-\pi}^{\pi} F(\mathbf{r}_s, \hat{\mathbf{r}}_i) e^{ik_0(\hat{\mathbf{r}}_s - \hat{\mathbf{r}}_i) \cdot \mathbf{r}'} \sqrt{1 - (\hat{\mathbf{r}}_s \cdot \hat{\mathbf{r}}_i)^2} d\phi_s \quad (8)$$

where

$$S(\mathbf{r}, \hat{\mathbf{r}}_i = \text{constant}) = \left[\frac{V(\mathbf{r}) \Psi(\mathbf{r}, \hat{\mathbf{r}}_i)}{\Psi'(\mathbf{r}, \hat{\mathbf{r}}_i)} \right] ** h(\mathbf{r}, \hat{\mathbf{r}}_i)$$

and ** denotes 2D convolution with the point spread function (PSF) $h(\mathbf{r}, \hat{\mathbf{r}}_i)$. In frequency space, the Fourier transform of $h(\mathbf{r}, \hat{\mathbf{r}}_i)$ can be considered a window function with a value $\sqrt{1 - (\hat{\mathbf{r}}_s \cdot \hat{\mathbf{r}}_i)^2}$ on the Ewald circle $k_0(\hat{\mathbf{r}}_s - \hat{\mathbf{r}}_i)$ and zero otherwise. We consider objects that have inhomogeneities large compare to the spatial resolution of $h(\mathbf{r}, \hat{\mathbf{r}}_i)$ so that the effects of the PSF can be neglected.

To isolate $V(\mathbf{r})$ in equation (8) from the perturbing factor $\Psi(\mathbf{r}, \hat{\mathbf{r}}_i) / \Psi'(\mathbf{r}, \hat{\mathbf{r}}_i)$, we utilize a filter in the spectrum of the derivative of the logarithm of $S(\mathbf{r}, \hat{\mathbf{r}}_i)$ (i.e. the differential cepstrum). Direct linear filtering is not appropriate for multiplied signals of this kind since their spectra are convolved. Phase wrapping problems are avoided in the differential cepstrum by omitting the logarithm explicitly in its definition. Neglecting $h(\mathbf{r}, \hat{\mathbf{r}}_i)$, the differential cepstrum⁷ of equation (8) becomes the spectrum of

$$\frac{\frac{\partial}{\partial x} S(\mathbf{r}, \hat{\mathbf{r}}_i)}{S(\mathbf{r}, \hat{\mathbf{r}}_i)} = \frac{\frac{\partial}{\partial x} V(\mathbf{r})}{V(\mathbf{r})} + \frac{\frac{\partial}{\partial x} \frac{\Psi(\mathbf{r}, \hat{\mathbf{r}}_i)}{\Psi'(\mathbf{r}, \hat{\mathbf{r}}_i)}}{\frac{\Psi(\mathbf{r}, \hat{\mathbf{r}}_i)}{\Psi'(\mathbf{r}, \hat{\mathbf{r}}_i)}} \quad (9)$$

After filtering, the reconstructed image of $V(\mathbf{r})$ is found by integration, and exponentiation. Successful recovery of $V(\mathbf{r})$ depends on how well the two terms on the right side of equation (9) separate in the differential cepstral domain.

Consider two lossless concentric cylinders with inner $\epsilon_r = 2$, radius 3.6cm and outer $\epsilon_r = 4$, radius 9.9cm, illuminated by a plane wave at 10GHz. Exact scattered far-field data were calculated and backpropagated (using equation (8)) to a 64x64cm² physical space. The magnitude of the single-view backpropagated image is shown in Figure 1. The scattering potential $V(\mathbf{r})$ is difficult to recognize since the total field $\Psi(\mathbf{r}, \hat{\mathbf{r}}_i)$ is very

different from the incident field $\Psi^i(\mathbf{r}, \hat{\mathbf{r}}_i)$ in this case (i.e. object represents a strong scatterer).

Using *a priori* knowledge of the object's size, the quantity $S(\mathbf{r}, \hat{\mathbf{r}}_i)$, of Figure 1, was set to zero just beyond its physical support D . A simple low pass filter was then applied to a regularized differential cepstrum. Figure 2 displays the reconstruction of the scattering potential generated from a filtered (in the differential cepstral domain) single-view backpropagated image for the same field-of-view as in Figure 1. Although uniqueness is not necessarily guaranteed⁸, the reconstruction qualitatively agrees with the original scattering potential $V(\mathbf{r})$.

In summary, single-view backpropagated images are formulated as the product of the scattering potential and the total field. A nonlinear processing technique is applied to remove the perturbing factor that tends to complicate images of more strongly scattering objects. Limitations of the proposed technique arise as the effects of the PSF become more prominent. In such cases, the backpropagated image of $V_{eff}(\mathbf{r}, \hat{\mathbf{r}}_i = \text{constant})$ is blurred to some extent due to the convolution with $h(\mathbf{r}, \hat{\mathbf{r}}_i = \text{constant})$. Currently, we are investigating a frequency extrapolation routine that exploits *a priori* knowledge of the object's support in an effort to improve the backpropagated images from strongly scattering structures.

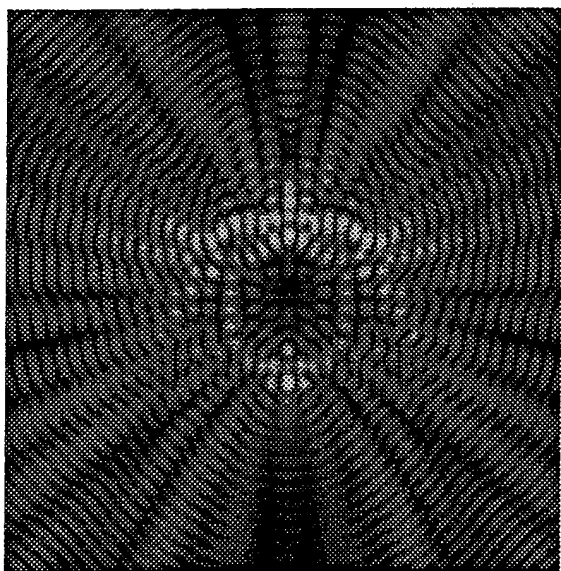


Figure 1.

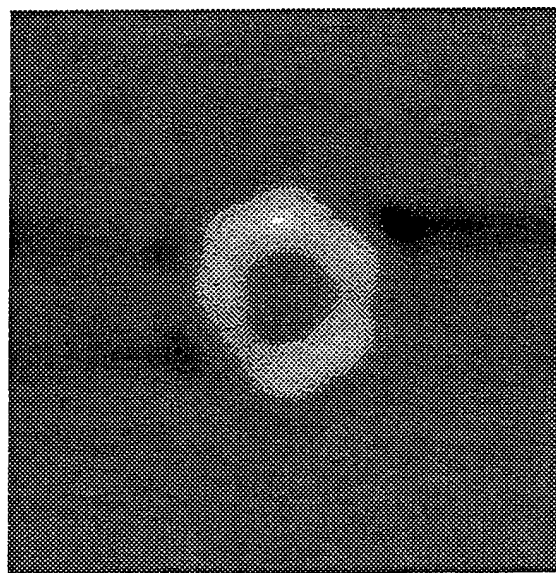


Figure 2.

Acknowledgment/Disclaimer

This work was sponsored in part by the Office of Naval Research grant N00014-89-J-1158. The views and conclusions contained herein are those of the authors and should not be interpreted as necessarily representing the official policies or endorsements, either expressed or implied, of the Office of Naval Research.

References

1. F.C. Lin, et al, Image estimation from scattered field data, 1990, International Journal of Imaging Systems Technology, Vol. 2, 76-95.
2. E. Wolf, Three-dimensional structure determination of semi-transparent objects from holographic data, 1969, Optics Communications, Vol. 1, No. 4, 153-156.
3. S.X. Pan, et al, A computational study of reconstruction algorithms for diffraction tomography: Interpolation versus filtered backpropagation, 1983, IEEE Transactions on Acoustics, Speech, and Signal Processing, ASSP-31, 1262, 1275.
4. M. Slaney, et al, Limitations of imaging with first-order diffraction tomography, 1984, IEEE Transactions on Microwave Theory and Techniques, Vol. MTT-32, 860-874.
5. B. Duchene, et al, Diffraction tomography approach to acoustical imaging and media characterization, 1985, Journal of the Optical Society of America A, Vol. 2, 1943-1953.
6. A.J. Devaney, A filtered backpropagation algorithm for diffraction tomography, 1982, Ultrasonic Imaging, 4, 336-350.
7. D. Raghuramireddy, et al, The two-dimensional differential cepstrum, 1985, IEEE Transactions on Acoustics, Speech, and Signal Processing, Vol. ASSP-33, 1335-1337.
8. A.J. Devaney, Nonuniqueness in the inverse scattering problem, 1978, Journal of Mathematical Physics, Vol. 19, 1526-1531.